Mass Spectrometry Techniques for Sublimated Gas

from Organic-Bearing Microparticles by Hypervelocity Impacts

Junichiro Nakazawa

Doctor of Philosophy

Department of Space and Astronautical Science

The Graduate University for Advanced Studies, SOKENDAI

March 2026

CONTENTS

Chapter 1: Introduction

1.1 Evolution of the Habitable Zone ……..…….... 7

1.2 Exploration of Ocean Worlds …….. 13

1.2.1 Bulk Density and Moment of Inertia

1.2.2 Planetary-Physics Techniques

1.3 Biosignature Investigations ……. 15

1.3.1 A Framework for Life-Detection

1.3.2 Biosignatures Based on Biomolecules

1.4 Flyby Sampling ……... 20

1.4.1 Trade-offs of Flyby Missions

1.4.2 In-situ Mass Spectrometry Using Hypervelocity Impacts

1.4.2.1 Cassini CDA (Cosmic Dust Analyzer)

1.4.2.2 Cassini INMS (Ion and Neutral Mass Spectrometer)

1.5 Positioning of This Study ……..……..……... 26

1.6 Structure of This Dissertation ……..…..…… 28

1.6.1 Overview

1.6.2 Detailed Outline by Chapter

1.6.2.1 Understanding Ionization and Sublimation Processes in Hypervelocity Impacts

1.6.2.2 Analysis of Neutral Gases Generated by Dust Impacts

Chapter 2: Modeling and Verification of Hypervelocity Impact Ionization Using the P4P Code

2.1 Overview of Hypervelocity Impact Ionization and Numerical Modeling Approaches …….. 32
2.2 P4P Code ……..…….. 34
2.2.1. Data from the Previous Studies
2.2.2. Hydrocode Simulations
2.2.3. Analytical Method for Calculating Ionization Degree
2.3 Comparison with Experimental Data …… 46
2.3.1. Non-Equilibrium Processes in Impact Ionization
2.3.2. Ion Yields
2.3.3. Ion Temperature
2.4 Summary ……..…….. 64

Chapter 3: Analysis of the Equivalence Between Laser Irradiation and Hypervelocity Impacts

3.1 Background and Motivation for Comparing Laser Ablation and Hypervelocity Impact 66
3.1.1 Experimental Limitations in Directly Reproducing Hypervelocity Impacts
3.1.2 Analogy of High-Temperature and High-Pressure Conditions Induced by Laser Irradiation
3.2 Numerical Methods and Simulation Conditions 70
3.2.1 Overview of the LILBID Experiment
3.2.2 Conditions in P4P Simulations
3.3 Simulation Results 78
3.3.1 Plasma Generation Process under Hypervelocity Impact
3.3.2 Temporal Waveforms and Ion Temperature Distribution under Hypervelocity Impact
3.3.3 Plasma Formation Process under Laser Irradiation Conditions
3.3.4 Temporal Profile and Ion Temperature Distribution under Laser Irradiation

3.4 Discussion 89
3.5 Future work 90
3.5.1 Extended Simulation
3.5.2 Detailed Electric Field Modeling for CDA simulation
3.5.3 Detailed Thin-Layer Laser Irradiation Modeling for LILBID Simulation
3.6 Summary 92

Chapter 4: Laser-Irradiation-Based Simulated Impact Experiments and Electron-impact Mass Spectrometry Observations

4.1 Experimental Validation of Laser–Impact Ionization Analogy Using Organic Particle Analogs ……..…..…. 94
4.2 Experimental Methods ……..……. 97
4.2.1 Overview of the Previous Studies: Hypervelocity Impact Mass Spectrometry of Polystyrene
4.2.2 Experimental System Configuration
4.2.3 Laser intensity
4.2.4 Experimental Apparatus and Methods
4.3 Results …….. 109
4.4 Discussion …… 113
4.5 Future work …….. 115
4.6 Summary …….. 116

Chapter 5: Development and Fundamental Characterization of Photoionization Method

5.1 Advancing from Electron to Photoionization: A Softer Approach to Impact Gas Analysis ……..… 118
5.2 Experimental Methods ……..……. 120
5.2.1 Construction of the Photoionization Experimental Apparatus
5.2.2 Modification of the Quadrupole Mass Spectrometer for Photoionization Compatibility
5.2.3 Gas Sample Introduction System
5.2.4 Sample Selection
5.3 Results ……. 125
5.4 Discussion ……...…… 129
5.5 Future work ……. 137
5.5.1 Overview
5.5.2 Modeling of the Photoionization Process
5.6 Summary ……. 139

Chapter 6: Conclusions and Future Perspectives

6.1 Conclusions ……..……... 140
6.1.1 Summary of the Present Study
6.1.2 Conclusions
6.2 Future Work …….……..…..……..…… 146
6.2.1 The Advancement of Impact-Generated Gas EI-MS
6.2.2 The Advancement of Impact-Generated Gas PI-MS
6.3 Prospects for Future Spaceborne Implementation …….. 152

Acknowledgements

References

Chapter 1. Introduction

1.1 Evolution of the Habitable Zone

Does life exist beyond Earth? This question has passed through countless minds and inspired a wide range of imaginations — from princesses dwelling on the lunar surface and octopus-like Martians to DNA-based organisms transferred to Earth by meteorites. Such fictions proliferated partly because humanity is capable to envision with or without facts. Contemporary science, however, has finally reached a stage where that blank canvas is beginning to take shape.

Since the first successful launch of an artificial satellite in 1957, numerous space exploration missions, primarily by the United States and the former USSR and then Russia, have been carried out (e.g., Cracknell & Varotsos, 2007). Space exploration quickly went beyond the Earth's orbit and rendered the Moon, Venus, and Mars no longer wholly unvisited, and revealed aspects of these worlds that telescopes alone could never show (e.g., Tsunakawa et al., 2015). As those missions sharpened our picture of the Moon and Mars steadily narrowing the room for unfettered speculation, the uniqueness of Earth as a planet swathed in oceans and nurturing life came into sharper relief by comparison.

In this context, the characteristics that make Earth habitable were systematized, and the idea of a habitable zone, "the range around a star within which liquid water can exist on a planet's surface under sufficient atmospheric pressure", gained currency. Although the concept itself appeared after 1950 (e.g., Huang, 1960), the current standard definition of the planetary system habitable zone, determined by stellar luminosity and a planet's orbital distance, was advanced in 1993 (Kasting et al., 1993). This immediately focused attention on Mars, a planet within the Sun's habitable zone, as a candidate for a habitable planet for extraterrestrial life (e.g., Maimone et al.,

2007). Following the first detections of exoplanets in the 1990s, planets orbiting within the habitable zones of other stars also drew intense interest (e.g., Overbye, 2013).

Meanwhile, missions to the giant gas planets in the outer region of the Solar System, which are well outside the classical habitable zone, opened new horizons. Of particular significance was Cassini–Huygens, a joint NASA/ESA mission launched in 1997 and inserted into Saturnian orbit in 2004 (Matson et al., 2003). The Cassini orbiter targeted Saturn, a world yet unexplored in detail (Wolf & Smith, 1995), while the Huygens probe conducted the first in-situ studies of the satellite Titan, the only known body in the Solar System besides Earth with a dense, nitrogen-dominated atmosphere at present(Lebreton et al., 2005). In 2005, Cassini observed plumes containing water vapor erupting from the south pole of Saturn's icy satellite Enceladus (Figure 1-1), suggesting for the first time the presence of a subsurface ocean beneath its ice shell (Porco et al., 2006).

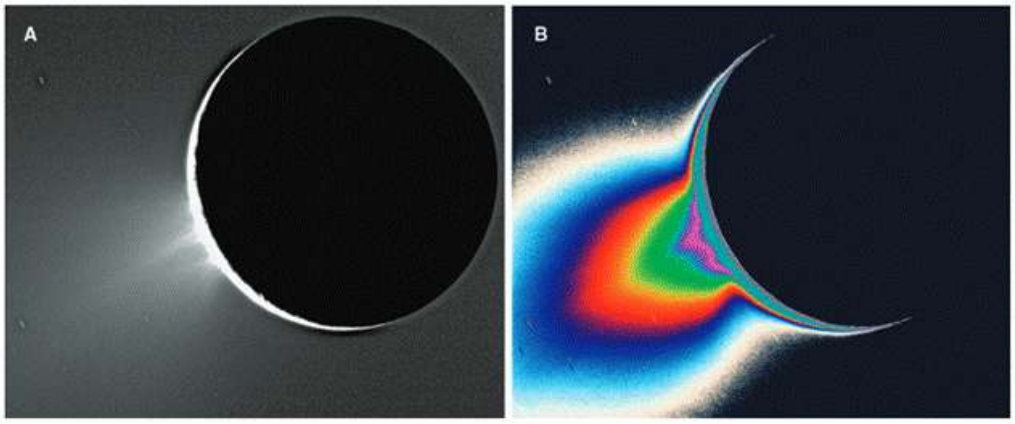

Figure 1-1. Plumes observed erupting from the south pole of Enceladus (Porco et al., 2006). Left: image captured by Cassini's Imaging Science Subsystem (ISS) Narrow Angle Camera (NAC). Right: a contrast-enhanced rendering in false color of the same scene.

Subsequent repeated flybys and gravity-field investigations indicated that the interior ocean may be global and extensive (Iess et al., 2014). In addition, Cassini's Cosmic Dust Analyzer (CDA) (Srama et al., 2004) performed mass spectrometry of solid grains within the plumes, suggesting that Enceladus's ocean is connected to a rocky core and may host hydrothermal reactions similar to those on Earth (Hsu et al., 2015). Results from the Ion and Neutral Mass Spectrometer (INMS) (Waite Jr et al., 2004) further implied that serpentinization, a reaction considered a key step in the origin of life on Earth, could be occurring at hydrothermal sites within Enceladus as shown in Figure 1-2 (Sekine et al., 2015; Waite et al., 2017). Collectively, these discoveries elevated Enceladus to one of the most promising bodies to search for extraterrestrial life in the Solar System and thrust it onto center stage in debates over the origin of life (e.g. Burchell and Wozniakiewicz, 2024).

Although there has been active, long-standing discussion among geochemists and biologists about the environments and chemistries that could have fostered life on early Earth (e.g., hydrothermal vents), Earth's present environment has been substantially modified by life itself, leaving scant direct information from the time of the emergence of life. Consequently, simulations and laboratory analogs alone are insufficient to resolve hypotheses about the origin of life. In this light, physical and chemical information from Enceladus's subsurface ocean, which is an analog to early Earth environments, has become an exceptionally valuable target for origin-of-life studies.

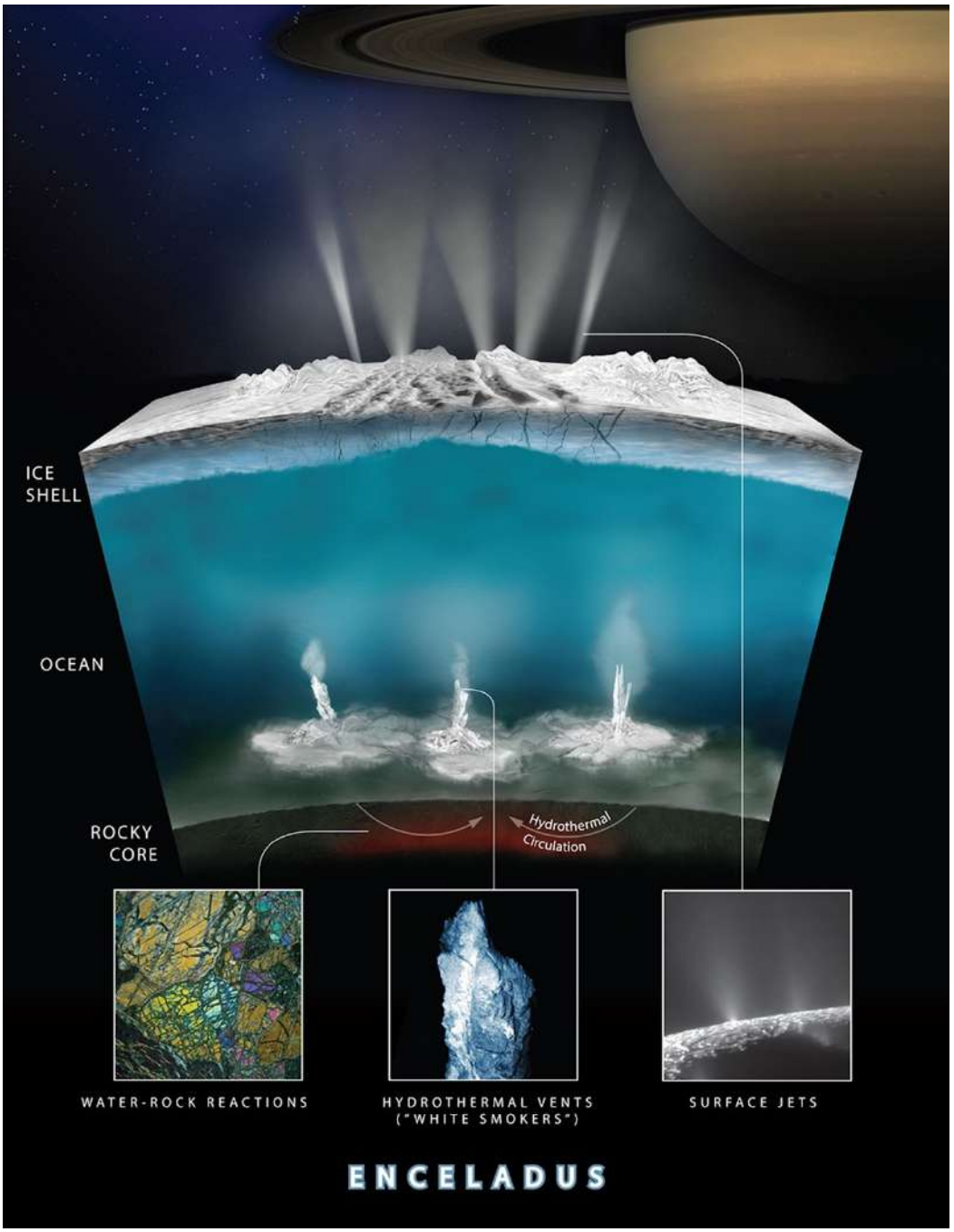

Figure 1-2. Schematic illustration of the internal structure of Saturn's icy moon Enceladus, showing an ice shell overlying a global subsurface ocean and a rocky core. Water–rock interactions at the seafloor drive hydrothermal circulation, producing hydrogen-rich fluids that rise through the ocean and are expelled as plumes through fractures in the ice shell. These plumes provide direct access to ocean-derived material and represent prime targets for in situ compositional analysis during spacecraft flybys. Adapted from "Enceladus Hydrothermal Activity," by National Aeronautics and Space Administration (2017).

These findings profoundly challenged the prevailing notion of the habitable zone as the circumstellar range where liquid water can exist on a planetary surface under sufficient atmospheric pressure (Kasting et al., 1993). The concept has since broadened: the traditional surface habitat, where liquid water resides on a planetary surface, has been complemented by a deep habitat, referring to interior oceans within icy bodies such as Enceladus (Figure 1-3). Recent deep space missions show that Enceladus is not unique in potentially harboring such interior oceans. NASA's Galileo mission (1995–2003) revealed that the Jovian satellites Europa, Ganymede, and Callisto might also host subsurface oceans (Spohn & Schubert, 2003). NASA's New Horizons mission, operating since 2015, suggested a possible interior ocean within Pluto (Nimmo et al., 2016). Analyses of Voyager 2 data even implied that satellites of Uranus and Neptune might possess interior oceans (e.g., Peterson et al., 2015). The exploration of deep habitats has thus advanced rapidly, and the term ocean worlds, bodies with oceans either at the surface or within, has entered common scientific parlance.

Exploration of ocean worlds is also gaining momentum internationally. JUICE, an ESA mission with JAXA participation, was launched in 2023 to target Ganymede (Grasset et al., 2013), while NASA's Europa Clipper was launched in 2024 to investigate Europa (Phillips & Pappalardo, 2014). Moreover, the Planetary Decadal Survey 2023–2032 (National Academies of Sciences, 2022) recommended a Uranus Orbiter and Probe as the top flagship priority to study Uranus and its potentially ocean-bearing satellites, and the Enceladus Orbilander (MacKenzie et al., 2021), a combined orbiter-lander mission to Enceladus, as the second priority. These priorities underscore the prominence of ocean worlds exploration and life detection in Europe and the United States.

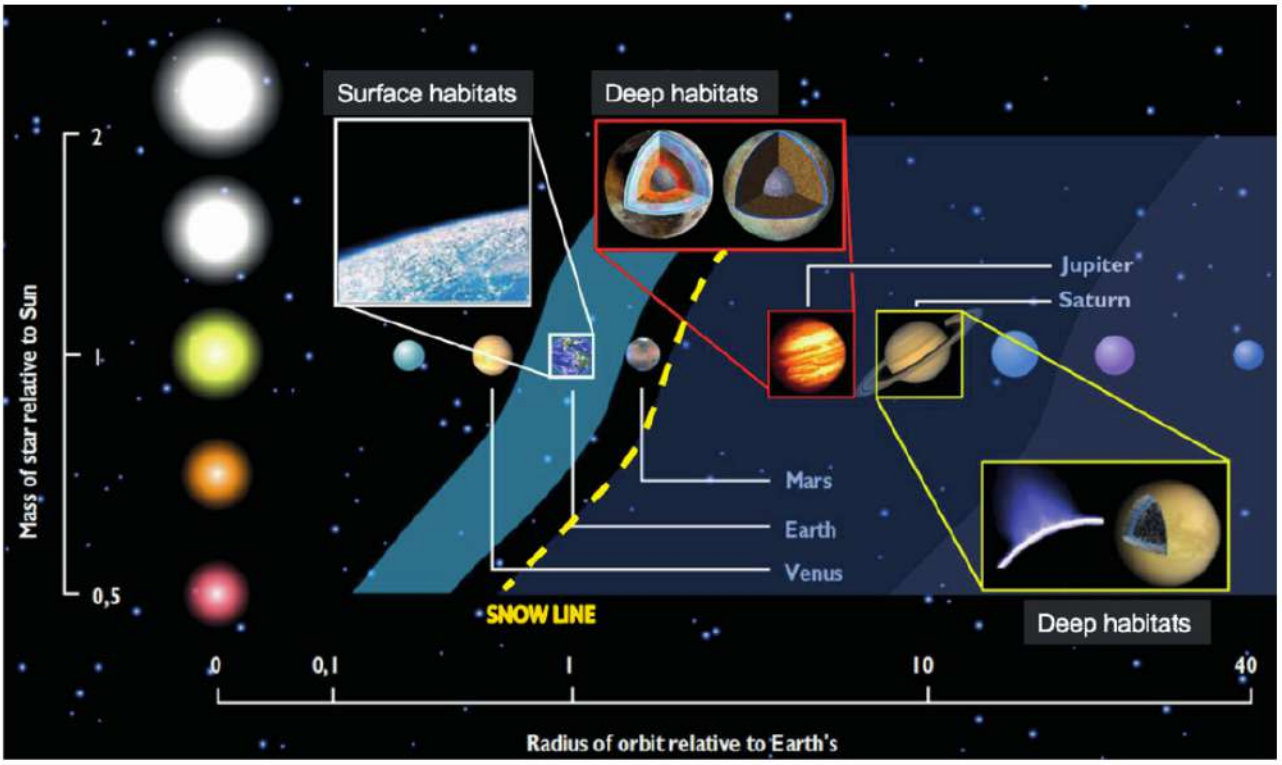

Figure 1-3. Historically, the habitable zone emphasized only surface habitats where liquid water could exist. Following the discovery of Enceladus's ocean, deep habitats, sustained by internal heat sources such as radiogenic decay and tidal heating, have gained attention. (Adapted from Grasset et al., 2013)

1.2 Exploration of Ocean Worlds

Despite the umbrella term “ocean worlds exploration,” Enceladus remains the only body at present for which a rocky core connected to a subsurface ocean has been robustly established with especially high astrobiological potential. Accordingly, the immediate scientific goal for other candidate ocean worlds is to test for the presence of interior oceans. As summarized by Nimmo & Pappalardo (2016), principal approaches include:

A. Determining global composition and structure via bulk density and moment of inertia to assess the plausibility of an interior ocean.

B. Geophysical tests for ocean detection, including

   a. Induced magnetic fields
   b. Geodesy (e.g., libration, tidal deformation)
   c. Radar sounding
   d. Surface geomorphology
   e. Compositional analyses

1.2.1 Bulk Density and Moment of Inertia

Icy satellites are mixtures of ice and rock; bulk density thus constrains their average rock/ice ratio and porosity. The moment of inertia (MoI) quantifies mass distribution relative to the rotation axis: a homogeneous sphere has MoI = 0.4, whereas differentiated bodies, heavy materials concentrated toward the center, lighter materials outward, have MoI < 0.4. This metric has yielded numerous insights into internal structure. For icy bodies, it is particularly important to determine whether they are differentiated into a rocky core and an overlying ice layer that may host an ocean. For example, the Jovian satellites Io, Europa, and Ganymede have MoI values of 0.378, 0.330, and 0.3105,

respectively—indicative of differentiated interiors, whereas Callisto's MoI of 0.406 suggests a more uniform interior (Anderson et al., 2001). The Saturnian moons Enceladus and Titan have MoI of ~0.34 – 0.36 (Less et al., 2014) and 0.34 (Gao & Stevenson, 2013), respectively, consistent with differentiated structures. Because internal oceans require differentiation at a minimum, spacecraft gravity measurements to determine bulk density and MoI are foundational.

1.2.2 Planetary-Physics Techniques

For bodies that satisfy minimal criteria for harboring an ocean based on density and MoI, the next step is to test ocean presence using planetary-physics methods: induced magnetism, libration/tides (geodesy), radar sounding, surface morphology, and compositional analysis. Here we briefly describe the last of these, which will be central to biosignature investigations in Section 1.3 onward.

Among available techniques, compositional analysis most directly indicates the possibility of interior oceans. For example, spectroscopy by Galileo's Near Infrared Mapping Spectrometer (NIMS) revealed sulfate hydrates on the surfaces of Ganymede and Europa, indirectly supporting the presence of interior oceans (Carlson et al., 2005).

When plumes are present, their analysis is paramount. While plumes can, in principle, arise from other sources than an ocean, Cassini's CDA and INMS provided a decisive demonstration on Enceladus by analyzing the plume's particulate and gaseous constituents (Hsu et al., 2015; Waite et al., 2017). If a plume originates from an interior ocean, in-orbit analysis can yield materials-science information about the ocean without landing, enabling not only ocean detection but also an assessment of habitability, a uniquely powerful approach at present. Plumes believed to emanate from interior processes have been reported at Io, Europa, Enceladus, and Triton (McEwen et al., 1998; Sparks et al., 2016; Waite et al., 2006; Kirk et al., 1995). For Europa Clipper (launched in 2024), key instruments for compositional analysis include the Surface Dust Analyzer (SUDA)

(Kempf, 2018) and the MAss SPectrometer for Planetary EXploration (MASPEX) (Waite et al., 2019).

1.3 Biosignature Investigations

Once interior oceans are established with high confidence (as in Section 1.2.2), the next phase is to assess whether those oceans could host life. Central to this phase is the concept of biosignatures whose presence would indicate life in a given environment. However, there is no unified view of what constitutes a biosignature, nor do we even possess a universally accepted definition of life. To build consensus criteria for ocean world missions, discussions by the Network for Life Detection (NfoLD), a community of planetary, Earth, and life scientists anchored by NASA, have proceeded on the basis of NASA's working definition of life as "a self-sustaining chemical system capable of Darwinian evolution" (e.g., Som, 2019; Neveu et al., 2020). Here, Darwinian evolution refers to the heritable change of traits across generations that maintains advantageous traits in a given environment.

1.3.1 A Framework for Life Detection

Among the proposed frameworks, Neveu et al. (2018) introduced the "Ladder of Life Detection," which organizes features related to life, organs/components of organisms and fundamental properties such as reproduction, growth, and metabolism into hierarchical levels and lists eight criteria by each of which can be judged as indicative of biology (Figure 1-4). The levels include:

- **Darwinian Evolution.** Essential by NASA's definition, but not realistically measurable in situ in unexplored environments because it unfolds over many generations as conditions change.

- **Growth & Reproduction.** Central biological traits, although not unique to life, have the potential for false positives.

- **Metabolism (metabolic products).** Living systems obtain energy from their environment and convert it to forms that support maintenance, growth, reproduction, and repair. Departures from non-biological steady states (including isotopic disequilibria) can evidence biological activity.

- **Molecules & Structures Conferring Function.** Macromolecules and specific structures supporting information storage/transfer and catalysis (e.g., DNA, RNA, proteins). Homochirality (D-sugars, L-amino acids for most terrestrial life) is a key characteristic.

- **Potential Biomolecule Components.** ATP, PAHs, lipids, nucleobases, amino acids, and other organics. Less specifically biological than the previous category, but often easier to detect.

- **Potential Metabolic Byproducts.** Variations in geologic distributions of elements that are rare in biomass but essential at enzyme active sites (V, Fe, Ni, Mo, W, Co, S, Se, P, etc.). Often readily detectable but require a robust biological context.

- **Biofabrics.** Environmental structures formed by microbial communities, e.g., stromatolites and other microbially induced sedimentary structures.

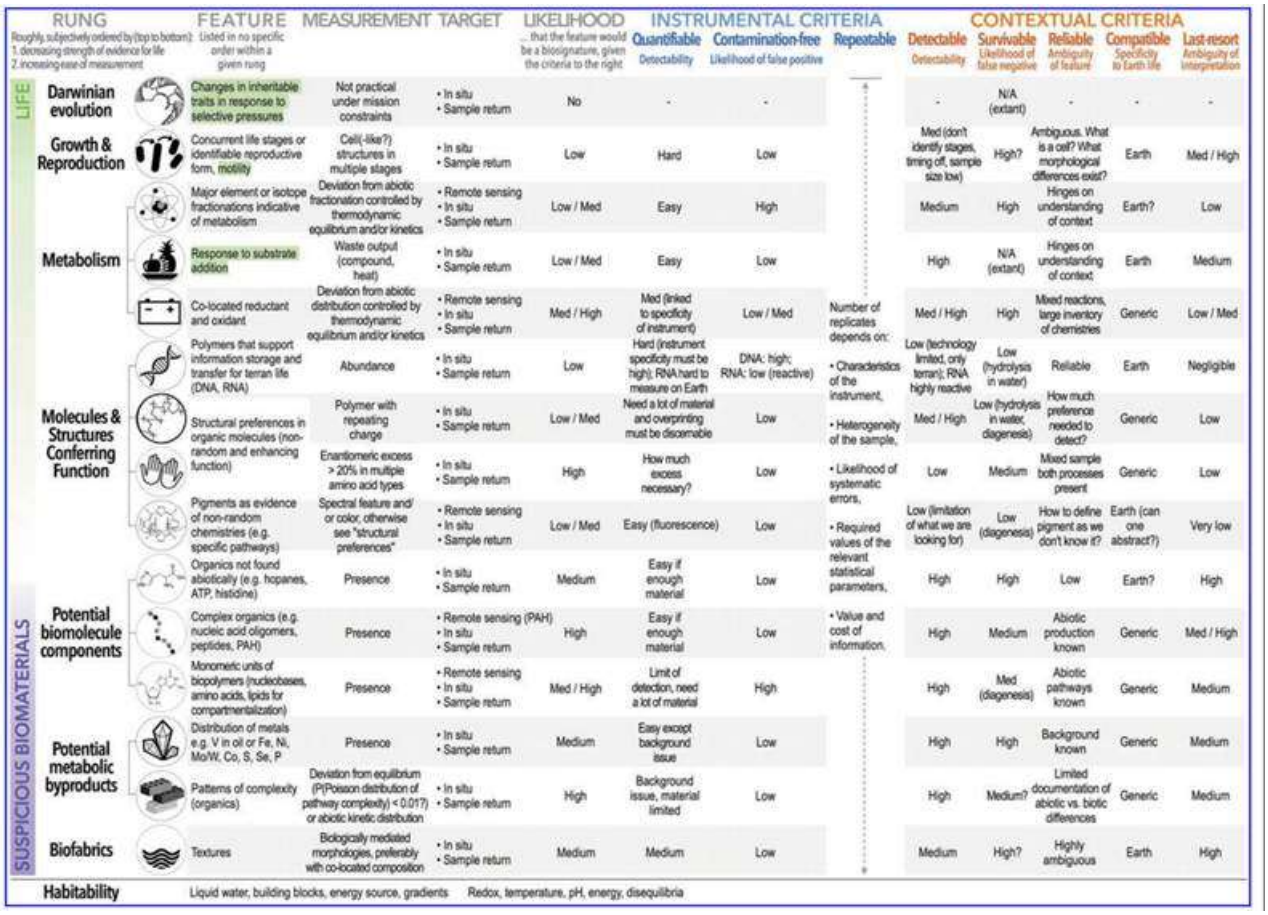

Figure 1-4. Matrix summarizing the Ladder of Life Detection (Neveu et al., 2018).

Each ladder level is evaluated against eight criteria:

1. Quantifiable (instrument sensitivity sufficient)
2. Contamination free
3. Repeatable
4. Detectable (features can be extracted from the measured data)
5. Survivable (no alteration between sampling and analysis)
6. Reliable (biological origin significantly more likely than abiotic)
7. Compatible (not excessively divergent from known terrestrial life)
8. Last resort (no plausible non-biological explanation)

1.3.2 Biosignatures Based on Biomolecules

While the ladder is systematic and comprehensive, it remains a framework for discussing biosignatures. For specific molecular targets such as sugars and amino acids (i.e., category "E. Potential biomolecule components"), more concrete evaluative criteria can be applied including the three key molecular attributes proposed by Glavin et al. (2019) for distinguishing biological from abiotic origins (Figure 1-5). They consider the following: (i) whether molecular distributions plausibly reflect biological byproducts; (ii) whether molecular chirality shows enantiomeric excess characteristic of life; and (iii) whether light-element isotopic anomalies (H, C, N, O) are present. In the Tagish Lake meteorite, for instance, although an L-excess of 43–59% was observed, the abundance of non-proteinogenic amino acids and elevated ^{13}C argued for an abiotic origin (Glavin et al., 2012).

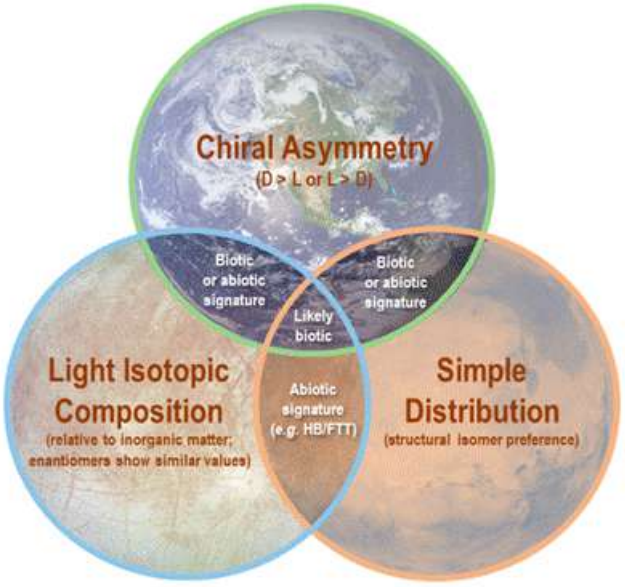

Figure 1-5. "Three key molecular attributes of amino acids and sugars" as candidate biosignatures based on biomolecules (Glavin et al., 2019).

1.4 Flyby Sampling

Section 1.2 outlined scientific benchmarks for future biosignature searches. The analytical instrumentation that can be deployed to achieve these benchmarks, however, depends strongly on mission architecture, particularly the relative velocity between target and spacecraft. Some missions such as Hayabusa and Hayabusa2 rendezvoused and touched down at their targets at relative velocity ≈ 0 to collect samples for Earth-based analysis (Yano, et al., 2006; Yurimoto et al., 2011; Yada et al., 2022). Others landed and conducted in-situ analyses with on-board GC-MS (e.g., Rosetta's Philae; Glassmeier et al., 2007) or rover-borne instruments (e.g., Mars rover Perseverance; Farley et al., 2020). By contrast, Cassini's relative speed through the Enceladus plume was 4–20 km s^{-1}, yet it still achieved remarkable science under the constraints of an hypervelocity flyby (Hsu et al., 2015; Waite et al., 2017).

Looking ahead, biosignature missions naturally bifurcate into two approaches:

I. Large landing missions that slow relative speed to enable detailed in-situ analysis or sample return.

II. Flyby missions that do not slow relative speed but collect material for improved in-situ analysis and/or sample return.

The Enceladus Orbilander, ranked second among flagship priorities in the Planetary Decadal Survey 2023–2032 (National Academies of Sciences, 2022), typifies approach (I). Such missions, however, entail long lead times and infrequent opportunities, perhaps once every several decades for a single target, limiting agility. By contrast, JAXA's DESTINY+ to a dormant comet typifies approach (II): smaller spacecraft can enable low-cost, higher-cadence deep-space exploration, complementing (I). This work, therefore, develops the flyby approach (II) in detail.

1.4 Flyby Sampling

1.4.1 Trade-offs of Flyby Missions

Flybys simplify overall mission design, enabling lower cost and higher cadence relative to rendezvous/landing missions. Landing missions must enter a target's sphere of influence and execute rendezvous operations, demanding more complex navigation and often more propellant. Sampling and surface operations further complicate the system and increase requirements for thermal control, communications, and power, generally driving missions to larger scale, higher cost, and longer preparation. Few space agencies can routinely field such missions.

By contrast, flybys, especially free-return trajectories that avoid capture by the target's gravity, impose far smaller navigation and propellant demands. Simpler spacecraft operations also ease thermal control, communications, and power requirements. These benefits become even more pronounced in the outer region of the Solar System, where low solar flux challenges power generation.

The key challenge for flyby missions is that they do not substantially reduce the relative velocity between the spacecraft and sampled material, in contrast to dedicated rendezvous missions such as orbiters or landers. For instance, Cassini's closest approaches to Saturn occurred at altitudes of ~2000 km (inside the D ring), with flyby speeds of ≈30 km s^{-1} (Hsu et al., 2018). During Enceladus flybys at altitudes of tens of kilometers, Cassini's encounter speeds were 7–18 km s^{-1} (Khawaja et al., 2019). In contrast, an orbiter around Enceladus could in principle sample plume material at significantly lower relative velocities, below 0.5 km s^{-1}, depending on the orbital configuration (Burchell & Wozniakiewicz, 2024). Nevertheless, even at encounter velocities exceeding ~10 km s^{-1}, flyby missions must be designed to extract scientifically valuable information. To analyze samples from plumes or atmospheres under such conditions, future missions must

employ either impact-based in situ mass spectrometry or the capture of products generated by hypervelocity impacts (typically exceeding a few km s^{-1}).

1.4.2 In-situ Mass Spectrometry Using Hypervelocity Impacts

When a hypervelocity particle strikes a spacecraft surface, it produces a suite of impact products shown schematically in Figure 1-6: plasma, gases, and solid fragments derived from both the projectile and the impacted surface (Ahrens & O'Keefe, 1972). Instruments such as Cassini's CDA (Srama et al., 2004) and INMS (Waite Jr et al., 2004) perform in situ mass spectrometry on these secondary plasmas and gases and have a proven record in the past ocean world exploration missions.

Prior to Cassini, several impact-ionization dust mass spectrometers employing similar design concepts were successfully flown in cometary missions. The Particular Impact Analyser (PIA) (Kissel, 1986) and the Dust Impact Mass Analyzer (PUMA) (Krueger and Kissel, 1987) aboard the Giotto spacecraft at Comet Halley, as well as the Cometary and Interstellar Dust Analyzer (CIDA) (Kissel et al., 2004) on the Stardust mission to Comet Wild-2, all utilized impact ionization to analyze solid dust particles. At Comet Halley, encounter velocities reached approximately 70 km s^{-1} (Hughes, 1987), resulting predominantly in atomistic mass spectra due to extreme impact-induced fragmentation (Krueger and Kissel, 1987). In contrast, CIDA experienced much lower encounter velocities of about 6.1 km s^{-1} at Comet Wild-2 (Kissel et al., 2001), enabling the detection of more complex molecular fragments (Krueger and Kissel, 2006). These missions demonstrated that the degree of molecular fragmentation in impact ionization mass spectrometry strongly depends on the impact velocity, providing an important foundation for interpreting later Cassini CDA observations.

With the biosignature context summarized in Section 1.3, we briefly review Cassini CDA/INMS results for the Enceladus ocean and outline resultant instrument requirements.

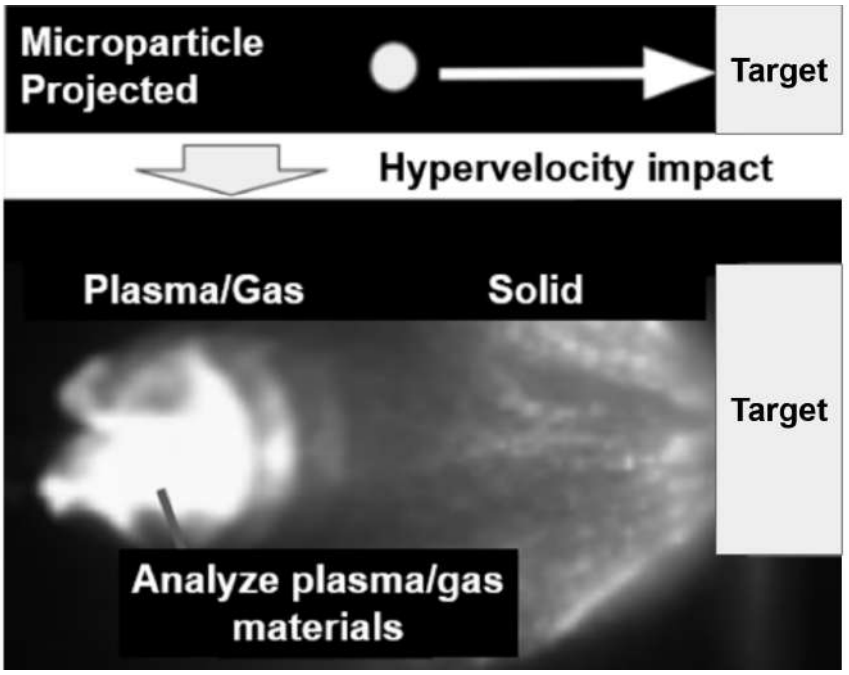

Figure 1-6. Hypervelocity impact between a solid particle and a solid target, and the resulting products. (Adapted from Fuse et al., 2020)

1.4.2.1 Cassini CDA (Cosmic Dust Analyzer)

The Cosmic Dust Analyzer (CDA) is an impact-ionization time-of-flight mass spectrometer (ToF-MS) designed to analyze solid microparticles striking the instrument's target section at hypervelocity (Figure 1-7). Microparticles entering through the aperture at speeds of several km s^{-1} or more impact a concave rhodium (Rh) target; impact compression heats the microparticles and produces a mixed gas–plasma cloud. When the impact occurs on the central QA (Chemical Analyzer) grid on the concave floor (right panel of Figure 1-7), the plasma is accelerated across a 3-mm gap by +1000 V toward the QI (Ion Collector), which is biased at −350 V and located near the focal point of the concave reflector. The flight time from QA to QI depends on the mass-to-charge ratio, enabling mass spectrometry with a resolving power of $m/\Delta m \approx 20–50$ (Postberg et al., 2018).

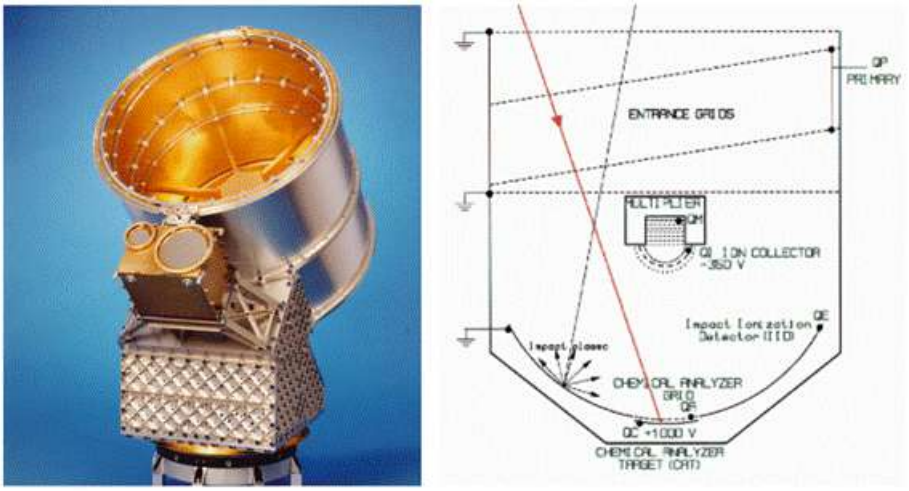

Figure 1-7. Configuration of Cassini CDA (Srama et al., 2004).

CDA elemental analyses revealed nanosilica (SiO_2) particles in Saturn's E ring, thought to derive from Enceladus's plume (Hsu et al., 2015), consistent with high-temperature water–rock interactions through hydrothermal activities on the seafloor. CDA also indicated the presence of abundant organics in the plume (Figure 7a; Postberg et al., 2018) and detected phosphates, which can be a key element for life detection (Postberg et al., 2023). However, as the flight instrument with $m/\Delta m \approx 20–50$, CDA could not resolve exact masses or structures of the detected organics to modern laboratory standards.

Figure 1-8(a) shows a mass spectra of the Enceladus plume measured by CDA. Cluster series at ~18 amu intervals are attributable to water clusters. Because impact-produced plasmas experience high internal energies, molecules undergo ionization while forming clusters of various sizes. CDA also analyzed organics in Saturn's E ring particles (Figure 1-8b; Hsu et al., 2018). Yet, owing to the extremely high encounter speeds (~30 km s^{-1}) between Cassini and the ring particles, CDA detected primarily peaks from water and carbon; organics were likely fragmented upon impact (Hsu et al., 2018). The strong dependence of impact-ionization mass spectra on encounter velocity,

including enhanced fragmentation at higher speeds, had already been demonstrated using engineering models of CDA prior to the Cassini mission (Goldsworthy et al., 2002, 2003). Thus, with CDA, (1) limited resolving power (m/Δm ≈ 20–50) and (2) impact-induced fragmentation hindered detailed molecular identification, even when the presence of organics was clear.

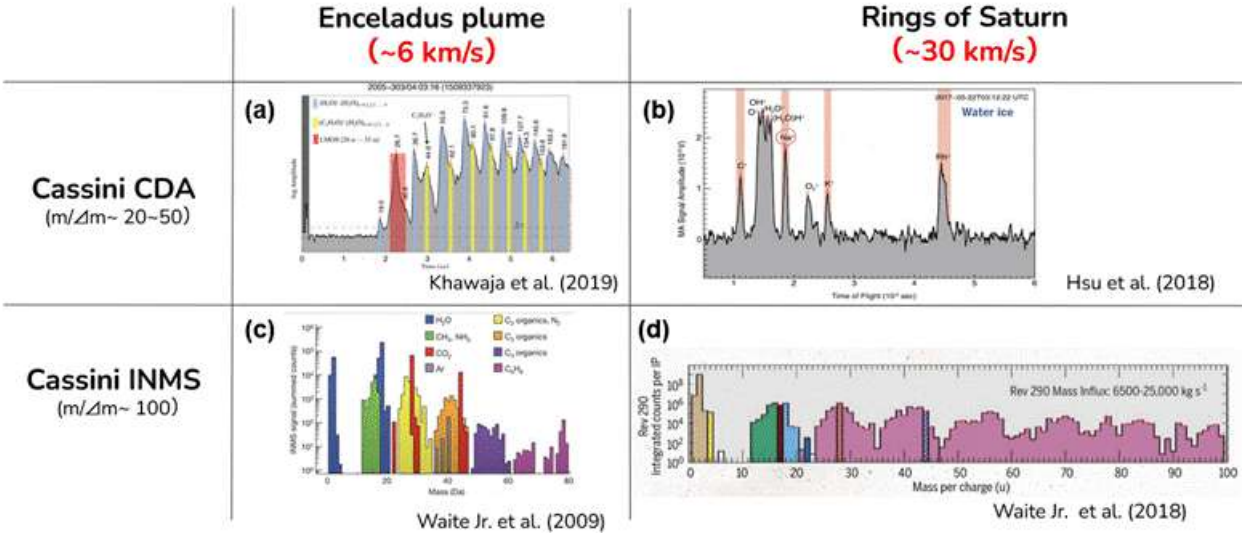

Figure 1-8. Comparison of impact ionization mass spectra measured by Cassini instruments under different encounter velocities. Panels (a) and (c) show mass spectra obtained during Cassini flybys of the Enceladus plume, where the typical relative impact velocity was ~6 km s^{-1}, measured by the Cosmic Dust Analyzer (CDA; m/Δm ≈ 20–50) and the Ion and Neutral Mass Spectrometer (INMS; m/Δm ≈ 100), respectively. Panels (b) and (d) show mass spectra obtained during crossings of Saturn's rings at much higher relative velocities of ~30 km s^{-1}, measured by CDA and INMS, respectively. Panels (a)–(d) are adapted from Khawaja et al. (2019), Hsu et al. (2018), Waite Jr. et al. (2009), and Waite Jr. et al. (2018), respectively.

1.4.2.2 Cassini INMS (Ion and Neutral Mass Spectrometer)

Unlike CDA, INMS ingests ions or neutral gases through two inlets (open and closed sources) and analyzes them with a quadrupole mass spectroscopy(MS) (Teolis et al., 2015). In the closed source mode in Figure 1-9, neutrals are collected in the red-shaded antechamber, then ionized by the orange-shaded electron gun and sent to the quadrupole. The open source has modes for both ions and highly reactive neutrals; samples are collimated by the yellow-green slit, pooled in the blue region, then ionized by the electron gun before quadrupole analysis.

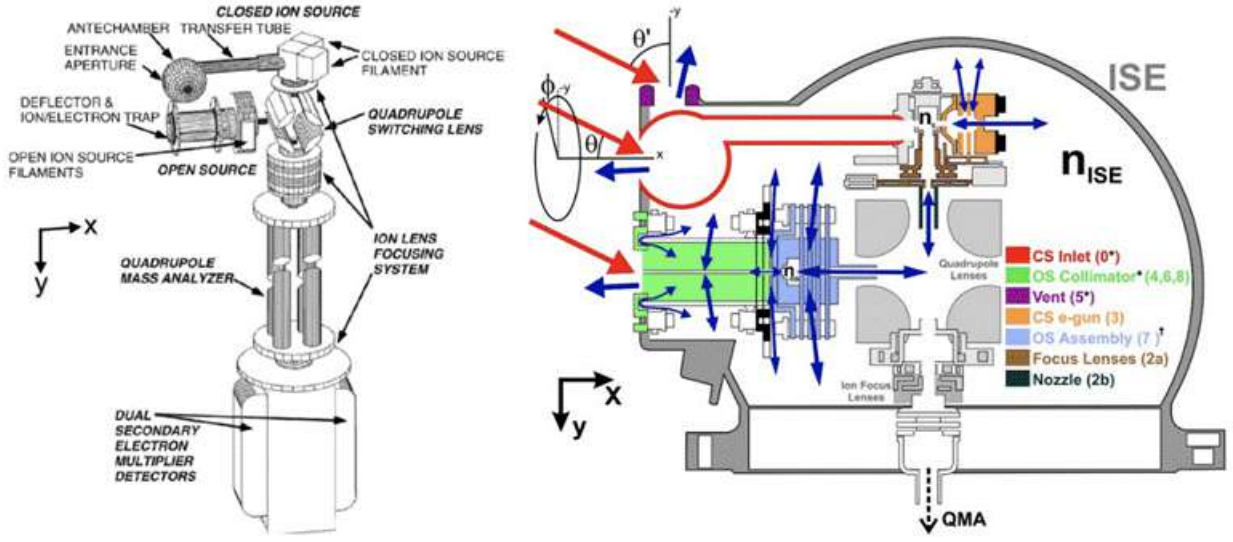

Figure 1-9. Configuration of Cassini INMS (Teolis et al., 2015).

INMS was originally intended for analyzing Saturn's and Titan's upper atmospheres, but proved fully capable of analyzing impact-induced gas by Enceladus's plume particles. Waite et al. (2009) reported organics and the noble gas argon (Figure 1-8(c)) and inferred that Enceladus's ice might share origins with cometary ices based on the D/H ratio in H_2O. Crucially, INMS detected molecular hydrogen (H_2) in the impact-induced gas by the plume particles (Waite et al., 2017),

indicating ongoing hydrothermal reactions involving reduced minerals and/or organics and a thermodynamic disequilibrium favorable to methanation (i.e., conversion of CO_2 to CH_4) within Enceladus's ocean.

During Cassini's crossings to the ring at a high encountering velocity of ~30 km s^{-1}, INMS ($m/\Delta m \approx 100$) still detected organics below $m/z \approx 100$(Figure 1-8d; Waite Jr. et al., 2018). Because impact desorption imparts less energy than impact ionization, fragmentation of organic molecules was reduced. Nevertheless, INMS still required 70 eV electron ionization, inevitably causing some fragmentation; thus, fully preserving molecular structures during the flybys remained challenging.

Consequently, while Cassini established the presence of organics without any doubt, energetics of detection mechanisms and instrumental resolution limited the details of molecular identification. These lessons emphasize the need for higher resolution MS and a deeper understanding of impact processes for in-situ mass spectroscopy in future icy moon exploration.

1.5 Positioning of This Study

In nearly half a century, spaceborne mass spectrometry has advanced remarkably. Early magnetic-sector and quadrupole instruments have given way to time-of-flight (ToF) and ion-trap analyzers with higher resolving power and wider mass ranges (Arevalo Jr. et al., 2020), enabling identification of complex organics in planetary atmospheres and icy moon plumes (Figure 1-10). However, these improvements have centered primarily on detector performance. The impact processes that generate the observed signals have seen comparatively little optimization.

For the Europa Clipper mission, the ToF-MS SUDA is designed to analyze hypervelocity dust impacts and still relies on impact ionization, under which microparticles are expected to be

fully ionized and heavily fragmented at encounter velocities of several to tens of km s^{-1} (Kempf et al., 2025). Designed for neutral gas analysis, MASPEX is a state-of-the-art spaceborne mass spectrometer. This instrument is substantially larger and more resource-intensive than conventional spaceborne mass spectrometers, with a mass of approximately 65 kg and a power consumption of about 91 W (Srinivasan et al., 2025). MASPEX achieves a dynamic range of ~10^6 and a mass resolving power on the order of 17,000 ($m/\Delta m$) at the 10% valley (Waite Jr. et al., 2024), far exceeding the performance of traditional flight mass spectrometers, which typically have masses of ~20 kg and power budgets of ~30 W. However, MASPEX still employs electron ionization, which intrinsically induces molecular fragmentation (Brockwell et al., 2016). Thus, even with the state-of-the-art spaceborne mass spectrometry, information lost to fragmentation at the moment of impact or ionization cannot be recovered. Overcoming this limitation requires not only improved detector performance but also a physical understanding and control of the impact and ionization processes themselves.

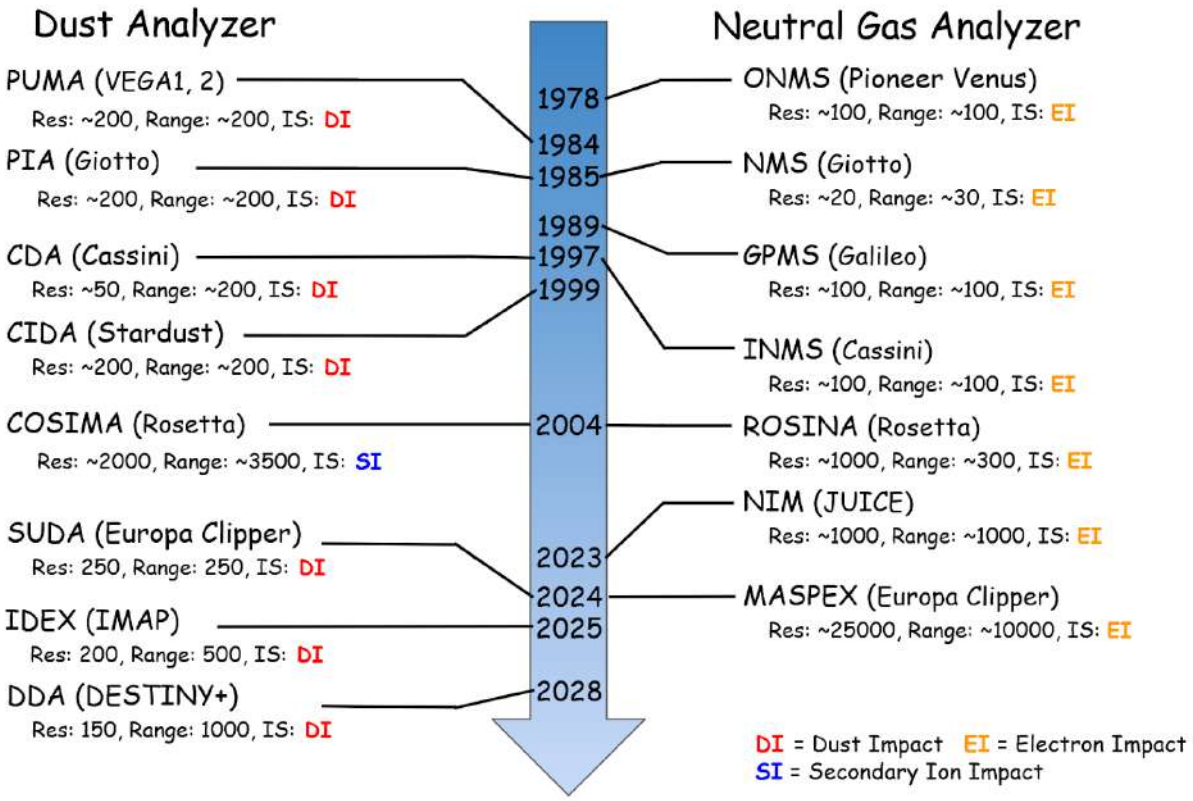

Figure 1-10. History of In-situ Mass Spectrometers for Impact Ionization (left) and Neutral Gas Analysis (right) onboard the Past and Present Spacecraft.

1.6 Structure of This Dissertation

1.6.1 Overview

This dissertation focuses on the analysis of neutral gases generated by dust impacts, intending to experimentally demonstrate that neutral gas analysis results in relatively mild molecular fragmentation, compared to plasma-based analysis. As an extension, the study evaluates mass spectrometric techniques that combine neutral gas analysis with non-destructive ionization methods other than electron ionization (EI), in order to contribute to the advancement of high accuracy organic analysis in future planetary missions.

This dissertation is structured around two main themes. The first part (Chapters 2–3) establishes the theoretical and numerical framework for understanding ionization and sublimation in hypervelocity impacts. The second part (Chapters 4–5) presents experimental investigations focusing on neutral gas analysis and soft ionization techniques. A brief overview of each part is summarized below.

1.6.2 Detailed Outlines by Each Chapter

1.6.2.1 Understanding Ionization and Sublimation Processes in Hypervelocity Impacts

Directly reproducing ionization and emission phenomena caused by hypervelocity impacts in laboratory experiments is extremely challenging, since no existing facilities can accelerate micrometer-scale or larger particles to velocities exceeding 20 km s^{-1} as a typical encountering velocity between spacecraft and microparticles during flybys to exploration targets. Therefore, this study employs high-temperature and high-pressure conditions generated by laser irradiation as an analogue to such hypervelocity impacts and examines their correspondence through numerical simulations.

Chapter 2 describes the fundamentals of the radiation-hydrodynamics code P4P (PINOCO for Plasma Processing and Planetary Physics), its adaptation for simulating hypervelocity impacts, and calibration against experimental data from Ratcliff et al. (1997). The two-temperature (electron/ion) model, based on the QEOS (quotidian equation of state), enables quantitative treatment of non-equilibrium plasma formation during impact.

Chapter 3 employs P4P to reproduce, in silico, both laser irradiation and hypervelocity impact conditions comparable to those in Klenner et al. (2019). By comparing the resulting

thermodynamic states and ion yields, the chapter establishes a theoretical correspondence between the two processes, providing a quantitative basis for using laser ablation as an analog for hypervelocity impacts.

1.6.2.2 Analysis of Neutral Gases Generated by Dust Impacts

Building upon the theoretical and numerical results above, this study conducted laser-driven analog experiments combining P4P simulations and mass spectrometric observations to assess the feasibility of analyzing impact-sublimated materials. And as an extension, photoionization (PI) mass spectrometry was developed and evaluated as a less destructive alternative to conventional EI.

Chapter 4 presents laboratory experiments designed to test the central hypothesis that analysis of impact-sublimated gas leads to less molecular fragmentation than direct plasma analysis. Laser-driven impact-analog experiments are combined with electron-impact (EI) mass spectrometry, and the resulting spectra are compared with benchmark data from Van de Graaff accelerator impact experiments (Srama et al., 2009). The results confirm that gas-phase MS can preserve molecular structures more effectively under equivalent energy conditions.

Chapter 5 introduces and characterizes a custom-built photoionization mass spectrometry (PI-MS) system as a softer ionization technique for analyzing impact-generated gases. By comparing the sensitivity and fragmentation behavior of PI and EI under conditions similar to typical spacecraft missions, this chapter evaluates the feasibility of PI-MS for future planetary missions.

Finally, **Chapter 6** synthesizes all the results, discusses their implications for spacecraft-borne MS instrumentation, and outlines future directions including integration with high-resolution analyzers (e.g., ToF, MULTUM, Orbitrap), testing under space environment constraints, and applications to biosignature detection missions.

The candidate was responsible for the development, implementation, and execution of all numerical simulations using the P4P code presented in Chapters 2–4, including model construction, parameter selection, and post-processing analysis. The candidate also designed and conducted the laser-driven experiments described in Chapters 4 and 5, developed the photoionization mass spectrometry (PI-MS) system, and performed all mass spectrometric measurements and data analyses. All interpretation of the results, figure preparation, and writing of this dissertation were carried out by the candidate.

Chapter 2. Modeling and Verification of Hypervelocity Impact Ionization Phenomena Using the P4P Code

2.1 Overview of Hypervelocity Impact Ionization and Numerical Modeling Approaches

In view of the research objectives and overall structure described in the previous chapter, this chapter presents the details of the P4P code that was constructed to numerically analyze hypervelocity impact ionization phenomena. In the following sections, the background of this study and the positioning of numerical analysis are outlined together with the flow of related studies.

Hypervelocity impacts typically generate intense plasma, ionization, and electromagnetic radiation (e. g. Grün et al., 1992). Ion yield, optical flashes, and radio-frequency (RF) emissions serve as valuable diagnostic tools for estimating impact conditions such as velocity, mass, and material composition (Ratcliff et al., 1997; Goel et al., 2015), critical parameters for spacecraft design, space environment monitoring, and future planetary exploration.

To investigate and simulate, laboratory studies have been conducted using both light–gas guns (LGGs) and electrostatic dust accelerators since Friichtenicht and Slattery(1963), LGG experiments at a few km s^{-1} under medium vacuum conditions (~0.1 Torr) mainly capture ejecta–gas–driven optical flashes (e.g., Schultz 1996; Sugita et al. 1998; Sugita and Schultz, 1999; Bergeron et al. 2006; Mihaly et al. 2013; Tandy et al. 2014, 2020; Schultz and Eberhardy 2015; Yafei et al. 2019,2021; Simpson et al., 2023). In contrast, electrostatic dust accelerators shot micrometer- and sub-micrometer-sized particles to tens of km s^{-1} in high vacuum (<10^{-5} Torr), enabling detailed diagnostics of plasma expansion (e.g., Eichhorn 1976; Krüger and Kissel 1984;

Krüger 1984; Kissel and Krüger 1986; Burchell et al. 1996; 1999; Ratcliff et al., 1997; Crawford and Schultz ,1999; Lee, 2012; Close et al., 2013; Goel, 2015; Tarantino, 2018; Hew et al., 2021). However, owing to the inverse coupling between particle size and velocity in electrostatic dust accelerators, laboratory experiments cannot reproduce all of the velocity–size distributions expected in natural environments. Researchers predict impact plasma yields with extrapolation of empirically constrained scaling laws obtained by these experiments, even though the governing physics and their capabilities are still unknown. Consequently, numerical simulations are indispensable for predicting impact-plasma yields across the relevant parameter space and for probing the underlying physics.

However, faithfully capturing these processes is difficult: the response couples strong gradients, phase changes, and ionization with pronounced departures from local thermal equilibrium (LTE). Consequently, LTE-based models reproduce only exceptional cases (e.g., large-scale vacuum expansion of ion clouds (Sugita et al., 2003; Zhang et al., 2016) and generally fail elsewhere, underscoring the need for explicitly non-equilibrium formulation (Kissel and Krüger, 1987). A critical component of numerical simulation is the equation of state (EOS). Classical forms such as Mie–Grüneisen EOS (Shawoon et al., 2019; Katayama et al., 2017) and Tillotson EOS (Tillotson 1962; Brundage, 2013) are tractable for high-pressure behavior but provide limited temperature dependence and no rigorous treatment of phase transitions; ANEOS (Melosh 2007) includes ionization physics (Saha/Thomas–Fermi) but assumes thermal equilibrium ($T_e = T_i$), which is incompatible with the immediate two-temperature state after hypervelocity impact. Recent efforts move beyond Ratcliff et al. (1997), who used Tillotson to infer an ionization threshold, to SPH with a non-ideal Saha and Griem corrections (Fletcher et al., 2015), to solid-state/TF hybrids (Song et al., 2014; 2016), and Gray three-phase EOS consistent with TF (Zhao et al., 2025), but still assumes thermal equilibrium ($T_e = T_i$). While these frameworks reproduce aspects of the data, they still struggle to match the observed velocity dependence across regimes.

In this chapter, the radiation-hydrodynamics code P4P (PINOCO for Plasma Processing and Planetary Physics), which is based on PINOCO (Nagatomo et al., 2006; 2015) is used and an electron–ion two-temperature model with the QEOS (quotidian equation of state) for partially ionized matter is implemented. This study simulates the impact experiments by Ratcliff et al. (1997) using an electrostatic dust accelerator that shoots iron projectiles onto rhodium targets under high vacuum conditions, and investigates the spatiotemporal evolution of ion yield, energy distribution, and charge state, and compare the results with the experimental dataset of the experiment, which provides a benchmark for validating the velocity dependence of impact-induced ionization. The objective of this chapter is to elucidate the role of non-equilibrium plasma physics and geometric factors in shaping measurable impact signatures and to provide a more physically grounded modeling framework for interpreting hypervelocity impact phenomena in space environments. The configuration of the P4P code and the implemented physical models are described in the following sections.

2.2 P4P Code

2.2.1 Data from the Previous Studies

In Ratcliff et al., iron microparticles are projected onto rhodium foils at the velocity of 3 – 50 km s^{-1}. The target was inclined at an angle of 36° to the incident particle beam, allowing the positive ions to be focused onto an electron multiplier mounted in a tube attached to another port in the chamber. Electrostatic field pulled ions generated by impacts, and at that time, the ion yield was measured by the turbulence of the potential of the accelerating grid. After a while, ions drift in the vacuum chamber and are detected by the electron multiplier. The time of drifting differs from the mass to charge ratio of ions, and they obtained mass spectra of impact-induced ions (Figure 2-1).

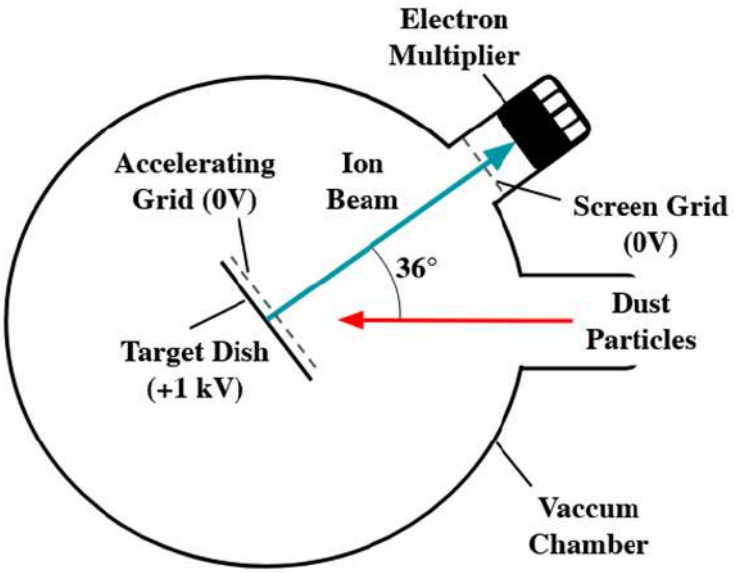

Figure 2-1. Experimental configuration adapted from Ratcliff et al. (1997).

As a result of this study, the scaling law of ion yield Q is described;

$$Q = cm^{\alpha} v^{\beta} \qquad (2\text{-}1)$$

where m is the projectile mass, v is the impact velocity, and c, α, and β are constants. The best statistical fits to the data obtained by Ratcliff et al. are 8.5 x 10^3, 1, and 4.74 for c, α, and β, respectively (for Q measured in Coulombs, m in kg, and v in km s^{-1}). The values of β vary with different materials, staying in a wide range of 2.74–4.75, and commonly it is in the range of 3.5–4.0, according to the reported result (Ratcliff et al., 1997; Burchell et al., 1999; Mocker et al., 2013; Song et al., 2016). Burchell et al. also conducted impact experiments using iron projectiles and rhodium targets, reporting 4.4 x 10^{-3}, 1, and 4.82 for c, α, and β, respectively.

According to the experiments, at low impact velocities (below 15 km s^{-1}), the plasma is dominated by alkali metals such as sodium and potassium. These species are known to be surface contaminants and are frequently observed in impact plasma production processes governed by surface ionization (Dalmann et al., 1977; Mocker et al., 2013). At velocities above 20 km s^{-1}, hydrogen becomes the dominant species, and signals from projectile and target materials such as Fe and Rh become increasingly significant. Previous studies have suggested that the hydrogen signals may originate from hydrogen atoms adsorbed on the rhodium target surface (Kissel and Krueger, 1984; Postberg et al., 2009; Klenner et al., 2019). This velocity-dependent shift in species composition reflects a transition from surface-dominated ionization at low velocities to bulk vaporization and ionization of the projectile and target materials at higher velocities. Therefore, from now on, we will focus on the hypervelocity impact, whose velocities are above 20 km s^{-1}.

Table 2-1. Impact parameters in Ratcliff et al.(1997) with their experimental results.

Impact Velocity v [km s^{-1}]	**Projectile Radius r [nm]**	**Projectile Mass m [kg]**	**The characteristic timescale t_s ($=2r_p/v_{imp}$) [ps]**
23.0	48.3	3.69×10^{-18}	4.20
27.3	41.8	2.38×10^{-18}	3.06
33.6	34.5	1.34×10^{-18}	2.05
44.0	26.5	2.40×10^{-19}	1.20

2.2.2 Hydrocode Simulations

P4P is built upon the framework of the integrated implosion simulation code, two-dimensional Arbitrary-Lagrangian-Eulerian (ALE) radiation hydrodynamics code (PINOCO: Precision Integrated implosion Numerical Observation COde), developed initially at the Institute of Laser Engineering, the University of Osaka (e.g. Nagatomo et al., 2006; 2015). While inheriting the

multi-dimensional and multi-physics integrated structure of PINOCO, P4P has been restructured as a radiation hydrodynamic code specialized for high-energy density science employing fixed Cartesian coordinates.

In P4P, the energy of ions and electrons is treated separately based on a two-temperature radiation hydrodynamics model. The code self-consistently incorporates key physical processes, including electron and ion thermal conduction with flux-limited Spitzer–Härm conductivity (L. Spitzer and R. Harm 1953), multigroup diffusion approximation radiation transport (Mihalas and Barbara 1984), and electron-ion energy relaxation.

The equation of state (EOS) employed is based on the QEOS model (More et al., 1988) which explicitly describes the thermodynamic response of both electrons and ions. The total Helmholtz free energy $F(\rho,T_e,T_i)$ is composed as:

$$F(\rho,Te,Ti) = F_i(\rho,T_i) + F_e(\rho,T_e) + F_b(\rho,T_e) \qquad (2\text{-}2).$$

Here, Fi and Fe represent the free energy contributions from ions (Cowan, 1956) and electrons (Takabe 1993), respectively, while F_b accounts for the bound-state contributions. In QEOS, the ion thermodynamic properties described as F_i are treated independently of the electron properties described as F_e based on the assumption that ion motion can be separated from the electronic state. However, local charge neutrality is maintained within each ion cell. Therefore, the interaction of ions and electrons is implicitly included through the constraint. Additionally, QEOS employs correction for chemical bonding F_b to correct for limitations at low temperatures and solid densities, where the TF model can overestimate pressure. Furthermore, P4P initially calculated the Thomas–Fermi model for hydrogen (Eliezer et al., 1986), and extends to other materials via scaling (Takabe, 1993, Takami and Takabe, 1990) to handle multiple materials within a unified EOS framework. The material-specific parameters introduced are primarily used for this scaling, and the

bulk modulus is additionally used to characterize the bound-state contribution F_b related to chemical bonding. All relevant input parameters for QEOS are summarized in Table 2-2.

Table 2-2. QEOS parameters used in the hydrocode model

Material		ρ_0[g cm^{-3}]	Atomic Mass [g mol^{-1}]	Atomic Number	Bulk Modulus [GPa]
Iron	Projectile	7.86	55.847	26	166
Rhodium	Target	12.41	102.9055	45	380
Nitrogen	Ambient gas	1.137	14.0	7	--

The calculation is conducted in Eulerian coordinates, and the computational conditions are summarized in Table 2-3. The simulation domain consists of a high-resolution region around the impact point and an extended region with a coarser mesh. In the high-resolution region, a uniform mesh is employed to capture steep gradients in pressure and density accurately. In contrast, the extended region uses a geometrically expanding mesh to reduce computational cost while maintaining a sufficiently large domain to minimize the influence of boundary conditions. This design ensures that plasma expansion and shock wave propagation induced by the collision can be resolved appropriately while balancing computational efficiency. We assessed numerical convergence by varying the high-resolution grid size (Δx = 2.5, 0.5, and 0.2 nm) and found that coarse grids underestimate ion yield, particularly at low velocities (up to ~30% for Δx = 2.5 nm). Therefore, we use Δx = 0.2 nm for the main simulations (CPPR = 241–132 across 23–44 km/s). The simulations were advanced in time using an explicit scheme subject to the Courant–Friedrichs–Lewy (CFL) condition. The time step was dynamically adjusted to maintain CFL < 0.15 throughout the calculation.

In the actual experiment, a 1 kV potential is applied to the target, and a grounded electrostatic grid is placed 3.3 mm above the target surface. This configuration generates an electric field in the vicinity of the target, which influences ion extraction (Goel, 2016; Tarantino et al., 2018; Hew et al., 2021). However, this electric field will be effective after the plasma expands and becomes larger than its Debye length, which is the late stage of impact plasma generation and affects the shape of plasma clouds at the centimeter scale. Because of this statement, the effect of the electric field is neglected in the present simulation.

Additionally, the experimental setup involves an impact angle of 36° between the target surface and the incident particle beam. Despite this inclination, Ratcliff et al. argue that the angle has minimal influence on the ion yield or the energy and angular distribution of the ejected particles. Their justification refers to the findings of Krüger (1984), who performed the impact induced ion time-of-flight mass spectrometry experiments at the angle of 0° and 45°, and observed no significant differences. Furthermore, an angle of 36° is not sufficient to produce elliptical craters (Christiansen and Cykowski ,1993; Mackay et al., 1995; McDonnell 1993; Hayhurst et al., 1995), which are typically indicative of oblique impact effects. Based on these prior studies, we performed the P4P calculations assuming normal (vertical) incidence, without incorporating the experimental impact angle.

Table 2-3. Values of the main parameters used in the P4P simulations.

Parameters	Values
Δx	0.2 nm
Δy	0.2 nm
Cell per Projectile Radius	241 (48.3 nm for the 23.0 km s^{-1} impact) 208 (41.8 nm for the 27.3 km s^{-1} impact) 172 (36.5 nm for the 33.6 km s^{-1} impact) 132 (26.5 nm for the 44.0 km s^{-1} impact)
End Time	30 ps
High Resolution Zone Width	60 nm (300 cells)
High Resolution Zone Height	200 nm (1000 cells)
High Resolution Target Depth	100 nm (500 cells)
Extension Width	150 nm (150 cells)
Extension Top	200 nm (50 cells)
Extension Bottom	200 nm (100 cells)
Vacuum Level	5×10^{-5} Pa[35]

2.2.3 Analytical Method for Calculating Ionization Degree

Using these equations, we calculate the velocity, pressure, both the projectile and target mass densities, ion temperature, electron temperature, and ionization degree at each grid point. However, the QEOS is primarily designed for high-temperature plasma states such as those induced by laser heating or shock compression that reach several to tens of keV (More et al., 1988). Consequently, the ionization degree predicted by QEOS implicitly assumes complete ionization and cannot be directly compared with the ionization degree observed in partially ionized plasmas at a few eV formed in impact experiments like those by Ratcliff et al. (1997) Therefore, it is important to analytically reprocess the ionization output from QEOS in order to obtain a more appropriate estimate of the ionization degree for such conditions.

In Thomas–Fermi (TF) theory, electrons are treated as a charged fluid surrounding the nucleus, and in QEOS, the influence of the plasma environment is incorporated via the ion-sphere model (More et al., 1988). In this model, all electrons are assumed to exist within a spherical region of radius R_0, centered on the nucleus and defined by the ion number density n_i as $R_0 = (3/4\ \pi\ n_i)^{1/3}$. The electron number density distribution $n_0(r)$ is determined as a function of the radial position r within the ion sphere by integrating the product of the occupation probability f(r) and the density of states at a given energy level over the energy domain:

$$n_0(r) = \int_0^\infty c_1\, \epsilon^{\frac{1}{2}} f(r)\, d\epsilon \qquad (2\text{-}3).$$

Here, c_1 is a constant given by:

$$c_1 = \frac{1}{2\pi^2}\left(\frac{2m_e}{\hbar^2}\right)^{3/2} \qquad (2\text{-}4).$$

Moreover, f(r) is the Fermi–Dirac distribution function:

$$f(r) = \frac{1}{exp\left(\frac{\epsilon-\mu-V(r)}{k_B T_e}\right)+1} \qquad (2\text{-}5).$$

This function is defined by the electron temperature T_e, chemical potential μ, and the potential V(r) arising from the central nucleus and the surrounding electron cloud.

In conventional QEOS, electrons existing in the inner region ($r < R_0$) are considered core (deeply bound) electrons, while those at the outer edge ($r = R_0$) are regarded as valence and free electrons. Therefore, the ionization degree Z_0 is calculated based on the total number of valence and free electrons using the electron density at the ion-sphere boundary:

$$Z_0 = \left(\frac{4\pi}{3}\right) R_0^3 \, n_0(R_0) \qquad (2\text{-}6).$$

In principle, the outer edge of the ion sphere, where free and valence electrons are assumed to exist, is located at the bottom of the potential well, tens of eV below the vacuum level. In high-temperature plasmas (several to tens of keV), this potential barrier can be neglected, and valence and free electrons are thermally excited and almost certainly ionized. As such, their total number is treated as the ionization degree. However, in partially ionized plasmas generated by impact ionization, the electron temperature is on the order of several to several tens of eV. Therefore, it becomes necessary to count only those electrons at the boundary of the ion sphere that possess sufficient energy to overcome the potential barrier and consider only those as truly liberated into the plasma.

In the P4P system, the energy threshold separating bound and free electrons is, in principle, determined self-consistently through a Screened Hydrogenic Model (SHM)-based average-atom calculation (Slater 1930; Takabe and Nishikawa 1994) at each thermodynamic condition. However, for the weakly ionized plasmas considered in this study, variations in the deepest bound core levels due to temperature and density effects are expected to be small compared to their absolute binding energies. Accordingly, as a first-order approximation, we adopt experimentally measured core-level binding energies at ambient conditions, obtained from X-ray photoelectron spectroscopy (XPS), as a fixed reference for the depth of the potential barrier $V_{barrier}$. According to X-ray photoelectron spectroscopy (XPS) dataset (Crist, 2018), the corresponding energy levels are the 3p orbital for Iron (–53.0 eV) and the 4p orbital for Rhodium (–40.7 eV). Accordingly, the number density of truly free electrons can be estimated by integrating only those electrons whose energies exceed the barrier:

$$n(r) = \int_{V_{barrier}}^{\infty} c_1 \, \epsilon^{\frac{1}{2}} f(r) \, d\epsilon \qquad (2\text{-}7).$$

By applying this expression, the total number of electrons calculated from QEOS can be corrected by selecting only those that possess enough energy to escape the potential well, thereby providing a more accurate estimate of the electron number density $n(R_0)$ and ionization degree Z in partially ionized plasmas.

However, this ion-sphere model for partial ionization considers the potential barrier of an isolated molecule and is thus applicable primarily to gaseous phases. To distinguish the gaseous phase from condensed phases, the chemical bonding model used in the QEOS term F_b (More et al., 1988) in Eq. (2-2) was adapted by defining the intermolecular bonding energy as:

$$E_b = E_0 \, expb \left[1 - \left(\frac{\rho_s}{\rho}\right)^{\frac{1}{3}}\right] \quad (2\text{-}8).$$

The values of E_0 and b in Eq. (2-8) were calculated based on the QEOS input parameters for each material. Specifically, these parameters were determined using the atomic mass, atomic number, and bulk modulus (Takabe 1993).

If the ion temperature exceeds this bonding energy at a given material density, the material is regarded as being in the gaseous state, and the partial ionization ion-sphere model is applied accordingly. As a result of this procedure, materials that were initially treated as fully ionized plasmas in the standard QEOS model were corrected, as illustrated in Figure 2-2. The ionization degrees in the original QEOS output (Figure 2-2a) range from 4.2 to 10, which is significantly overestimated for the partially ionized plasma expected at electron temperatures of a few or a few tens of eV. Cells with densities above the reference values listed in Table 2-2 are classified as solid based on Eq. (2-8). For the remaining cells, corrections were applied using Eqns. (2-4), (2-5), and (2-7); however, in some cases, the electron potential V(r) in Eq. (2-5) failed to converge due to extremely low densities, resulting in the absence of corrected values. The corrected ionization

degrees (Figure 2-2 b) range from 0 to 3, which are more consistent with the actual electron temperatures in the simulation.

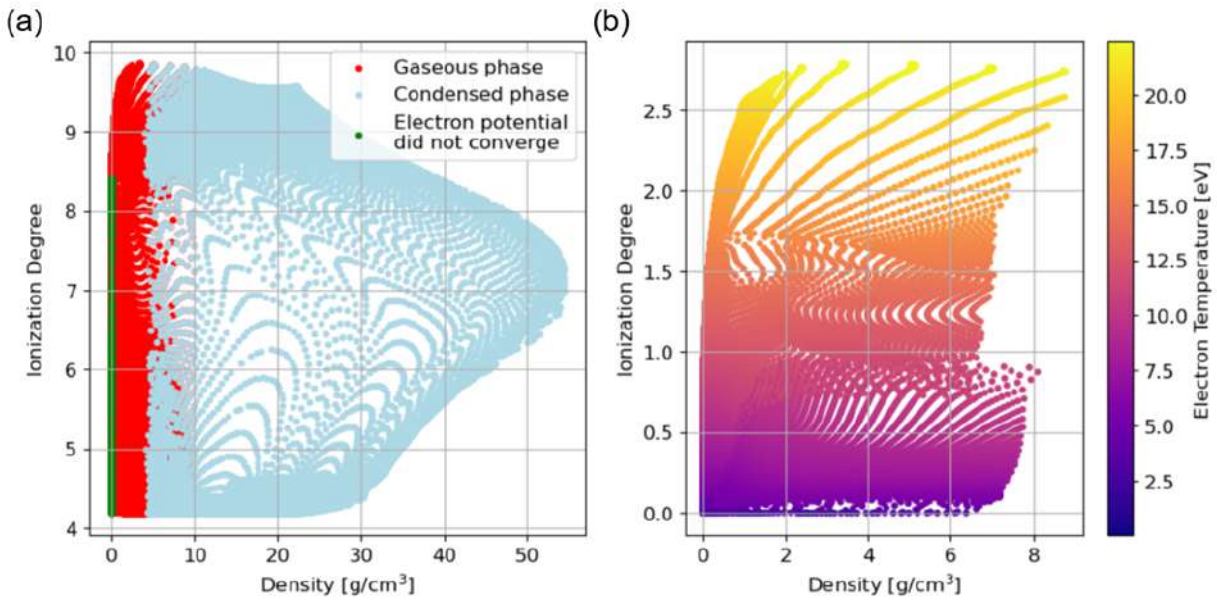

Figure 2-2. Ionization degree maps from QEOS at 1.6 ps in the simulation for the 44.0 km s^{-1} impact. All materials involved in the experiment, such as iron (projectile), rhodium (target), and nitrogen (ambient gas), are included. (a) Original QEOS output, where all electrons on the outer shell of the ion-sphere (i.e., valence and free electrons) are plotted. Cells for condensed phase material are shown in blue, cells whose electron potential did not converge during the correction procedure in green, and gaseous cells subject to correction in red. (b) Corrected QEOS output by applying a potential barrier-based cutoff to identify truly plasma electrons in the red-labeled plasma cells in (a). The color scale indicates electron temperature in electron volts (eV).

Using the ionization degree z obtained through the above procedure, along with the Faraday constant F, the atomic masses of the projectile and target materials (M_p, M_t), and the mass densities

of the projectile and target at each grid point (ρ_p, ρ_t), the charge generated at each grid point was estimated using the following equation:

$$Q = \sum_{i=p,t} F \frac{\rho_i}{M_i} z_{ion} \quad \text{(2-9).}$$

Additionally, to enable a meaningful comparison with the ion temperature measurements reported by Ratcliff et al.(1997), we compute the ion temperature as a charge-weighted average over all simulation cells. In the experiment, the electron multiplier collects ions using an external electric field and measures the time- and spatially-averaged energy of incoming ions. Therefore, to replicate the measurement conditions, the simulated ion temperature must be averaged over space using the local ion yield as the weighting factor. Moreover, considering that the experimental sampling is on the nanosecond scale, whereas the simulation resolves picosecond dynamics, a further temporal averaging using the total ion yield at that timestep as the weighting factor is also required. The charge-weighted average ion temperature at each time step t is given by:

$$E_{tot}(t) = \frac{\sum_j E_{ion,j}(t) \cdot Q_j(t)}{\sum_j Q_j(t)} \quad \text{(2-10),}$$

where $E_{ion,j}$ is the local ion temperature and Qj is the local ion number density in cell j. The final ion temperature value E_{avg} to be compared with experimental data is obtained by:

$$E_{avg} = \frac{\sum_t E_{tot}(t) \cdot Q_{tot}(t)}{\sum_t Q_{tot}(t)} \quad \text{(2-11),}$$

where Q_{tot} is the total ion yield at that timestep. The candidate ran the P4P code previously constructed (e.g. Nagatomo et al., 2006; 2015), and designed the analytical model and executed the calculations.

2.3 Comparison with Experimental Data

2.3.1 Non-Equilibrium Processes in Impact Ionization

Figures 2-3 and 2-4 present the time evolution of the density, charge, electron temperature, and ion temperature distributions for a hypervelocity impact between a 53 nm iron projectile and a rhodium target at 44.0 km s^{-1}. As the projectile penetrates the target, the local density reaches up to approximately 60 g cm^{-3}, and the propagation of a high-density region through the target due to the shock wave can be observed. In particular, Figure 2-3(b) shows a distinct high-density outflow emerging from the projectile–target interface at an angle of approximately 16.3°. In the density plot, this structure is characterized by densities in the range of 0.01–10 g cm^{-3}, which are more than an order of magnitude higher than those of the surrounding rarefied region, and it extends preferentially along a well-defined direction from the impact point. The snapshot corresponds to approximately half of the characteristic timescale, t_s (= $2r_p/v_{imp}$, where r_p is projectile radius in meters and V_{imp} is impact velocity in meters per second). Such a structure is consistent with impact jetting reported in previous hypervelocity impact studies (Walsh et al., 1953; Harlow et al., 1966; Ang 1990), where a high-speed, high-pressure, and high-temperature outflow is generated from the projectile–target interface during the early stage of the impact, from first contact to t_s. A similar directional structure is also observed in the ion temperature distribution shown in Figure 2-4(b). The jetting angle inferred from the ion temperature field is approximately 16°, in close agreement with the density-based estimate, indicating that both diagnostics capture the same mechanically driven jetting flow. In this region, the electron temperature reaches 20–30 eV, while the ion temperature exceeds 100 eV, demonstrating a pronounced thermal non-equilibrium during the early phase of impact ionization.

Additionally, the jetting region, despite its high temperature, does not contribute significantly to ion yield. This is attributed to the non-existence of the thermal nonequilibrium state in which the

electron temperature remains relatively low compared to the ion temperature. As shown in equations (2-5) and (2-7), the ionization degree is highly dependent on the electron temperature. However, the kinetic energy of the projectile is initially deposited into the ions, leading to preferential heating of the ions. The electron temperature rises gradually through thermal exchange with ions, resulting in a transient state where ion temperature is higher than electron temperature during the initial picoseconds after the impact. Previous studies have often identified jetting as one of the major contributors to impact flash generation (Jean and Rollins, 1970; Sugita and Schultz, 1999, 2003 ; Zhaoxia et al., 2020), but such observations typically involve ambient atmospheric interactions. In the present study, conducted under high vacuum conditions, it is clear that the jetting region contributes minimally to charge generation (Simpson et al., 2023).

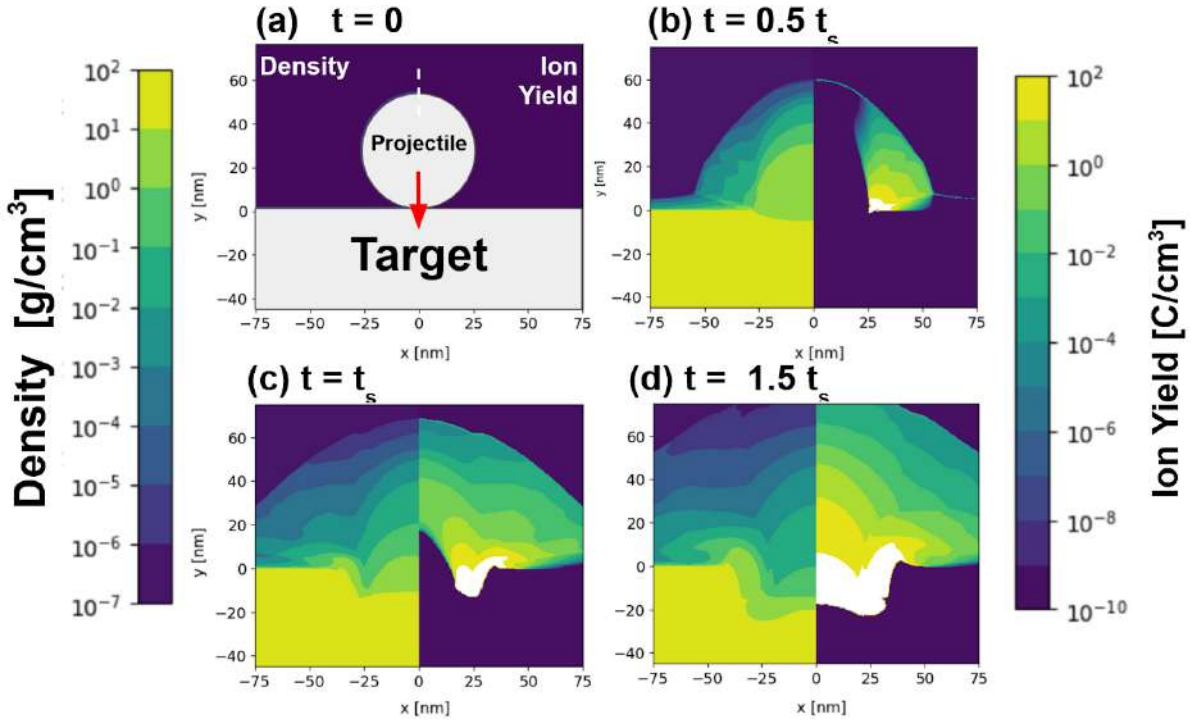

Figure 2-3. Temporal evolution of density and charge distributions during a hypervelocity impact between a 53 nm iron projectile and a rhodium target at 44.0 km s^{-1}. The left and right halves of each panel show the density and charge, respectively. (a) Initial setup at t = 0. (b–d) Snapshots at t =

0.5 t_s, t = t_s, and t = 1.5 t_s, where t_s is the characteristic impact timescale, defined as the ratio of the projectile diameter to the impact velocity ($t_s = 2r_p / v_{imp}$).

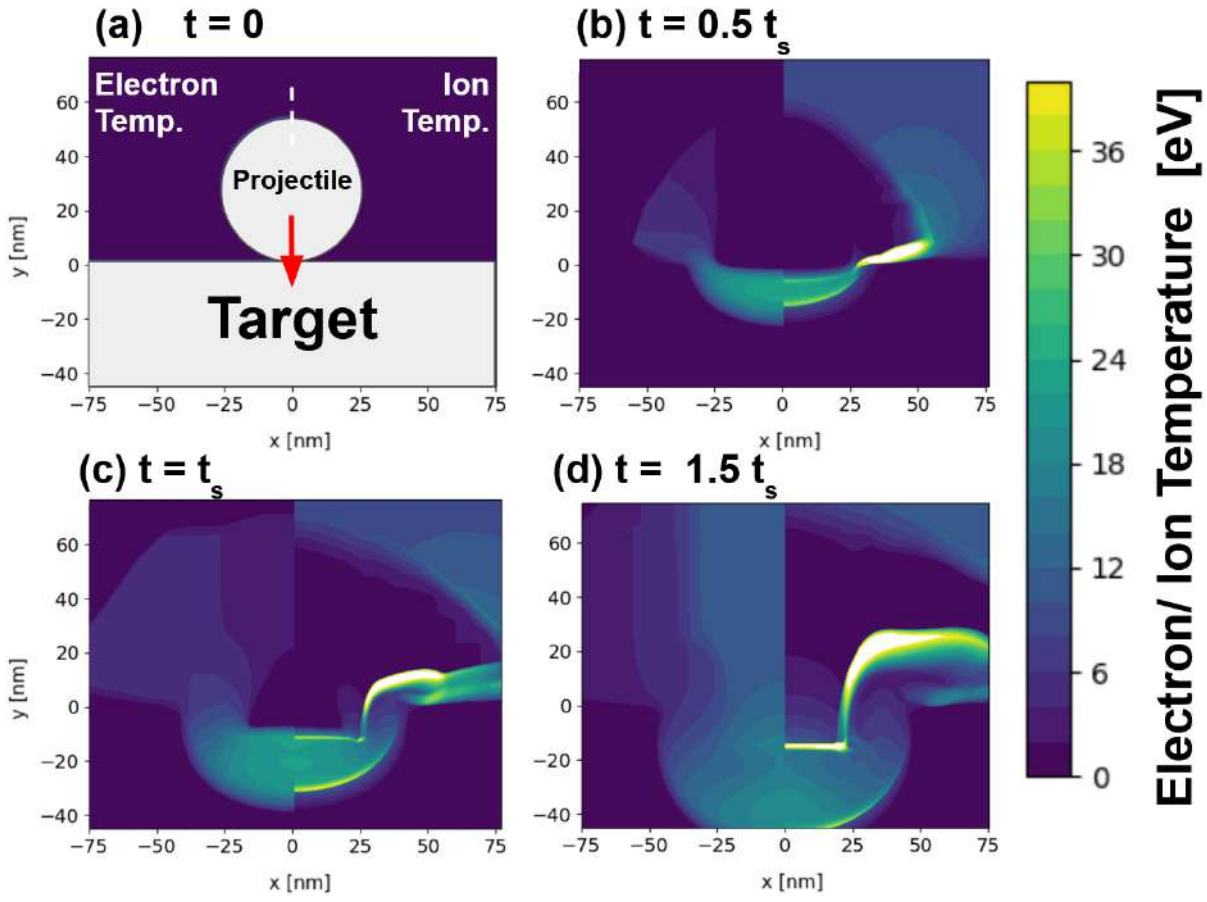

Figure 2-4. Temporal evolution of electron and ion temperature distributions during a hypervelocity impact between a 53 nm iron projectile and a rhodium target at 44.0 km s^{-1}. The left and right halves of each panel show the electron temperature and ion temperature, respectively. (a) Initial setup at t = 0. (b–d) Snapshots at t = 0.5 t_s, t = t_s, and t = 1.5 t_s, where t_s is the characteristic impact timescale, defined as the ratio of the projectile diameter to the impact velocity ($t_s = 2r_p / v_{imp}$).

Additionally, as shown in Figure 2-3(b–d), charge generation first occurs near the crater rim, characterized by moderate density and elevated electron temperature, and subsequently in the crater

floor. After this, the plasma would expand into vacuum as reported in many studies (Close et al., 2013; Goel, 2015; Tarantino, 2018, Hew et al., 2018,2021; Fletcher et al., 2015).

Based on the physical quantities at $t = t_s$ shown in Figure 2-3(c) and 2-4(c), the region near the crater rim has a lower density than the solid phase and exhibits ion temperatures exceeding the chemical bonding energy defined by equation (2-8), thereby being treated as gaseous. Moreover, the electron temperature surpasses 10 eV, allowing a significant fraction of electrons to overcome the potential barrier assumed in the QEOS model. Consequently, the ion-sphere model for partial ionization becomes valid in this region, and ionization degrees exceeding 1.0 are observed, corresponding to noticeable ion yield. In contrast, the crater floor exhibits extremely high density, up to 24 g cm^{-3}, and is therefore treated as a condensed phase. Although both ion and electron temperatures exceed 20 eV, the chemical bonding energy in this region is estimated to be as high as 313 eV, based on equation (2-8), making thermal excitation of electrons into free states difficult. As a result, the ionization degree in this region is evaluated to be nearly zero, and no charge generation is observed—entirely consistent with the theoretical framework of the QEOS model.

2.3.2. Impact of Non-Equilibrium on Impact-Induced Ionization

Figure 2-5 shows the simulation results at $t = 2.5\ t_s$ for two different assumptions: (a) a non-equilibrium case ($T_e \neq T_i$), and (b) a thermal equilibrium case ($T_e = T_i$), which is enforced by increasing the time constant for electron–ion temperature exchange by a factor of 1000 compared with the conventional setting. The time $t = 2.5\ t_s$ corresponds to the moment when the ion yield reaches its maximum in each condition. In the non-equilibrium case shown in Figure 2-5(a), the ion temperature locally increases at the shock front near the tip of the vapor plume. This feature reflects the conversion of kinetic energy into thermal energy through artificial viscosity. Because this high-temperature region is characterized by a low mass density, its contribution to the global energy balance of the system remains limited. In contrast, this localized thermal structure is spatially

homogenized in Figure 2-5(b). This behavior indicates that ion thermal energy is rapidly transferred to electrons and redistributed, demonstrating that thermal equilibrium is effectively established by the numerical modification.

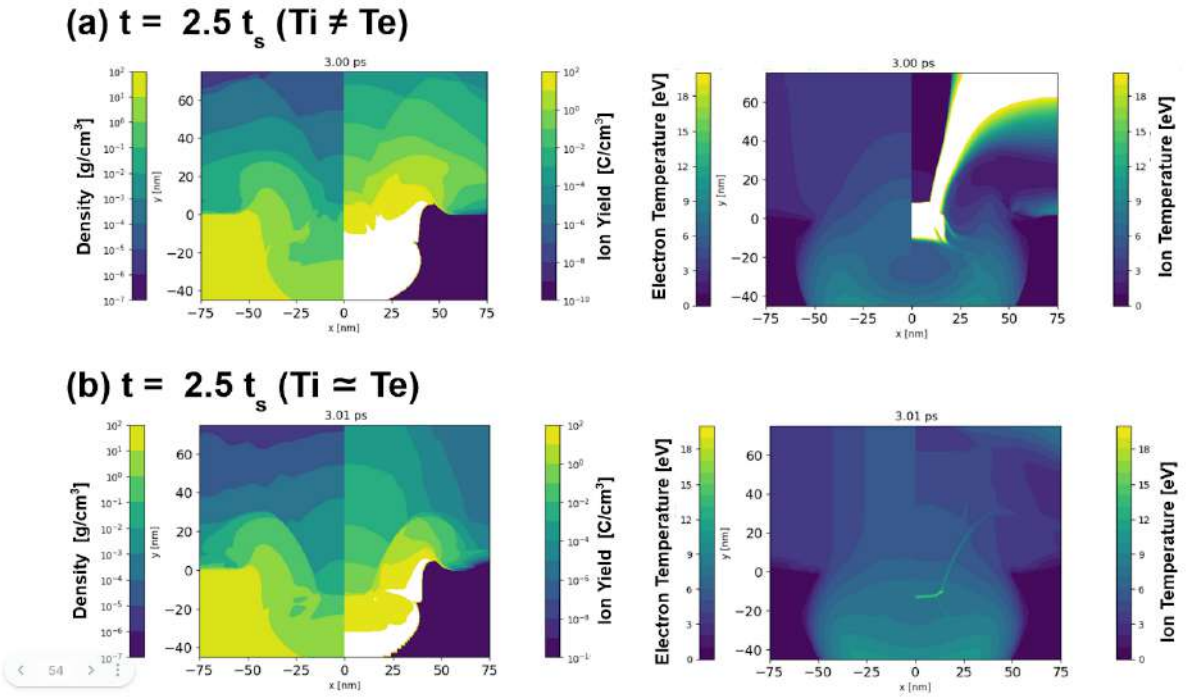

Figure 2-5. Spatial distributions of mass density and ion yield (left panels), and electron/ion temperature (right panels) at t = 2.5 t_s in a hypervelocity impact between a 53 nm iron projectile and a rhodium target at 44.0 km s^{-1} for (a) the non-equilibrium case ($T_i \neq T_e$) and (b) the thermal equilibrium case ($T_i \approx T_e$). Thermal equilibrium is enforced by increasing the time constant for electron–ion temperature exchange by a factor of 1000. The t_s is the characteristic impact timescale, defined as the ratio of the projectile diameter to the impact velocity ($t_s = 2r_p / v_{imp}$).

Despite the fact that the ion temperature, electron temperature, and mass density do not differ significantly between the two cases, the resulting ion yield shows a substantial discrepancy.

The total ion yield is 0.26 pC in the non-equilibrium case and only 0.042 pC in the equilibrium case. To investigate the origin of this difference, we focus on the location (x, y) = (0 nm, −20 nm) in Figures 2-5(a) and 2-5(b). At this position, the equilibrium case exhibits a higher electron temperature (7 eV compared to 5 eV) and a slightly higher density (0.8 g cm^{-3} compared to 0.7 g cm^{-3}), yet the generated charge density is significantly smaller (24 C cm^{-3} compared to 196 C cm^{-3}). This behavior is attributed to a pronounced reduction in the chemical potential appearing in the Fermi–Dirac distribution (Eq. 2-5), where the chemical potential in the equilibrium case is much lower than that in the non-equilibrium case (12 eV versus 36 eV). As a result, the Fermi–Dirac distribution shifts toward lower energies, leading to a substantial decrease in the population of electrons with energies exceeding the estimated surface barrier potential, $V_{barrier} \approx 50$ eV, as evaluated by Eq. (2-7).

In the P4P framework, the QEOS model is employed to self-consistently determine the electron number density, chemical potential, and electrostatic potential by solving the Poisson equation, the Fermi–Dirac distribution, and the charge neutrality condition using density and temperature as inputs (More et al., 1988). The resulting free energy is then used to construct the temperature evolution equation derived from the energy conservation law, in which temperature is treated as the primary unknown. Consequently, the chemical potential is not an independent variable but is constrained by the temperature that satisfies the time-dependent energy balance.

The electron energy evolution equation includes a source term dQ, which represents energy exchange and loss processes. Under thermal equilibrium conditions, the energy influx from ions into the electron system is enhanced, leading to an increase in the total electron energy. This trend is consistent with Figures 2-5(a) and 2-5(b), where regions of high charge generation inside the crater tend to exhibit higher ion temperatures in the equilibrium case. However, electrons transport energy far more efficiently than ions through thermal conduction, and additional energy loss occurs through

radiative processes. As a result, the effective energy budget governing the temperature evolution differs substantially between the equilibrium and non-equilibrium cases.

These differences in energy transport and redistribution reduce the chemical potential in the equilibrium case, thereby suppressing the high-energy tail of the electron distribution and ultimately leading to a lower ion yield. This result demonstrates that non-equilibrium processes between ions and electrons play an essential role in accurately reproducing impact-induced ionization in P4P simulations.

2.3.3 Ion Yields

By integrating the simulated two-dimensional charge distributions in cylindrical coordinates, we analytically estimated the total amount of charge generated in three dimensions at each time step. Figure 2-6 shows the temporal evolution of the ion yield for four different impact velocities. We can see that many of the ion yield curves have two peaks. The first and second peaks exist around 1 and 3 times the characteristic timescale t_s, then gradually decay as the electron energy dissipates. Figure 2-7 shows the temporal evolution of the ion yield separately for the projectile and the target during a 44.0 km s^{-1} impact event. According to this graph, we can estimate that the first peak is attributed to the combined peak of target and projectile ion yield, while the second peak is attributed solely to the peak of projectile ion yield. By Figure 2-4, we can see ions of the projectile are generated from the rear side of the projectile, and one of the targets is generated from the edge of the crater. Because of these facts, we may be able to assume target ions are generated after the rarefaction wave from the edge of the crater releases the shocked and compressed target material created by the shock wave, and projectile ions are generated after the shock wave reaches the rear side of the projectile. The rarefaction wave created by the reflection of the shock wave propagates through the projectile. The gap between the two peaks may represent this different process.

Interestingly, the temporal overlap between the two peaks becomes more pronounced at higher impact velocities. For example, at 44.0 km s^{-1}, the two peaks merge into a single sharp structure, likely due to the rapid propagation of the shock and rarefaction waves through both the target and the projectile. In contrast, at lower velocities, the delay between the two processes becomes more distinct, resulting in a well-separated double-peak structure. This behavior is consistent with the fact that the shock wave speed increases nearly linearly with particle velocity, preserving the timing of the first peak across different impact velocities, while the rarefaction wave speed has a different dependency (Wen and Chen, 2020), causing the second peak to shift forward with increasing velocity. This trend further supports the interpretation that the mechanical process of the ion formation.

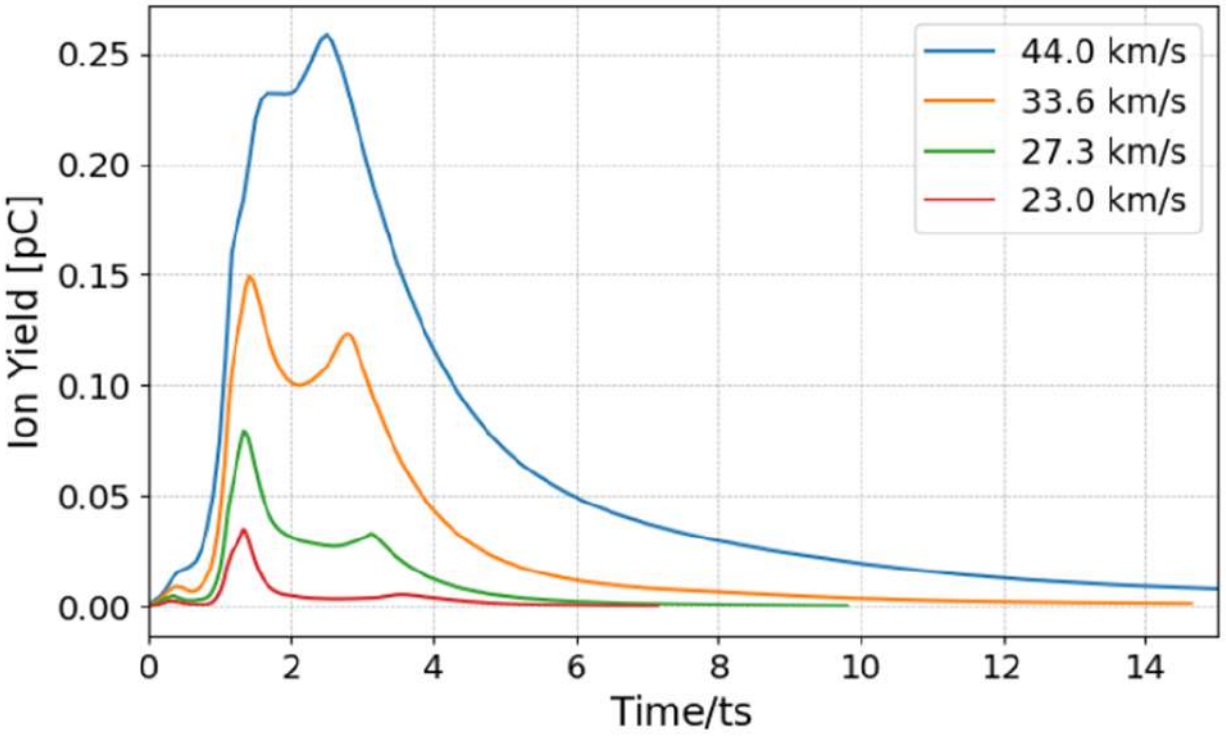

Figure 2-6. Temporal evolution of ion yield [pC] for four impact velocities: 23.0 km s^{-1}, 27.3 km s^{-1}, 33.6 km s^{-1}, and 44.0 km s^{-1}. Each curve represents the integrated ion yield over the simulation domain as a function of time. Horizontal axes are normalized by the characteristic timescale ($t_s = 2r_p/v_{imp}$).

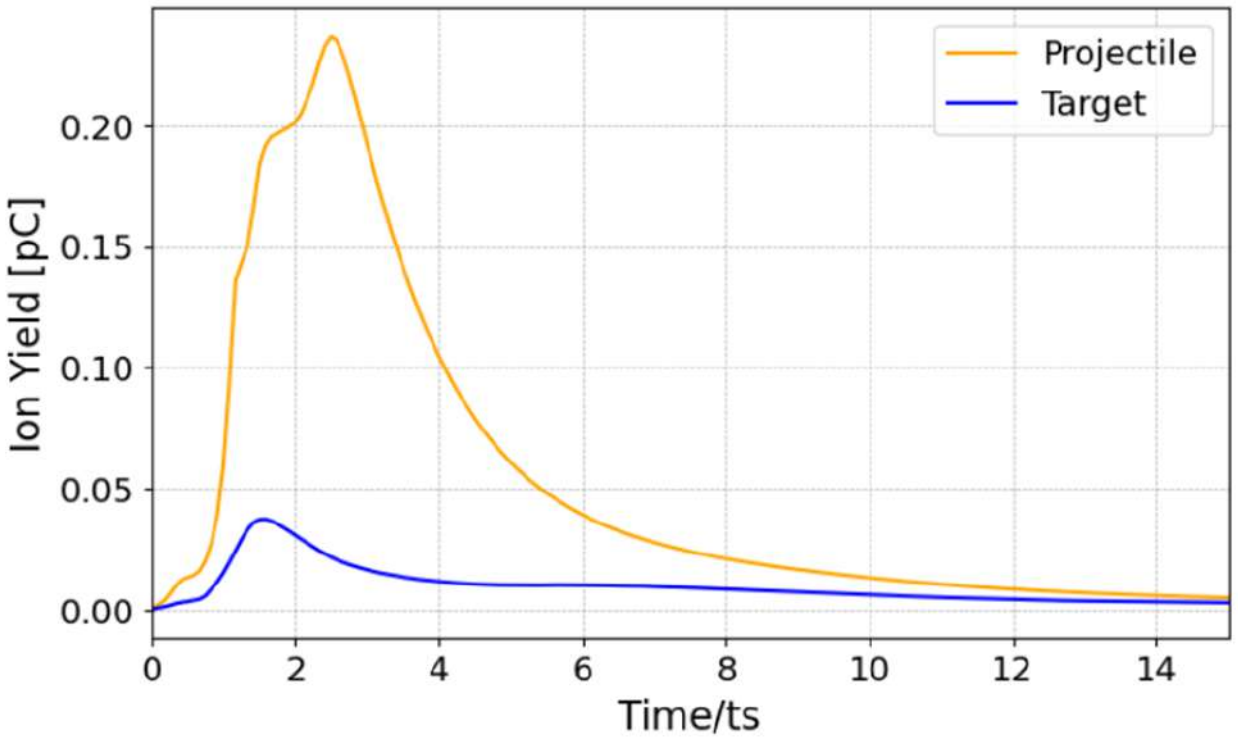

Figure 2-7. Temporal evolution of ion yield originating from the projectile (Fe, orange) and the target (Rh, blue) in a 44.0 km s^{-1} impact event. Horizontal axes are normalized by the characteristic timescale ($t_s = 2r_p/v_{imp}$).

In this simulation, we compute the spatially integrated ion charge present within the computational domain at each time step. In the experiments, ions are extracted upward by an external electrostatic field and collected by an acceleration grid. In similar plasma collection experiments, Knabe and Krüger (1982) noted that no Debye-shielding effect is expected with particles up to 70 km s^{-1} and about one micrometer diameter or less. Referring to Hew et al.(2021), we can also assume that almost all of the plasma generated in hypervelocity impact will expand beyond the Debye length and will be collected by the electric fields. Under this assumption, we use the peak ion yield values from Figure 2-6 as the maximum possible charge present during the impact

event as Song et al. (2016) did. While this assumption overlooks recombination, it provides a first-order estimate that is consistent with the experimental configuration.

Based on the above hypothesis, we compared the ion yield per unit projectile mass (Q/m) from the simulation with the experimental values for each velocity, as shown in Figure 2-8. The simulation results follow the relationship:

$$Q/m = 4.9 \times 10^{-3}\ v^{4.80} \qquad (2\text{-}12).$$

Assuming a power-law form with an exponent $\alpha = 1$, the velocity exponent β was found to be 4.80, and the coefficient c was 4.9×10^{-3} (for Q measured in Coulombs, m in kg and v in km s^{-1}). In comparison, Ratcliff et al. (1997) and Burchell et al. (1999) reported $\beta = 4.74$ and $c = 8.5 \times 10^{-3}$, $\beta = 4.82$ and $c = 4.4 \times 10^{-3}$ for iron projectiles to rhodium targets, respectively. The similarity in trends is remarkable, especially the velocity dependence, where the β value differs by only about 1% and 0.5 % from Ratcliff et al. (1997) and Burchell et al,(1999), respectively. Although the coefficient c in the simulation is approximately 42% of Ratcliff et al., the difference from the value of Burchell et al.[35] is only 10%, and it remains consistent across all velocities. The logarithmic residuals shown in the inset of Figure 2-8 exhibit an approximately flat trend with respect to impact velocity, indicating that the velocity dependence of the simulation results is in good agreement with the experimental data and that the remaining discrepancy primarily manifests as a systematic offset in the coefficient c rather than a velocity-dependent deviation.

To assess the numerical uncertainty associated with the simulation, a grid convergence analysis was performed by comparing the standard resolution case ($\Delta x = 0.2$ nm) with a coarser grid ($\Delta x = 2.5$ nm). The resulting uncertainty is larger at lower impact velocities and decreases toward higher velocities, indicating improved numerical convergence in the high-velocity regime. Importantly, the magnitude of the residual offset can be related to the coefficient c, and the difference in the coefficient c between Ratcliff et al. and Burchell et al. might be attributed to

differences in experimental geometry (Burchell, personal communication, 2025), suggesting that the reproducibility of this coefficient is not fundamentally significant.

The consistency of the β value with experimental data is particularly remarkable, considering that previous numerical studies have struggled to match ion yields measured in experiments. For example, Song et al. reported 3D numerical simulations of hypervelocity impacts. Although a direct comparison is not possible due to different projectile–target combinations and the higher complexity of their three-dimensional calculations, fitting their reported results to Eq. (2-1) indicates that the predicted ion yields correspond to approximately 70% of the empirical formula by Ratcliff et al. at 15 km s^{-1}. It is worth noting that in Song et al., the hydrodynamic response was governed by a solid-state EOS, while Thomas–Fermi theory was used only in a post-processing ionization model under a single-temperature assumption. Similarly, Zhao et al.[53] observed that theoretical charge quantities exceeded experimental measurements, especially above 10 km s^{-1}. In Zhao et al., ionization was estimated using the Saha equation applied to temperatures obtained from the EOS, implicitly assuming local thermodynamic equilibrium.

Within the high-velocity regime considered in the present study, the present study achieves close agreement with experimental values. This success likely stems from two key factors: first, we deliberately focused on impact velocities above 20 km s^{-1}, where bulk ionization dominates, while avoiding the surface-ionization-dominated regime below 15 km s^{-1} (as discussed by Dalmann et al.; Mocker et al.); and second, we correctly implemented the QEOS model, which accurately describes high-temperature plasma states.

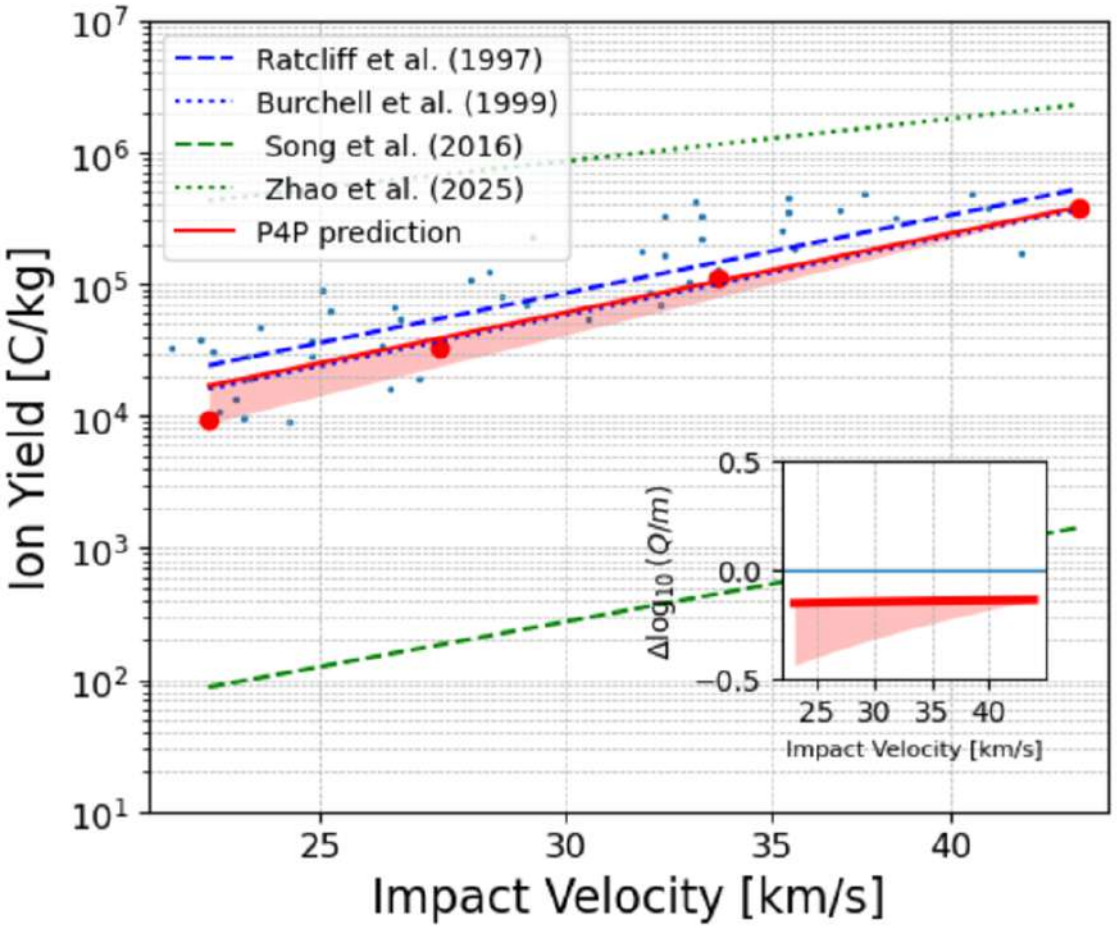

Figure 2-8. Comparison of ion yield per unit projectile mass (Q/m) as a function of impact velocity. The two blue lines represent previous experimental scaling: Ratcliff et al. (1997) (dashed) and Burchell et al. (1999) (dotted). The blue scatter points indicate the original experimental measurements reported by Ratcliff et al. (1997). The two green lines represent previous numerical predictions: Song et al. (2016) (dashed) and Zhao et al. (2025) (dotted). The red solid line shows the present P4P simulation prediction, with red dots indicating individual simulation results from this work. The red solid line shows the present P4P simulation prediction, with red dots indicating individual simulation results from this work. The red shaded region represents the numerical uncertainty associated with spatial resolution, estimated from the difference between simulations performed with grid spacings of $\Delta x = 0.2$ nm (standard resolution) and $\Delta x = 2.5$ nm (coarser resolution). The inset shows the logarithmic residuals, $\Delta\log_{10}(Q/m) = \log_{10}[(Q/m)\_model / (Q/m)\_exp]$, between the P4P prediction and the experimental data of Ratcliff et al. (1997) as a function of impact velocity.

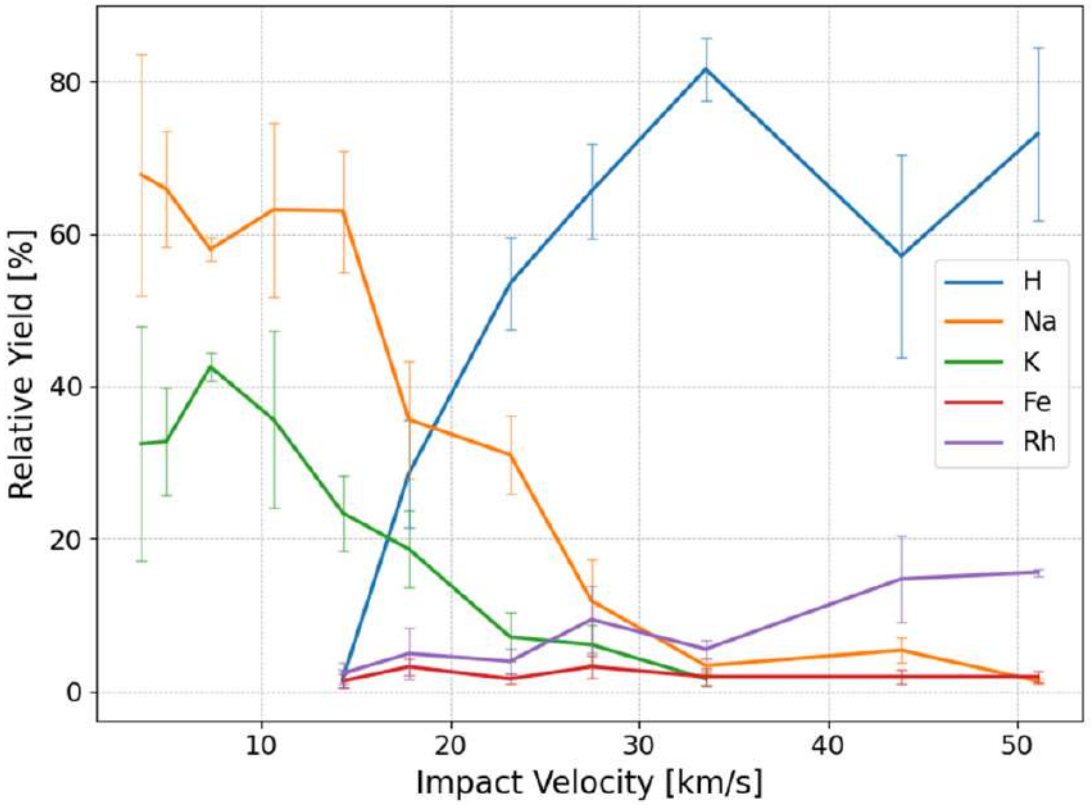

Figure 2-9. Relative yields of atomic species observed in impact plasma as a function of impact velocity, based on experimental results adopted by Ratcliff et al. (1997).

One thing to be noted is that the simulation does not account for hydrogen atoms, which significantly contribute to the experimental signal. As shown in Figure 2-9, for impact velocities exceeding 20 km s^{-1}, most of the ions detected by the electron multiplier are hydrogen, which originates from contamination on the target (Kissel and Krueger, 1984; Postberg et al., 2009; Klenner et al., 2019). As shown in Figure 2-9, for impact velocities exceeding 20 km s^{-1}, hydrogen ions account for a substantial fraction of the ions detected by the electron multiplier. In contrast, the P4P simulations intentionally focus on ionization of the primary metallic constituents and do not include hydrogen dissolved in the target material.

This difference raises the question of whether a direct comparison between the simulated and experimentally inferred velocity-scaling exponent β is physically meaningful, given that a

dominant ion species in the experimental signal is absent from the model. A key point, however, is that different diagnostic components in the experimental setup probe different ion populations. While the electron multiplier detects the relative abundance of ion species after post-impact expansion and acceleration, the total ion yield is measured by the acceleration grid located approximately 3 mm above the target surface. As a result, the species composition detected by the electron multiplier does not necessarily reflect the relative ionization occurring at the impact site.

To illustrate this effect, Figures 2-10(a) and (b) show the velocity distributions of rhodium target ions and iron projectile ions at the time of maximum charge generation, assuming Gaussian distributions characterized by their mean velocities and standard deviations. Using these distributions as initial conditions, ion trajectories were calculated with SIMION in a geometry reproducing the target disk and acceleration grid of the experimental setup by Ratcliff et al. Hydrogen ions, being released from the rhodium target, were assigned the same initial velocity distributions as target-derived ions. As shown in Figure 2-10(c), heavier ions experience weaker vertical acceleration in the electric field, making their horizontal velocity components more influential in determining their post-impact dispersion. Consequently, the experimental configuration, where the electron multiplier is positioned along the target normal, strongly favors the detection of hydrogen ions.

Because key parameters such as the detector distance and the aperture of the ion-focusing optics are not reported, a fully quantitative correction of the measured species yields is not possible. Therefore, the relative yields of atomic species reported in the experiments should not be interpreted as direct measures of the intrinsic ionization yields at the impact site without accounting for velocity-space filtering and post-impact drift processes.

Even though rhodium atoms are heavier than iron atoms, Figures 2-10(a) and (b) show that the horizontal initial velocity dispersion of iron ions is larger than that of rhodium ions. As a result,

the trajectories of iron ions are more widely spread than those of rhodium ions. This implies that the present experimental configuration favors the detection of rhodium ions over iron ions.

The simulation results shown in Figure 2-7 indicate that ion generation from the projectile dominates the total ion yield, suggesting that most of the ionization occurs within the projectile material during and shortly after the impact. In contrast, as shown in Figure 2-9, the dominant ion species detected in the experiment is rhodium, originating from the target. These apparent inconsistencies can be reasonably attributed to the geometry and selectivity of the experimental detection system. Therefore, although hydrogen is not included in the present simulations and discrepancies exist between the experimentally detected and simulated relative ion yields, the model still captures the dominant bulk ionization processes of metallic species and remains physically meaningful.

What we can reliably compare is the total ion yield estimated by the simulation and measured in the experiment, and we can qualitatively attribute the lower coefficient c in the simulation to the absence of hydrogen. That should not be interpreted as a fundamental inconsistency, but rather as a reflection of differences in detection conditions and simulation assumptions. Thus, the strong agreement in the velocity dependence β serves as a more reliable indicator of the simulation's validity. This supports the conclusion that, despite the difference in absolute magnitude, the simulation successfully captures the fundamental physics of hypervelocity impact ionization.

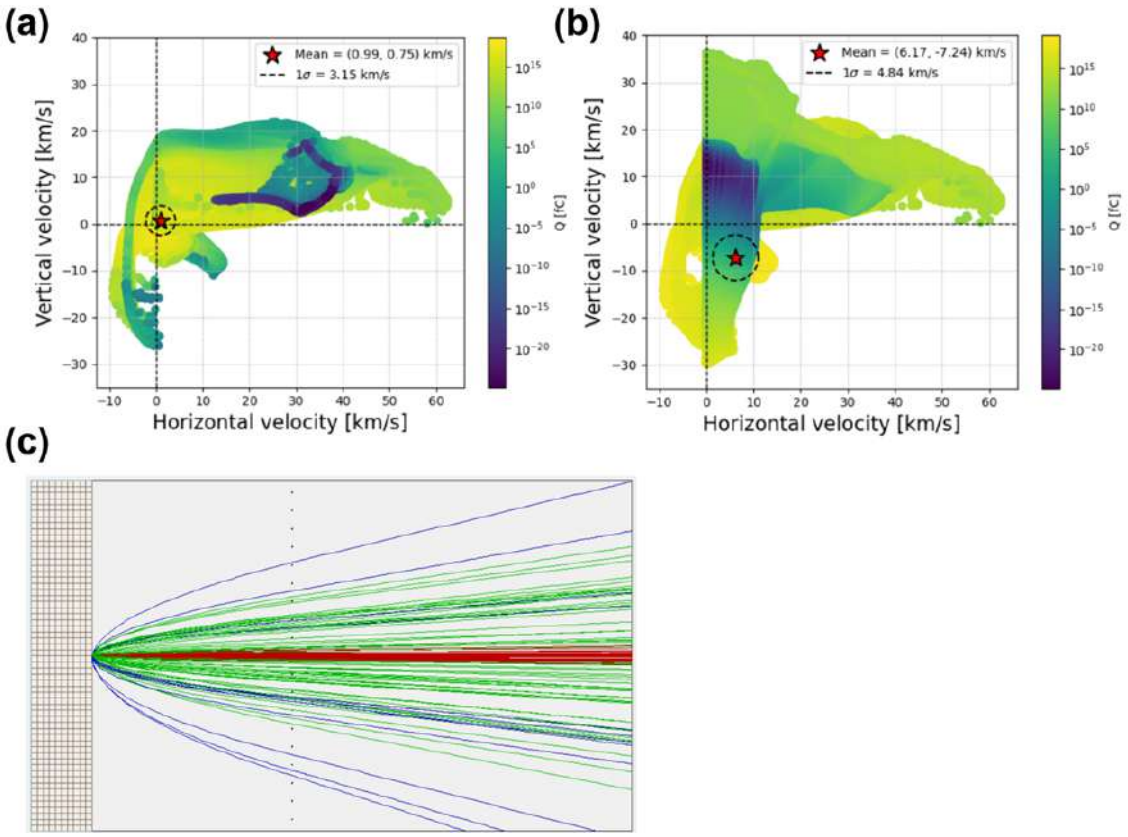

Figure 2-10. Species-dependent velocity distributions and ion trajectories illustrating detection bias in the experimental setup. Charge-weighted velocity distribution of (a) rhodium ions and (b) iron ions at the time of maximum charge generation, assuming a Gaussian distribution characterized by its mean velocity and standard deviation. (c) Ion trajectories calculated with SIMION using the mean velocities and standard deviations obtained in (a) and (b) as initial conditions, where red, blue, and green trajectories correspond to hydrogen, iron, and rhodium ions, respectively.

2.3.4 Ion Temperature

Figure 2-11 shows the temporal evolution of the average ion temperature for different impact velocities for both projectile and target. The ion temperature peaks sharply within the first 0.1 ps after impact and then decays rapidly. The sharp peaks in Figure 2-11 correspond to the jetting region formed immediately after impact, where ions can exceed 100 eV, as shown in Figure 2-4. However, according to Figures 2-6, the total ion charge in this region is relatively low, implying that these high-energy ions contribute little to the overall ion yield. The majority of ions are expected to originate from the region around the peak of the ion yield curve shown in Figure 2-6. Accordingly, we compute the time-averaged ion temperature as described in Equation (2-11), integrating from 0 ps up to the time corresponding to the peak of the ion yield curve (see Figure 2-12).

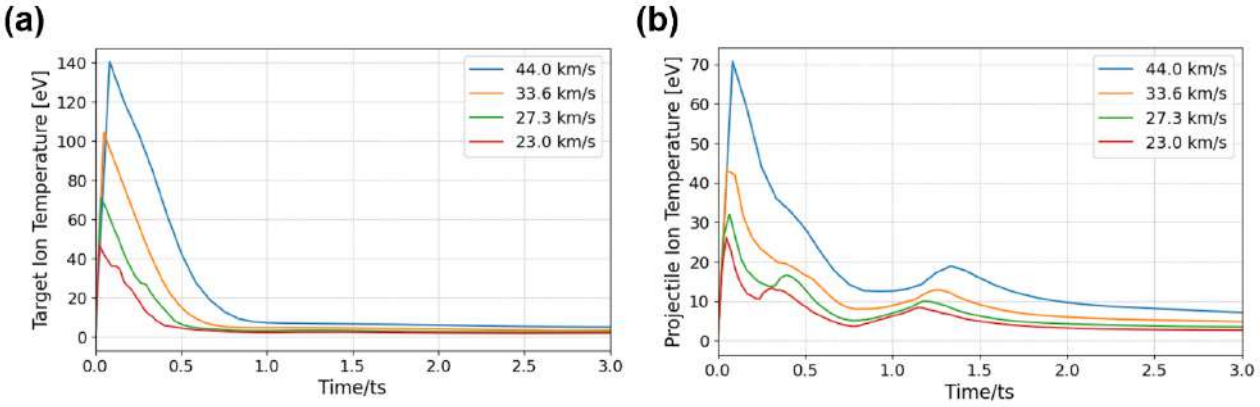

Figure 2-11. Temporal evolution of spatial average ion temperature obtained from equation (2-10), shown separately for ions originating from the target (a) and from the projectile (b), at various impact velocities. Horizontal axes are normalized by the characteristic timescale ($t_s = 2r_p/v_{imp}$). For both target and projectile ions, higher impact velocities result in higher peak energies.

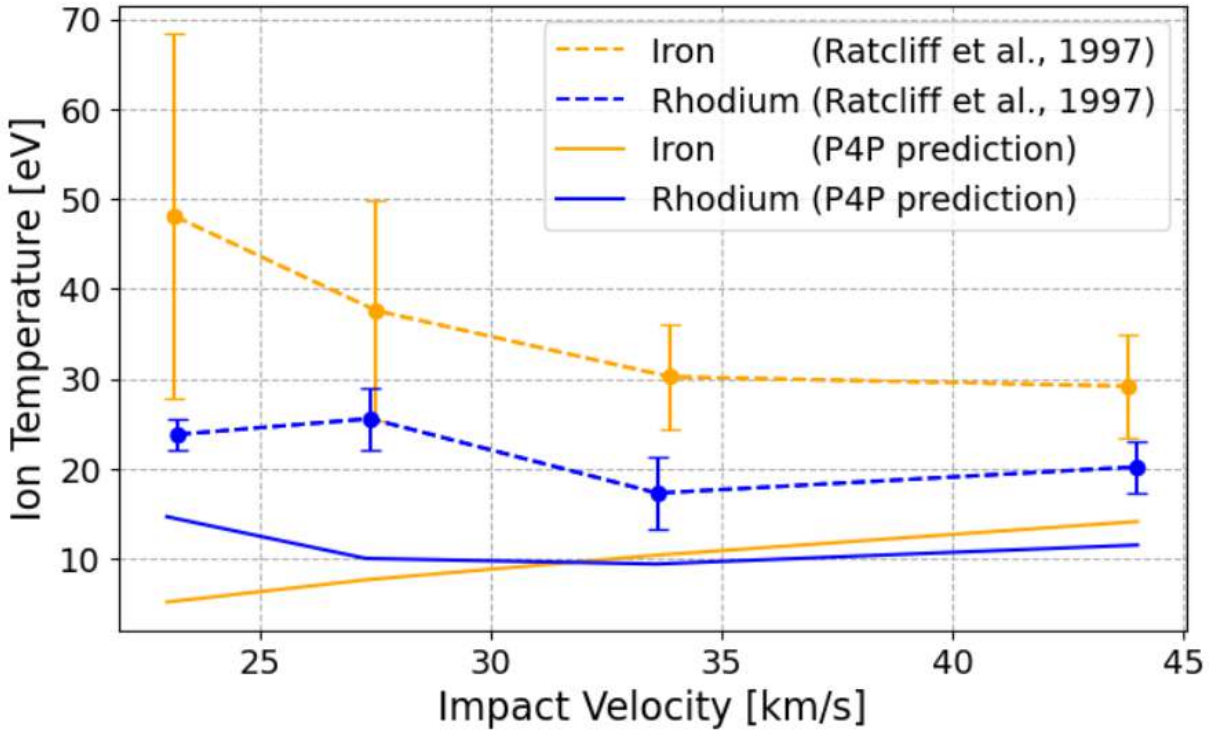

Figure 2-12. Comparison of time-averaged ion temperature between the P4P simulation and the experiment by Ratcliff et al. (1997) as a function of impact velocity, shown separately for ions originating from the projectile and the target. In the simulation, the ion temperature was computed as a spatial average initially weighted by the local ion charge density, and subsequently averaged over time using the total ion yield at each time step, ranging from 0 ps to the time that corresponds to the peak of the ion yield curve, as described in equation (2-11).

Although the simulation underestimates the absolute ion energies compared to the experimental results (Fig 2-12), there is no strong velocity-dependent trend similar to the experiment. This discrepancy is likely attributable to hydrogen contamination and/or differences in experimental geometry. In the experiments, ion energies are inferred from mass spectra measured using an electron multiplier. As a result, differences between the simulated and experimentally inferred ion energies, as discussed in the previous section, are not negligible. In particular, the electron multiplier is expected to preferentially detect lighter ions and ions with a substantial

velocity component normal to the target surface, rather than providing a fully representative distribution of all ions generated by the impact.

2.4 Summary

In this chapter, we developed a radiation-hydrodynamics framework called P4P, which explicitly treats electrons and ions as having separate temperatures. By combining thermal conduction, radiative transport, and electron–ion energy exchange, and by applying a potential-barrier-based correction to the QEOS equation of state, we created a model that can quantitatively capture the highly non-equilibrium plasma conditions that arise immediately after an impact. From the ionization and charge calculations, several key findings emerged.

First, regarding velocity dependence, impacts between iron and rhodium showed an ion yield that scaled as $Q/m \propto v^{4.80}$. This result closely matches experimental data (Ratcliff et al.; Burchell et al.), which reported $\beta \approx 4.74$–4.82. Small deviations in the coefficient are mainly attributed to differences in experimental geometry, hydrogen contamination, and the lack of external electric fields or hydrogen in the present model. Despite these differences, the main physical processes are consistently reproduced. Next, for the spatial distribution and generation mechanism, we found that charge generation occurs primarily in the medium-density region around the crater rim, where the electron temperature is high. In contrast, at the crater floor, where the material remains condensed, the binding energy is large and the ionization degree is almost zero ($Z \approx 0$). Although the initial jetting region shows a high ion temperature, its lower electron temperature makes only a small contribution to the total ion yield. The temporal evolution of ion yield shows a distinct double-peak structure, corresponding to the passage of the shock and rarefaction waves. As the impact velocity increases, the interval between the two peaks becomes shorter, and they gradually merge into a single broad peak.

For ion temperature, while the absolute energies are somewhat lower than experimental measurements, the weak dependence on impact velocity is well reproduced. The discrepancy is mainly due to experimental detection biases caused by hydrogen-dominated ion collection and the oblique impact geometry.

Overall, these results demonstrate that the P4P model provides a reliable description of the key features of non-equilibrium ionization in hypervelocity impacts, specifically, the spatial origin of charge generation, its characteristic timescales, and its velocity scaling behavior. In the next chapter, we will use this validated P4P framework to systematically investigate the physical equivalence between laser irradiation and impact ionization. By referring to representative experiments such as Klenner et al. (2019), we aim to quantitatively link laser intensity with impact velocity and identify the conditions under which their ion yields, mass spectra, and energy distributions coincide. This analysis will not only guide the design of laser-based simulated impact experiments but also lay the foundation for applying photoionization techniques, which will be explored in the following chapter.

Chapter 3 Analysis of the Equivalence Between Laser Irradiation and Hypervelocity Impacts

3.1 Background and Motivation for Comparing Laser Ablation and Hypervelocity Impacts

In Chapter 1, we identified the uncertain equivalence between laser ablation and impact ionization as one of the key issues limiting the interpretation of mass spectra obtained from impact experiments. Although the similarity between the two processes has been recognized since the 1970s and has been explored in the calibration of dust analyzers aboard cometary missions such as VEGA and GIOTTO (e. g., Kissel & Krueger, 1987), the physical correspondence between laser fluence and impact velocity remains largely empirical. In particular, while Klenner et al. (2019) compared the MS spectra of laser ablation and hypervelocity impacts and reported a qualitative similarity, the comparison was specific to their experimental setup and could not be generalized across different systems. Therefore, to establish a quantitative and physically grounded framework linking these two ionization processes, this chapter employs the P4P radiation-hydrodynamics code, which was calibrated in Chapter 2, to simulate both phenomena under controlled and comparable conditions.

Yet, until the laser ablation process is directly modelled, it is crucial to understand why direct reproduction of hypervelocity impacts in laboratory experiments is inherently limited, and how laser-driven experiments can serve as meaningful analogs under thermodynamically equivalent states. The following Section 3.1.1 describes the experimental limitations of reproducing hypervelocity impacts, highlighting the need for a numerical approach that bridges laser ablation and impact ionization.

3.1.1 Experimental Limitations in Directly Reproducing Hypervelocity Impacts

Hypervelocity impacts of micrometeoroids reach velocities of several tens of kilometers per second, and they are extremely difficult to reproduce directly in ground-based experiments. In a two-stage light gas gun, the achievable velocity is generally limited up to ~7 km s^{-1}, and it is not always possible to reproduce the regime in which material vaporization or plasma formation becomes dominant (i.e., >10 km s^{-1}). On the other hand, while electromagnetic accelerators are theoretically capable of achieving impact velocities on the order of several tens of kilometers per second, this requires that the accelerated particles be reduced to nanometer-scale sizes (e.g., Ratcliff et al., 1997; Postberg et al., 2014), where the governing physical processes are no longer representative of micron-sized or larger micrometeoroid impacts. Under such conditions, the effects of particle size, thermal diffusion, and radiative transport become significant, making it difficult to directly scale the observed phenomena to macroscopic meteoroid impacts. Therefore, to simulate the transient high-temperature and high-pressure states generated by impacts at tens of kilometers per second, it is necessary to employ an alternative approach that can reproduce thermodynamically equivalent conditions — namely, laser irradiation.

3.1.2 Analogy of High-Temperature and High-Pressure Conditions Induced by Laser Irradiation

Laser irradiation can produce plasmas characterized by extremely high temperature, pressure, and ionization degree by depositing intense energy onto a material surface within an extremely short timescale. Notably, the characteristic timescale of a hypervelocity impact by micron-sized particles, typically several tens of kilometers per second, is on the order of nanoseconds. Consequently, nanosecond-pulse laser experiments can reproduce temperature, pressure, and entropy conditions comparable to those of impact plasmas. However, laser irradiation and hypervelocity impacts

inherently involve fundamentally different modes of energy deposition, and their thermodynamic pathways significantly differ from each other (Hamann et al., 2016).

As illustrated in Figure 3-1, the pressure–volume relationship of a hypothetical silicate material under shock compression clarifies this difference. In an impact event, the material is compressed from point A (ambient conditions) to point B along the Hugoniot curve, and subsequently released to point B' during expansion. In this process, melting and initial vaporization are induced. When the compression reaches a higher shock pressure (point C), the material can reach a completely vaporized state (point C') (Melosh, 1989).

In contrast, under laser irradiation, the material can reach the B' phase (melting or partial vaporization) directly, without undergoing the shock-compression process, depending on the irradiation parameters (green dashed arrow in the figure).

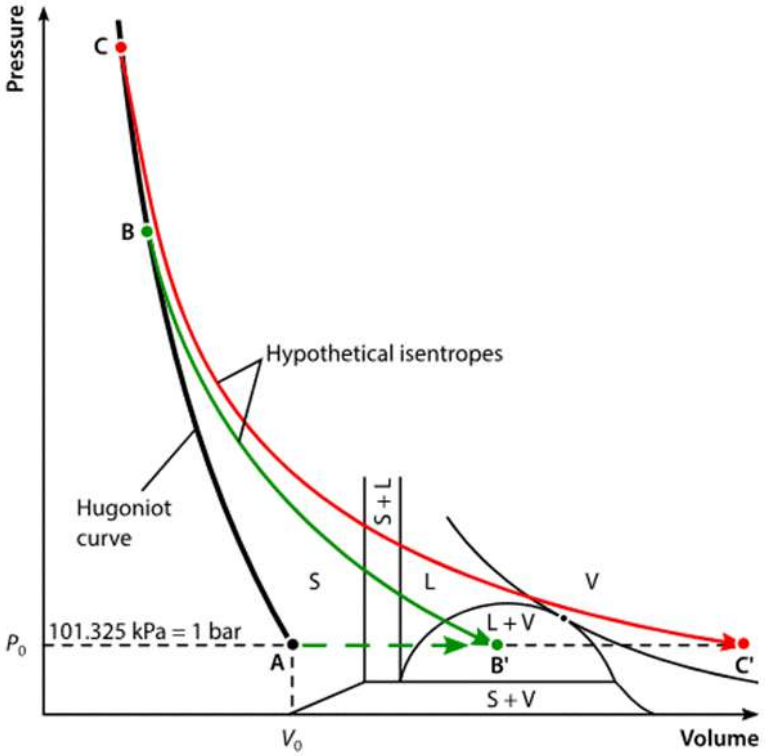

Figure 3-1. Pressure–volume relationship of a hypothetical silicate material subjected to shock compression (Adopted from Hamann et al., 2016).

This difference originates from the mechanism of energy deposition. Specifically in hypervelocity impacts, momentum-driven compression occurs through the transfer of momentum, whereas pressure-driven heating based on photon absorption is dominant in laser irradiation. Furthermore, in laser irradiation, the standoff distance of the absorption layer (cutoff depth) is limited, and part of the energy diffuses laterally according to the Gaussian profile. Thus, even if the shock pressure is equal to the ablation pressure, it is not self-evident that both conditions will lead to the same temperature.

Even when both processes reach an identical final thermodynamic state (e.g., partial vaporization), their respective pathways differ. In particular, laser irradiation does not reach the shock Hugoniot condition, which represents a fundamental distinction between the two phenomena (Hamann et al., 2016). When we employ laser irradiation as an analog for hypervelocity impacts, it becomes essential to clarify which physical quantities, such as pressure, temperature, entropy, or degree of ionization, should form the basis for defining phase equivalence. Various comparative approaches have been proposed in previous studies. For example, Ahrens et al. (2003) conducted comparisons based on equivalence in input kinetic energy, while Pirri (1977) and Aubert et al. (2019) focused on crater formation. Kissel & Krüger (1987) investigated the correspondence between the two phenomena through comparisons of total charge yield. Moreover, the studies by Arad et al. (1996), Kadono et al. (2002), and Hamann et al. (2016) all demonstrated that the thermodynamic states achieved under laser irradiation could be quantitatively similar to those generated by hypervelocity impacts. These previous studies established a foundation for treating laser irradiation as a thermodynamic analog to impact processes.

Building upon this framework, this study focuses particularly on the reproducibility of ionization processes and mass spectra. Specifically, we aim to quantitatively examine the extent to which the energy distribution and charge states of ions ejected by hypervelocity impacts can be

reproduced by laser irradiation. This type of comparison has been pursued by Ohno et al. (2004), Mocker et al. (2012), Klenner et al. (2019), and Sanderink et al. (2023). With their findings, this study analytically evaluates the phase equivalence between laser irradiation and hypervelocity impacts, by using numerical simulations with the P4P code.

3.2 Numerical Methods and Simulation Conditions

3.2.1 Overview of the LILBID Experiment

As an analogue experiment for impact ionization mass spectrometry (IIMS) under hypervelocity impact conditions, the Laser Induced Liquid Beam Ion Desorption (LILBID) technique has been developed (e. g. Klenner et al., 2019; 2022; Khawaja et al., 2020; Sanderink et al., 2023).

This method experimentally reproduces the ice particle impact spectra observed by spaceborne mass spectrometers, such as the Cosmic Dust Analyzer (CDA) onboard the Cassini spacecraft and the Surface Dust Analyzer (SUDA) currently flying in space on the Europa Clipper, under laboratory conditions.

In the LILBID method, a liquid water beam with a radius of approximately 7–12 µm—optionally containing organic compounds or salts—is injected into a high-vacuum chamber (5×10^{-5} mbar). A pulsed infrared laser (wavelength = 2840 nm, pulse width = 7 ns, repetition rate = 20 Hz, maximum energy = 4 mJ) is focused onto the beam, instantaneously heating and explosively dispersing the water jet. The resulting cations and anions are detected using a reflectron-type time-of-flight mass spectrometer (ToF-MS).

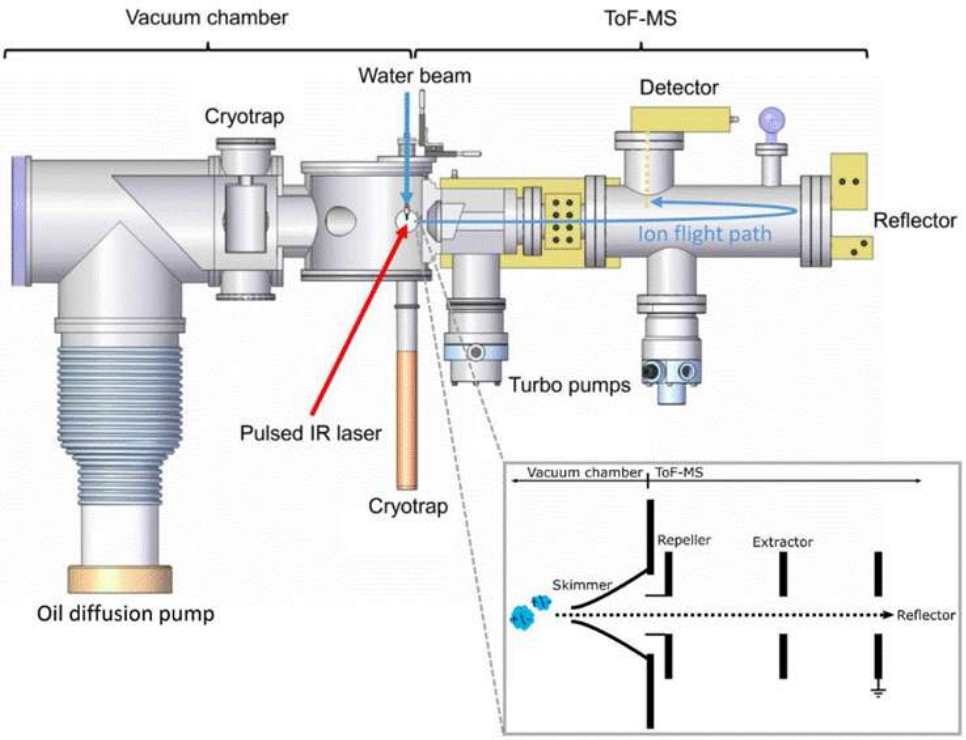

Figure 3-2. Experimental LILBID-TOF-MS setup for simulating hypervelocity impacts of ice (Klenner et al., 2019).

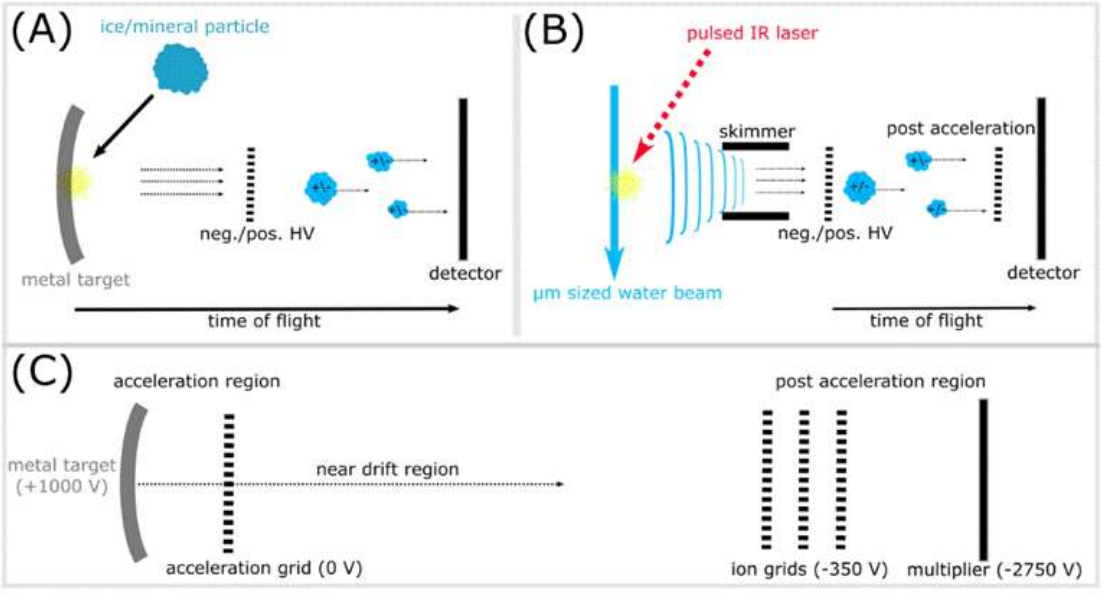

Figure 3-3. Comparison of impact ionization with mass spectrometers in space (A) and liquid beam laser desorption (B) for comparable energy impact and dispersion conditions by LILBID. The figure (C) shows the main acceleration and drift zones within the CDA Chemical Analyzer mass spectrometer onboard the Cassini (Klenner et al., 2019).

A distinctive feature of the LILBID technique is the delay time method. By adjusting the delay time, ions with a distinct initial velocity are selected for detection. For example, a short delay time allows detection of fast and high-energy ions, whereas a longer delay time enables observation of slower, lower-energy ions arriving later. Through this mechanism, the LILBID system can experimentally reproduce ion temperature distributions corresponding to different impact velocities. Klenner et al. (2019) reported that the mass spectra of ice particles obtained using the LILBID method show excellent agreement with those observed by the Cosmic Dust Analyzer (CDA) onboard the Cassini spacecraft.

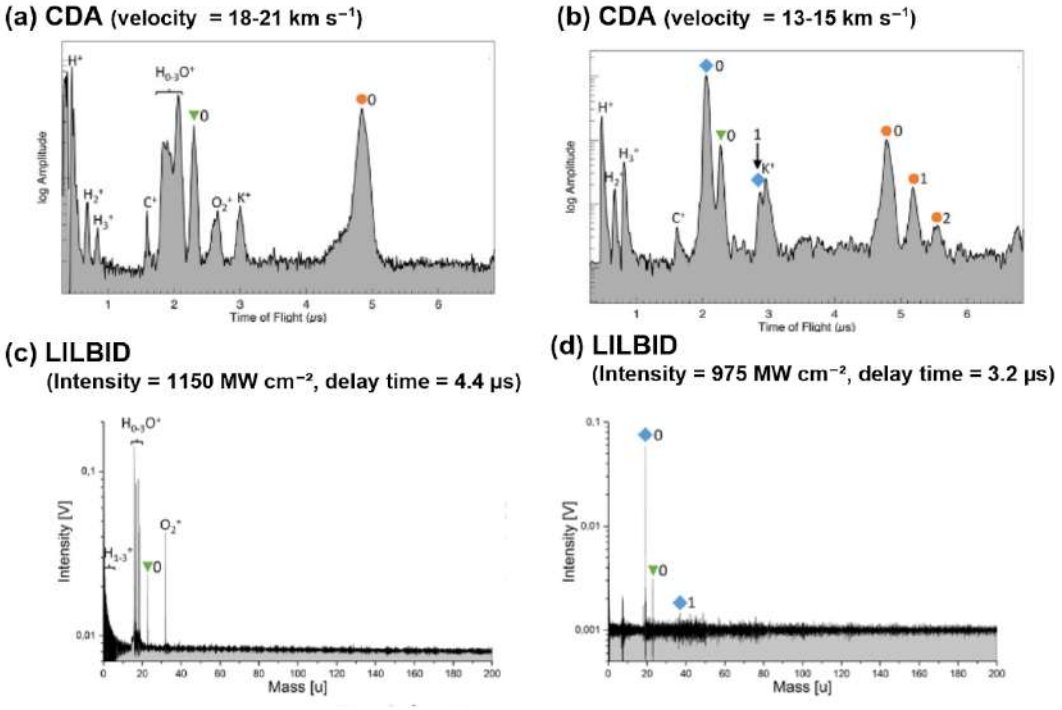

Figure 3-4. The panels (a) and (b) are the baseline corrected CDA mass spectra of ice grains at a velocity of 18 - 21 km s^{-1} and 13 - 15 km s^{-1}, respectively. And the panels (c) and (d) are the laboratory analogue of CDA Type 1 spectra (LILBID spectra) under a laser intensity of 1150 MW cm^{-2} and a delay time of 4.4 µs, and a laser intensity of 975 MW cm^{-2} and a delay time of 3.2 µs, respectively. The horizontal axis in (a) and (b) are time of flight in microseconds whereas the horizontal axis in (c) and (d) are atomic mass units.

In Klenner et al. (2019), it has also been reported that the mass spectra observed by the CDA can be accurately reproduced through laboratory experiments. However, the physical basis for the reason why the CDA spectra can be reproduced under specific laser irradiation conditions has not been sufficiently clarified. The delay time in the LILBID apparatus was empirically adjusted to selectively detect ions with particular energy distributions, thereby identifying the experimental conditions under which the resulting spectra matched with those observed by the CDA.

Klenner et al. (2019) suggested that the shape of the obtained mass spectra strongly depends on the initial plasma conditions, such as electron number density, energy distribution, and expansion velocity, immediately after irradiation. These parameters are fundamentally governed by scaling laws intrinsic to the impact process (e.g., Kissel & Krüger, 1987).

Therefore, if the initial plasma conditions generated by laser irradiation correspond to those produced by hypervelocity impacts, the resulting mass spectra should resemble the spectra observed with the CDA. However, because LILBID employs a unique technique involving laser irradiation of a liquid beam, unlike conventional solid-target impacts, direct comparison of absolute ion yields is difficult. Consequently, to directly compare laser irradiation with impact processes, we require a time-dependent simulation that is capable of resolving plasma generation, expansion, and ionization dynamics.

By understanding this background, this study aims to address the fundamental question:“Which physical parameters govern the mass spectra?” To answer this question, we introduce the two-temperature radiation hydrodynamics code P4P developed in Chapter 2, which focuses on the microscopic energy distribution of plasma. Then, we seek to derive the correspondence between the initial plasma conditions under laser irradiation and hypervelocity impacts, and to quantitatively evaluate their phase equivalence.

3.2.2 Conditions in P4P Simulations

In this study, laser irradiation on a water beam target was simulated using the P4P code in order to reproduce the laser conditions reported in the LILBID experiments by Klenner et al. (2019). Their experimental parameters were a wavelength of 2.84 μm, a pulse width of 7 ns, and an energy density ranging from 670 to 1150 MW cm^{-2}. These correspond to the following conditions associated with the impact velocities observed by the CDA for ice-particle impacts (Table 3-1).

Table 3-1. LILBID experimental conditions used to reproduce CDA ice-grain impact spectra (after Klenner et al. 2019)

Impact velocity (km s^{-1})	**Laser intensity (MW cm^{-2})**	**Delay time (μs)**
18–21	1150	4.4
13–15	975	3.2
9–11	975	3.8
	670	4.9
6.5–8.5	975	3.8
	670	4.9
	540	5.7
4–6	975	3.8
	670	4.9
	445	6.3

For hypervelocity impacts, the impact velocities were (a) 19.5 km s^{-1}, (b) 14.0 km s^{-1}, (c) 10.0 km s^{-1}, (d) 7.5 km s^{-1}, and (e) 5.0 km s^{-1}, respectively. Klenner et al. (2019) mentioned that they used the CDA data whose ion yields were between 12 fC and 30 fC to ensure a similar signal-to-noise ratio for the individual spectra at all velocity regimes. Thus, this study changed the projectile sizes for each impact velocity to aim at the same ion yield regime. As for laser irradiation, while Klenner et al. (2019) used some of the co-added spectra produced from a mixture of different delay time windows, we conducted (a) 1150 MW cm^{-2} with delay time = 4.4 μs, (b) 975 MW cm^{-2} with delay time = 3.2 μs, (c) 975 MW cm^{-2} with delay time = 3.8 μs, (d) 670 MW cm^{-2} with delay time = 4.9 μs, (e) 540 MW cm^{-2} with delay time = 5.7 μs, and (f) 445 MW cm^{-2} with delay time = 6.3 μs, respectively.

The spatial profile of the laser beam was assumed to follow a Gaussian distribution with a full width at half maximum (FWHM) of 100 μm, corresponding to a standard deviation of $\sigma \approx 42.5$ μm. For the impact simulations, a 10 μm-diameter ice projectile was modeled impacting with a Rh target at velocities of 14 km s^{-1} and 10 km s^{-1}. Table 3-2 summarizes the main parameters used in the P4P simulations. For both the laser irradiation and impact cases, the vacuum level was set to 5×10^{-5} Pa (Klenner et al., 2019). In the laser irradiation simulations, the spatial resolutions were Δx = 0.1 μm and Δy = 0.5 μm, and the computational domain was extended up to 15 ns. For the hypervelocity impact simulations, Δx = 0.07 μm and Δy = 0.2 μm were used, and the simulation time was extended up to 3 ns.

Table 3-2. Values of the main parameters used in the P4P simulations.

Parameters	Values for impact	Values for laser ablation
Projectile size	3.75 μm (for 5.0 km/s) 2.00 μm (for 7.5 km/s) 1.40 μm (for 10.0 km/s) 0.80 μm (for 14.0 km/s) 0.29 μm (for 19.5 km/s)	–
Δx	21.9/ 12.2/ 7.1/ 3.4/ 1.9 nm	0.5 μm
Δy	19.8/ 11.0/ 6.4/ 3.1/ 1.7 nm	0.1 μm
Cell per Projectile Radius	167	–
High Resolution Zone Width	6600/ 3700/ 2100/ 1000/ 570 nm	150 μm
High Resolution Zone Height	19800/ 11000/ 6400/ 3100/ 1700 nm	50 μm
High Resolution Target Depth	990/ 550/ 320/ 160/ 90 nm	8 μm
Extension Width	4000/ 2200/ 1300/ 620/ 340 nm	150 μm
Extension Top	4000/ 2300/ 1200/ 560/ 310 nm	325 μm
Extension Bottom	990/ 550/ 320/ 160/ 90 nm	50 μm
End Time	1580/ 630/ 260/ 90/ 40 ps	8 ns
Vacuum Level	5×10^{-5} Pa	5×10^{-5} Pa

In the charge calculations performed with the P4P code, the model in Chapter 2 assumed monoatomic species. Therefore, for atomic systems, each computational cell represents a single atom. However, for water molecules, which consist of three atoms, an averaged atomic representation was adopted. Specifically, the effective atomic number and atomic mass were calculated as the mean values of the constituent atoms, yielding:

$$\bar{Z} = 3.33 = (8 + 1 + 1) / 3 \quad (3\text{-}1),$$

$$\bar{A} = 6.0 = (16 + 1 + 1) / 3 \quad (3\text{-}2),$$

respectively. The outer-shell potential in the ion-sphere model plays a crucial role in determining the effective ionization threshold. For water, this potential was set to –33.4 eV, corresponding to the

potential energy of the O 2s orbital of the H_2O molecule, as defined by Shibaguchi et al. (1977); Fransson et al. (2016). With this configuration, the ionization degree computed in the P4P post-processing routine is expected to correspond to the detachment of the shallowest molecular orbital, the $1b_1$ orbital (–12.6 eV). To verify this, a Boltzmann distribution was plotted for the cell where the computed ionization degree was 0.017, using the ion temperature in that cell (3.40 eV). The fraction of particles with energy exceeding 12.6 eV was found to be 0.024 (Figure 3-5). This close agreement between the calculated ionization degree (0.017) and the Boltzmann-predicted fraction (0.024) indicates that the post-processing ionization calculation accurately reproduces a model in which electrons from the $1b_1$ orbital (–12.6 eV) are detached.

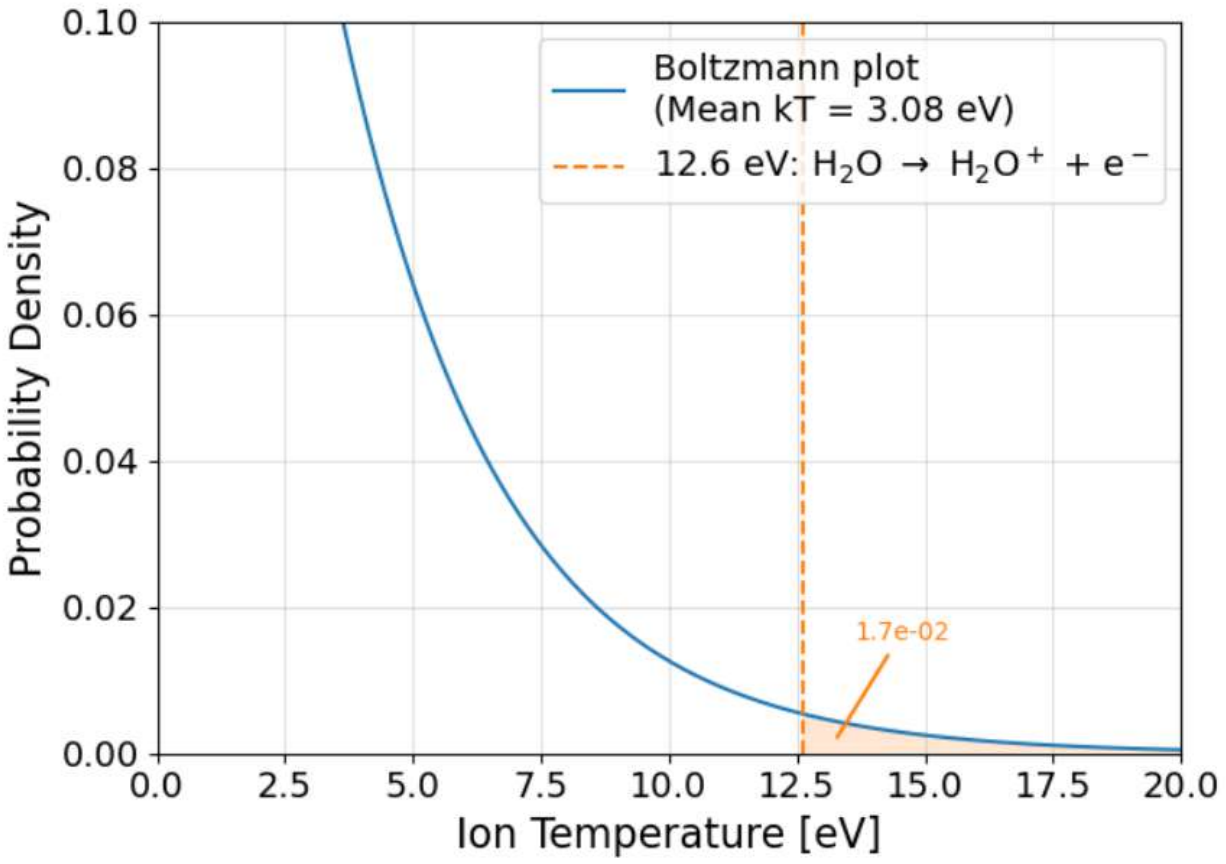

Figure 3-5. Boltzmann distribution for the cell where the computed ionization degree was 0.017, using the ion temperature in that cell (3.40 eV). The fraction of particles with energy exceeding 12.6 eV was found to be 0.024.

This ionization process corresponds to the reaction,

$$H_2O \rightarrow H_2O^+ + e^- \qquad (3\text{-}3).$$

The 1b1 orbital electrons are involved in the O–H bonding; therefore, the resulting H_2O^+ ions are highly unstable. Such water cations undergo ultrafast proton transfer to produce hydroxyl radicals (OH) and hydronium cations (H_3O^+) within less than 100 fs (Lin et al., 2021), as follows:

$$H_2O^+ \rightarrow OH^+ + H \qquad (3\text{-}4),$$

$$H_2O^+ + H_2O \rightarrow H_3O^+ + OH \qquad (3\text{-}5).$$

These reaction products, particularly hydronium cations, have also been identified experimentally by Klenner et al. (2019) and are known to play a key role as precursors in the formation of water ion clusters. The candidate ran the P4P code previously constructed (e.g. Nagatomo et al., 2006; 2015), and designed the analytical model for H_2O and executed the calculations.

3.3 Simulation Results

3.3.1 Plasma Generation Process under Hypervelocity Impact

Figure 3-6 and 3-7 shows the density distribution and charge generation , as well as the electron and ion temperature distributions, for a 0.8-μm-diameter ice projectile impacting a Rh target at 14 km s^{-1}. Immediately after impact ($t \simeq ¼$ ts, where $ts = 2r_p / V_{imp}$ is the characteristic timescale, r_p is the projectile radius in meters, and V_{imp} is the impact velocity in meters per second), the projectile begins to penetrate the target surface, and a localized jetting region emerged. After $t \simeq ½$ ts, as the material within the projectile and near the target interface undergoes free expansion in the rearward direction, weak ionization reappears, but the corresponding temperature remains low. This indicates

that at a velocity of 14 km s^{-1}, the shock energy is insufficient to maintain a high electron temperature or sustained ionization. Unlike laser irradiation, the ion temperature expansion proceeds the electron temperature expansion, which implies thermal energy of impact plumes is derived from kinetic energy that projectiles used to have before impacts.

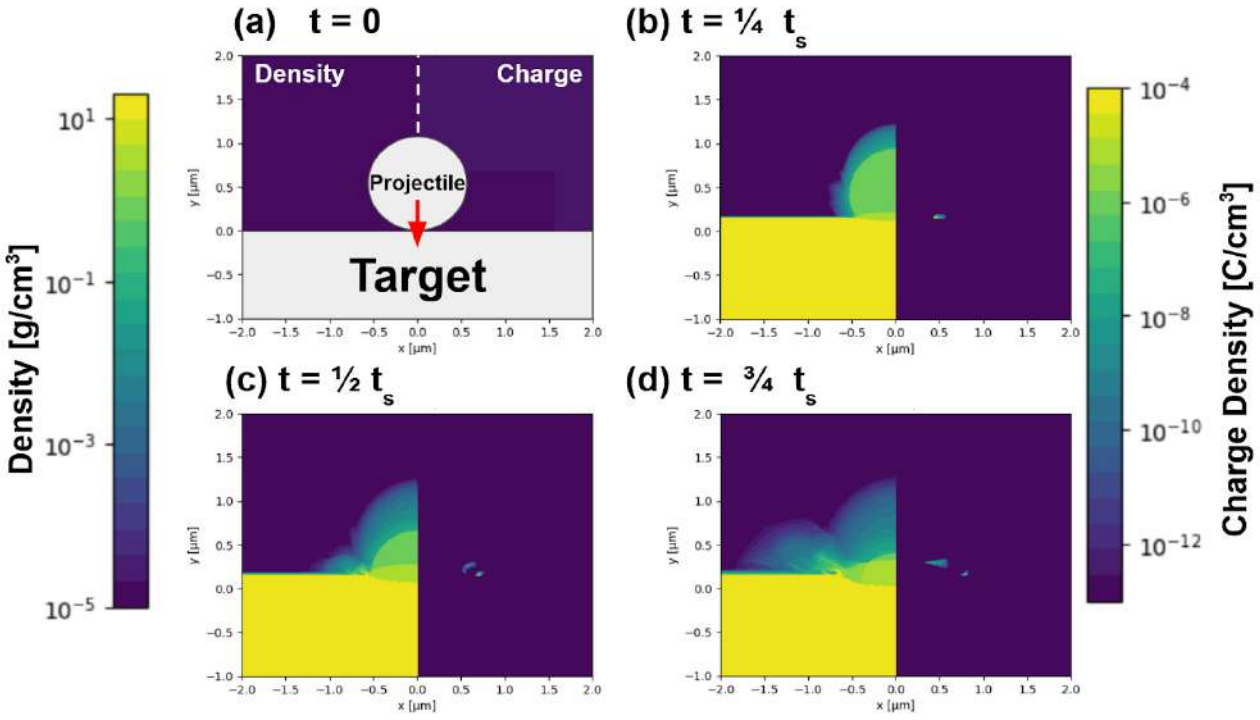

Figure 3-6. Temporal evolution of density (left) and charge density (right) distributions during a hypervelocity impact, between a 0.8 μm H_2O ice projectile and a rhodium target at 14 km s^{-1}. This impact velocity is compared to the LILBID experiment whose laser intensity is 975 MW cm^{-2} and delay time is 3.2 μs, shown in Figure 3-11. The t_s is the characteristic impact timescale, defined as the ratio of the projectile diameter to the impact velocity ($t_s = 2r_p / v_{imp}$).

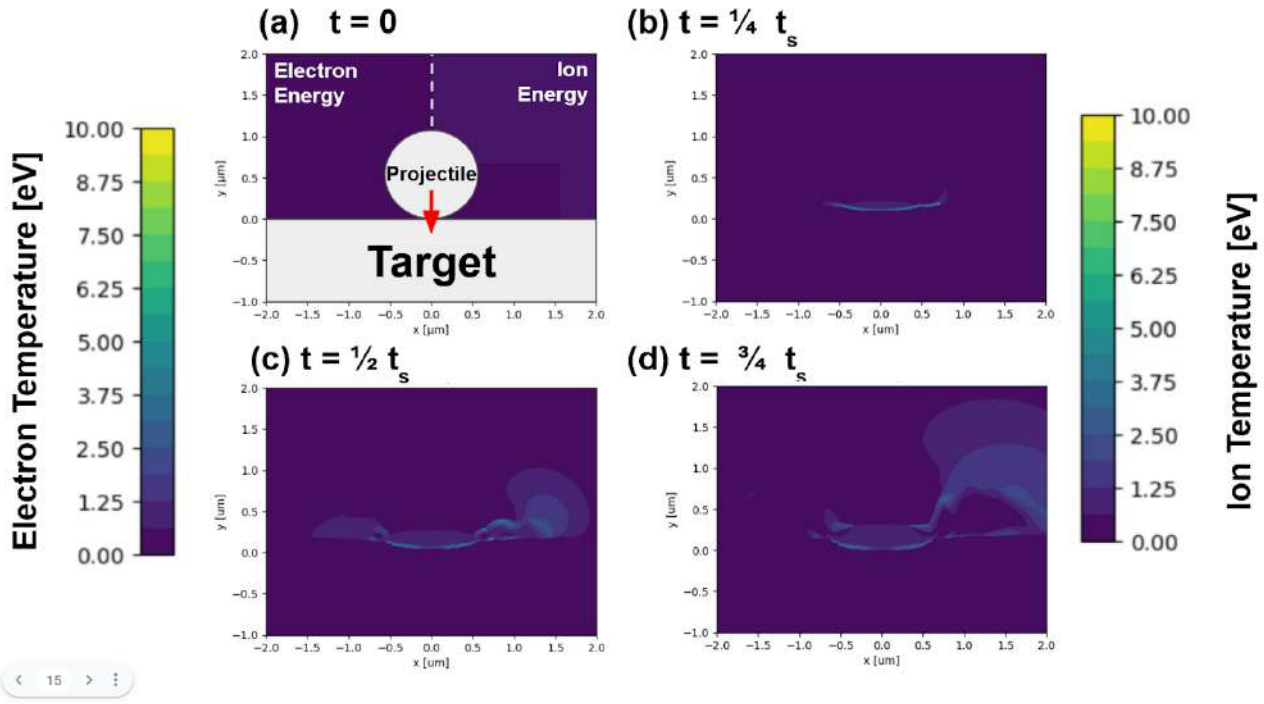

Figure 3-7. Temporal evolution of electron temperature (left) and ion temperature (right) distributions during a hypervelocity impact, between a 0.8 μm H_2O ice projectile and a rhodium target at 14 km s^{-1}. This impact velocity is compared to the LILBID experiment whose laser intensity is 975 MW cm^{-2} and delay time is 3.2 μs, shown in Figure 3-12. The scale bar is the same as Figure 3-12. The t_s is the characteristic impact timescale, defined as the ratio of the projectile diameter to the impact velocity ($t_s = 2r_p / v_{imp}$).

On the other hand, in the hypervelocity case exceeding 20 km s^{-1} discussed in Chapter 2, strong ionization dominated both at the projectile–target interface and within the rear expansion region. Under the present 14 km s^{-1} condition, the shock energy is much smaller. Although transient heating and ionization due to jetting occur locally, the overall charge production, particularly from low-temperature expansion, is significantly lower than that under the laser-irradiation condition.

Figure 3-8 presents the simulated ion yield for ice projectiles obtained using the P4P code, together with experimental ion-yield data for iron projectiles reported by Stübig (2002) for

comparison. Direct experimental measurements of ion yield from hypervelocity impacts of ice projectiles do not exist, primarily because ice particles cannot currently be accelerated to the velocity range of this study. Timmermann and Grün (1991), and Burchell et al. (1996) performed dust-impact experiments on icy targets over a velocity range of 3–60 km s^{-1} and derived a scaling law for the mass and velocity dependence of ion yield for ice surfaces. Burchell et al. (1996) describe the ionization for impacts on ice by $I/m = cv^{\beta}$, and found that $c = 0.0040 \pm 0.0008$ and $\beta = 4.12 \pm 0.41$. This value is an order of magnitude lower than the value for impacts on gold and iron (Göller and Grün, 1989; Burchell et al., 1999). Our P4P simulation results reproduce this trend: the ion yield for ice projectiles impacting a rhodium target remains below 2 ~ 3 orders of magnitude of that for iron projectiles, consistent with comparative hypervelocity impact data reported by Stübig (2002). While the absolute scaling differs, this agreement in relative magnitude is notable given the different experimental configurations (ice target vs. ice projectile) and the known sensitivity of ion yield to material properties and charging geometry, quantities that can vary by orders of magnitude.

Furthermore, the P4P model naturally reproduces the characteristic slope change in ion-yield scaling observed around ~10–14 km s^{-1} in multiple previous studies (e.g., Göller and Grün, 1989; Stübig, 2002). Göller and Grün (1989) identified two such inflection points (~6.5 km s^{-1} and ~12 km s^{-1}), attributing it to their specific experimental geometry. Accordingly, the absence of the lower-velocity break in our results is reasonable, while the emergence of the ~12 km s^{-1} transition reinforces the physical consistency of the P4P simulations with experimental knowledge. These facts strongly support the physical validity of the P4P simulation in modeling hypervelocity impact -induced plasma from water ice.

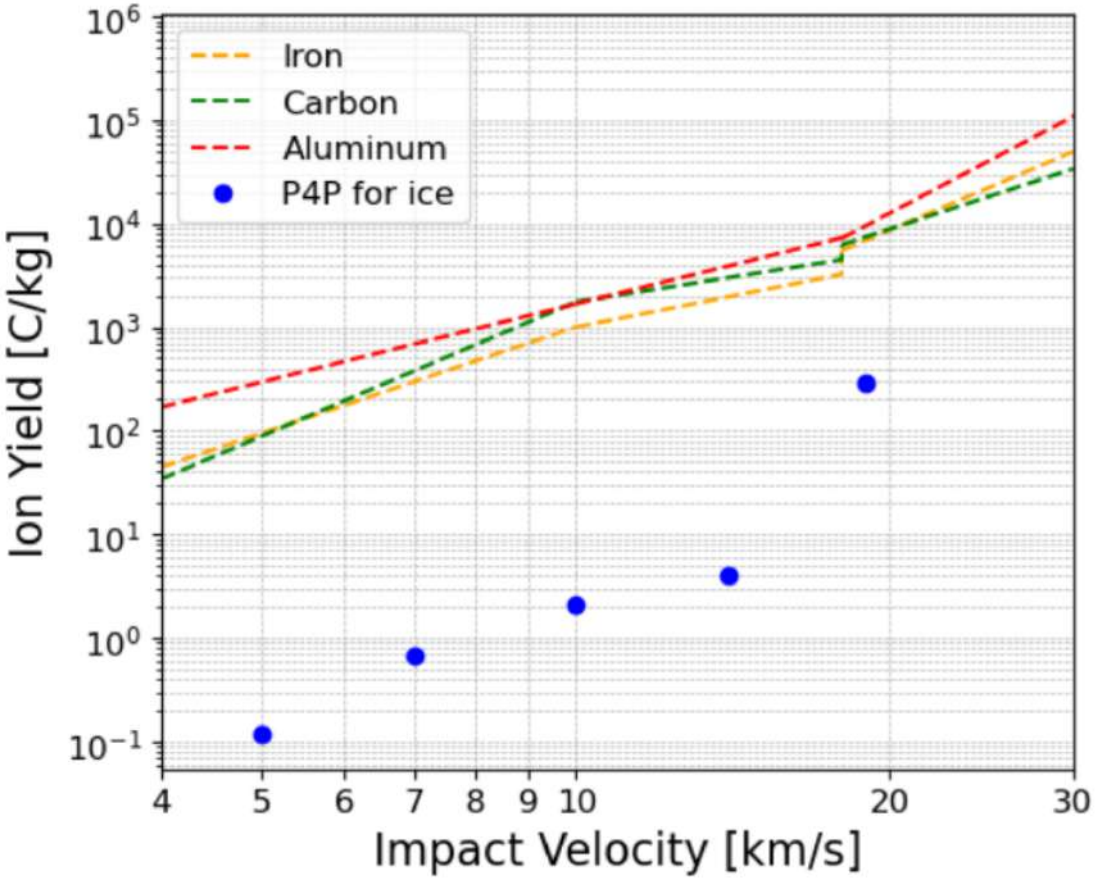

Figure 3-8. Ion yield for ice by the P4P simulation, compared to the ion yield for Aluminum, iron, carbon projectiles impact to rhodium target by the impact experiment (Stübig, 2002).

3.3.2 Temporal Waveforms and Ion temperature Distribution under Hypervelocity Impacts

Figure 3-9 shows the temporal evolution of the generated charge and the spatially averaged ion temperature. Note that the horizontal axis represents time normalized by the characteristic timescale scale (defined in Section 3.2.2); therefore, the absolute time values differ among cases due to variations in projectile size. Interpretation must therefore focus on the relative evolution with respect to the characteristic timescale.

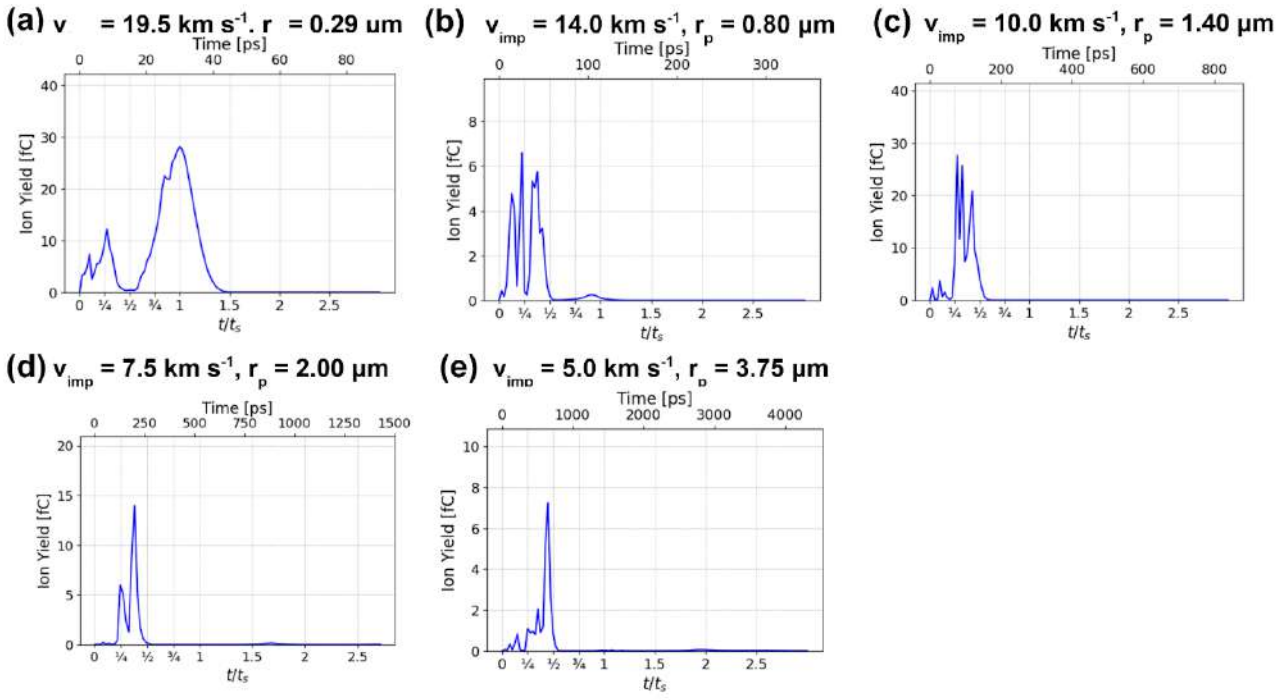

Figure 3-9. Temporal evolution of generated charge by hypervelocity impact, whose impact velocity = (a) 19.5 km s^{-1}, (b) 14.0 km s^{-1}, (c) 10.0 km s^{-1}, (d) 7.5 km s^{-1} and (e) 5km s^{-1}. Horizontal axes are normalized by the characteristic timescale ($t_s = 2r_p/v_{imp}$).

Across most impact velocities, the total charge reaches a maximum at approximately t ≃ ¼ ts. An exception is observed for the 19.5 km s^{-1} case, where the early rise is comparatively smaller and the dominant peak is broader. This behavior reflects a transition in the dominant ion-production mechanism. For impacts between 5.0 and ~14.0 km s^{-1}, ion generation is primarily driven by jetting—high-temperature material being ejected from the projectile–target interface. In contrast, at ~19 km s^{-1}, ion production becomes dominated by the pressure-relaxation process associated with rarefaction waves propagating from the rear side of the projectile, as discussed in Section 2.3.2. This mechanistic transition is closely related to the change in ion-yield trend observed in Figure 3-8, consistent with breakpoints reported in previous experimental and theoretical studies in the 10–14 km s^{-1} velocity range.

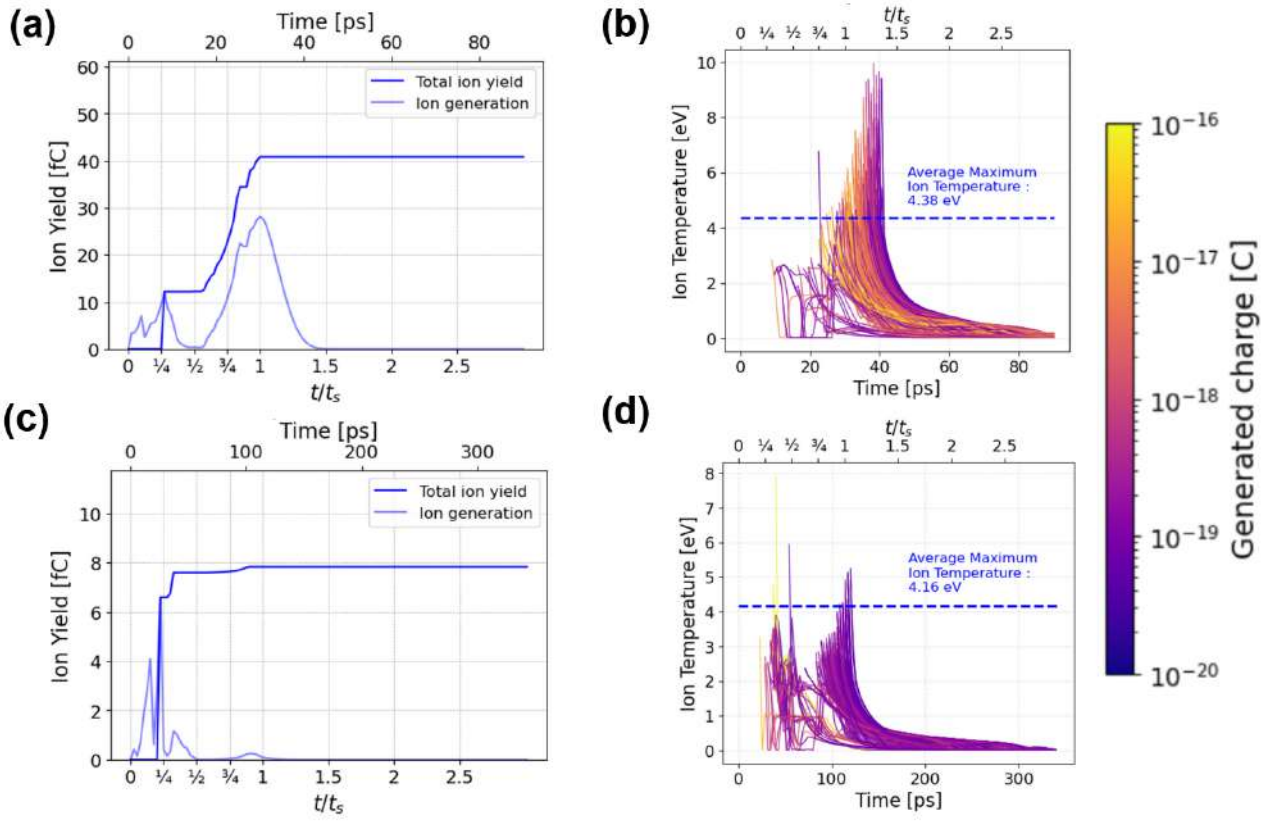

Figure 3-10. (a) Temporal evolution of the ion yield. The light blue line represents the net ion generation, while the blue line indicates the time-accumulated ion yield. (b) Time evolution of the ion temperature for individual ions up to 2.5 t_s under an impact velocity of 19.0 km s^{-1}. (c) and (d) show the corresponding ion yield and ion temperature obtained under an impact velocity of 14.0 km s^{-1}, respectively. The blue dotted horizontal lines in (b) and (d) indicate the charge-weighted average of the maximum ion temperature experienced by each ion. Horizontal axes are normalized by the characteristic timescale ($t_s = 2r_p/v_{imp}$).

Figure 3-10 (a) and (c) show the time evolution of the ion yield under an impact velocity of 19.0 km s^{-1}. The light blue lines represent the raw P4P output of ion generation, while the blue lines indicate the accumulated total ions that are extracted by the electric field biased on the CDA target, as estimated using the method described in Section 3.2.2. In Figure 3-10 (b), a large number of ions are generated between 1 t_s and 1.5 t_s. This ion population constitutes a substantial fraction of the

total ion yield and dominates the charge-weighted average of the maximum ion temperature experienced by each ion, which is 4.38 eV. In contrast, in Figure 3-10 (d), the temperature of ions generated between 1 t_s and 1.5 t_s becomes lower, while the relative contribution of ions originating from the jetting region (¼ t_s to ½ t_s) increases. As a result of this balance, the charge-weighted average of the maximum ion temperature decreases to 4.16 eV.

3.3.3 Plasma Formation Process under Laser Irradiation Conditions

Figures 3-11 and 3-12 show the temporal evolution of the density distribution, charge generation, and electron/ion temperature distributions under laser irradiation at an energy density of 975 MW cm^{-2}.

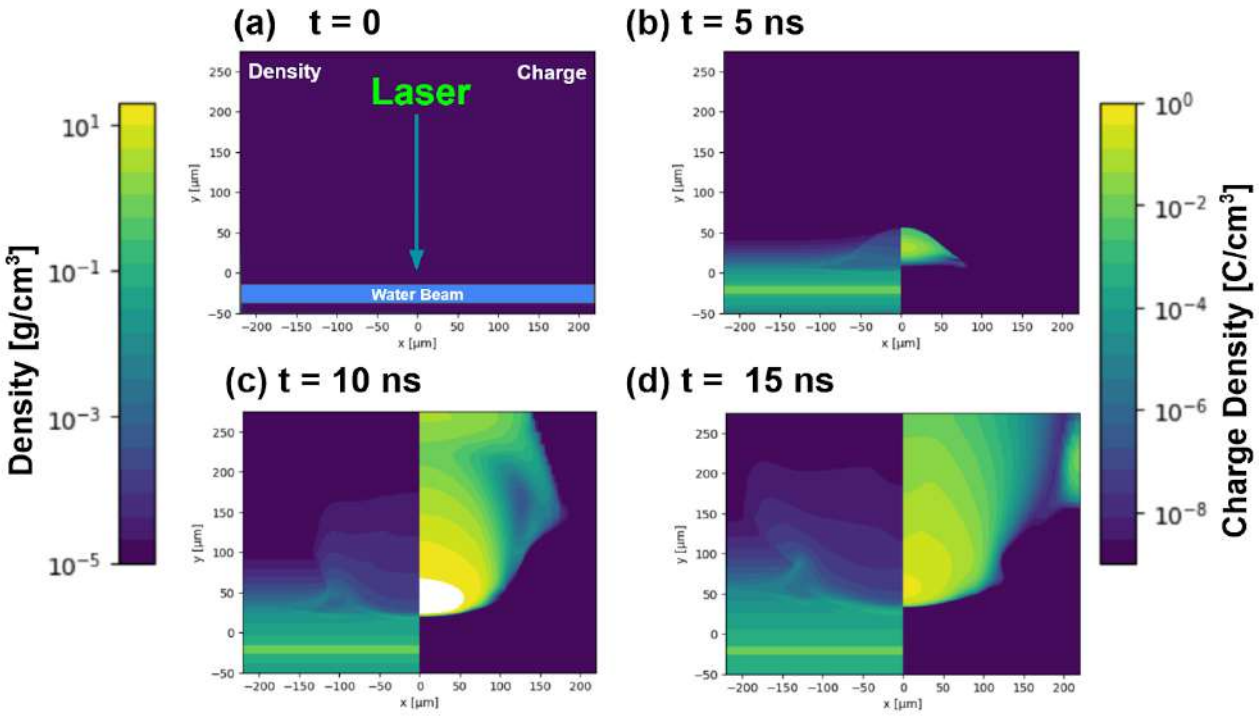

Figure 3-11. Temporal evolution of density (left) and charge density (right) distributions during a laser ablation, where the power density is 975 MW cm^{-2} and the target material is H_2O ice. This impact velocity is compared to the CDA data whose impact velocity is 13-15 km s^{-1}, shown in Figure 3-6.

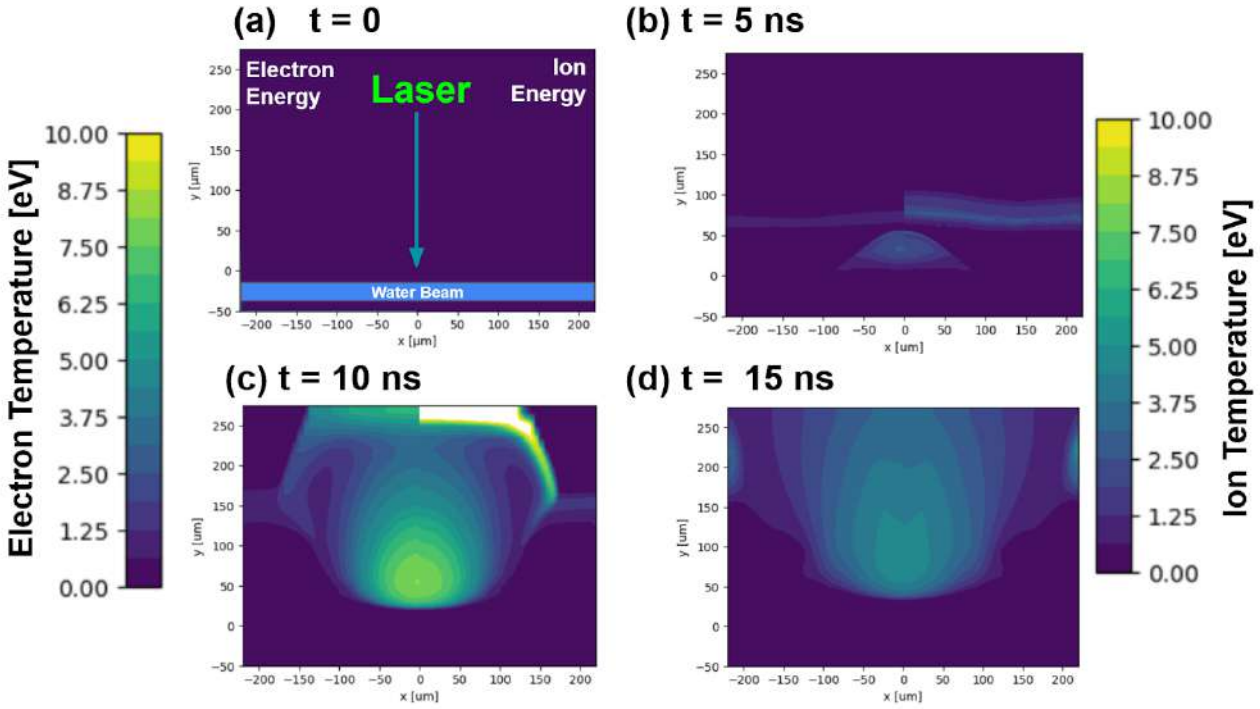

Figure 3-12. Temporal evolution of electron temperature (left) and ion temperature (right) distributions during a laser ablation, where the power density is 975 MW cm^{-2} and the target material is H_2O ice. This impact velocity is compared to the CDA data whose impact velocity is 13-15 km s^{-1}, shown in Figure 3-7. The scale bar is the same as Figure 3-7.

Immediately after the laser pulse (t = 0–5 ns), rapid heating occurs at the target surface, leading to the formation of a plasma plume as the water expands explosively. The tip of the plume grows upward from the irradiated surface and reaches a stand-off distance of approximately 30 μm at t = 10 ns. As the plume develops, electrons near the irradiated surface are preferentially accelerated and emitted, forming a localized ionization region. Meanwhile, as the plume expands, the laser energy is absorbed further into the material, and the high-charge density region gradually extends upward. The electron temperature rises sharply immediately after irradiation, forming a high-temperature region that precedes the ion temperature. This occurs because the laser energy is

mainly absorbed through electrons, resulting in a non-equilibrium state in which the electron temperature exceeds the ion temperature at t = 5 ns.

Subsequently, at t = 10 ns, energy exchange between electrons and ions progresses, and both species reach a nearly thermal equilibrium state within the plasma plume. At the same time, the ion temperature locally increases at the shock front near the tip of the plume, reflecting the conversion of kinetic energy into thermal energy through the artificial viscosity. Because this region is of low density, its influence on the overall energy balance of the system is limited.

3.3.4 Temporal Profile and Ion temperature Distribution under Laser Irradiation

Figure 3-13 (a) and (c) show the time-resolved ion yield passing the delay-time selection. Under both laser conditions, the ion yield exhibits a moderate peak at approximately t ≃ 11–12 ns, slightly after the peak of the relative laser intensity at 10 ns. The peak ion yields in (a) and (c) are 11.2 μC and 9.0 μC, respectively, and their ratio is close to the ratio of the corresponding laser intensities. However, due to the difference in delay time between the two conditions, there is little difference between the total ion yield and the delay-time-selected ion yield under a laser intensity of 1150 MW cm^{-2} with a delay time of 4.2 μs, whereas the difference is relatively larger under a laser intensity of 975 MW cm^{-2} with a delay time of 3.2 μs. This indicates that a longer delay time allows a larger fraction of ions to be selected.

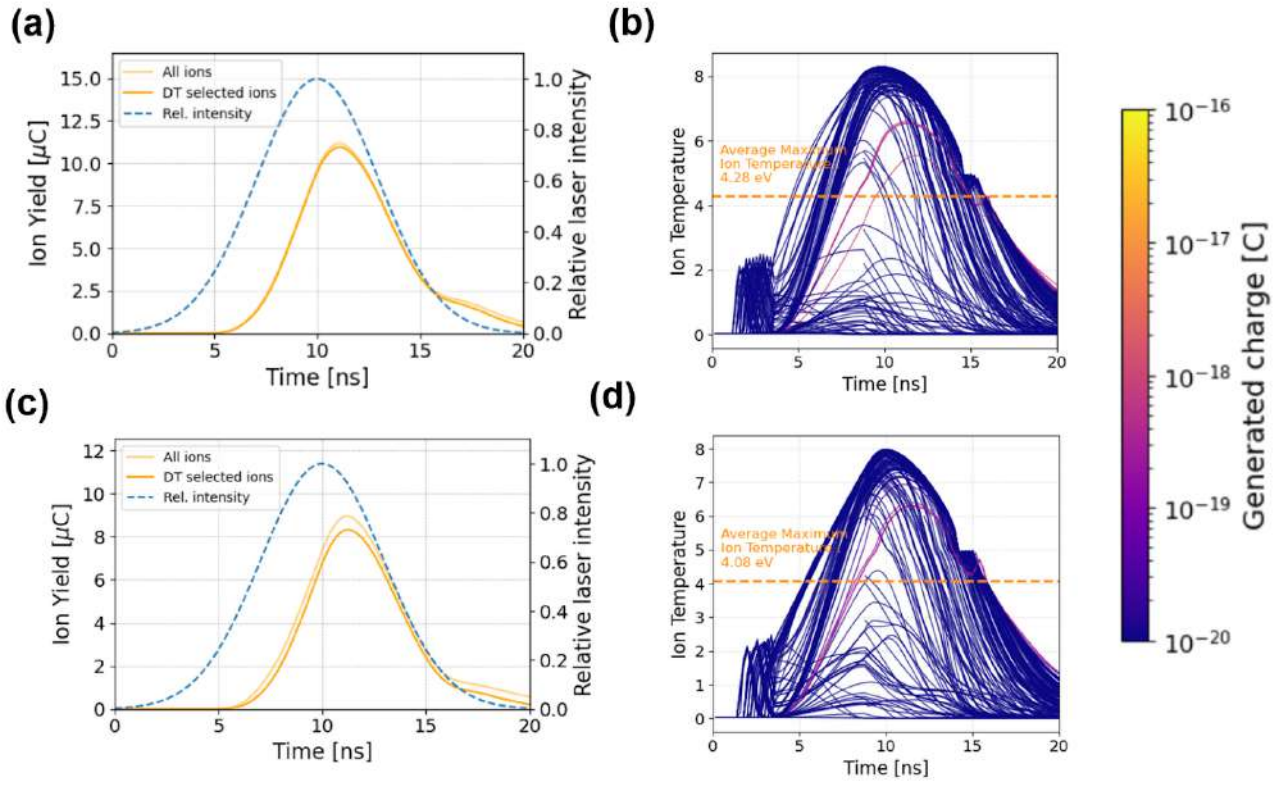

Figure 3-13. (a) Temporal evolution of the yield of all ions and the ions passing the delay-time selection together with the relative laser intensity under a laser intensity of 1150 MW cm^{-2} and a delay time of 4.4 μs. (b) Time evolution of the ion temperature for individual ions that remain at 20 ns and pass the delay-time selection under the same condition. The color bar represents charge for each ion. (c) and (d) show the corresponding results obtained under a laser intensity of 975 MW cm^{-2} and a delay time of 3.2 μs. The orange dotted horizontal lines in (b) and (d) indicate the charge-weighted average of the maximum ion temperature experienced by each ion.

Figure 3-13 (b) and (d) show the time-resolved ion temperature for individual ions that remain at 20 ns and pass the delay-time selection. The temperature for each ion experienced the peak around 11 - 12 ns, that corresponds to the peak of ion yield. In the LILBID system, ions generated by laser irradiation first travel through a field-free drift region of approximately 25 mm. After a delay time of a few microseconds, the ions are extracted by an electric field. During this

field-free drift period, a significant fraction of ions can recombine before being detected. Since the P4P code cannot simulate ion dynamics over microsecond timescales following nanosecond laser irradiation, we instead extract ions that remain at 20 ns and evaluate the charge-weighted average of the maximum ion temperature experienced by each ion.

A range of skimmer diameters from 5 to 20 mm and acceleration zone lengths from 10 to 250 mm were adopted (see Figure 3-2, 3-3). The resulting charge-weighted average maximum ion temperature varies with these parameters, ranging from 4.19 to 4.28 eV for a laser intensity of 1150 MW cm^{-2} with a delay time of 4.4 μs, and from 3.98 to 4.08 eV for a laser intensity of 975 MW cm^{-2} with a delay time of 3.2 μs. Importantly, the difference between the two laser irradiation and extraction conditions remains approximately 0.2 eV, indicating that the relative difference in ion temperature is robust against uncertainties in the delay-time selection parameters.

3.4 Discussion

Interestingly, the average ion energies shown in Figures 3-10 and 3-13 exhibit similar trends. For both laser irradiation and hypervelocity impact, panels (b) and (d) in these figures demonstrate an increase in average ion temperature with increasing laser intensity or impact velocity. More notably, a quantitative correspondence is observed between the two cases. In Figure 3-10, condition (b) (impact velocity: 19.5 km s^{-1}) yields an average ion temperature of 4.38 eV, while condition (d) (impact velocity: 14.0 km s^{-1}) yields 4.16 eV. Similarly, in Figure 3-13, condition (b) (laser intensity: 1150 MW cm^{-2}, delay time: 4.4 μs) produces an average ion temperature of 4.25 eV, whereas condition (d) (laser intensity: 975 MW cm^{-2}, delay time: 3.2 μs) yields 4.06 eV. These values are summarized in Table 3-3. In both the laser irradiation and hypervelocity impact cases, the difference between conditions (b) and (d) is approximately 0.2 eV. Although a systematic offset of

about 0.1 eV exists between the two methods, this discrepancy is likely attributable to uncertainties in the simulation of the delay-time selection and the treatment of the electric field during ion extraction.

These quantitative similarities strongly suggest that the charge-weighted average of the maximum ion temperature can serve as a key indicator linking hypervelocity impact generated plasmas-mass spectra and laser irradiation generated plasmas-mass spectra. Since chemical reaction rates depend exponentially on temperature, similarity in ion temperature implies similarity in the chemical pathways responsible for the observed mass spectra. This provides a fundamental physical basis for the widely observed spectral equivalence between laser ablation and hypervelocity impact experiments.

Table 3-3. The charge-weighted average of the maximum ion temperature experienced by each ion calculated by the P4P simulations.

Condition	Hypervelocity impact	Laser ablation
19.5 km s^{-1}/ 1150 MW cm^{-2} and 4.4 μs	4.38 eV	4.28 eV
14.0 km s^{-1}/ 975 MW $cm^{-2}$and 3.2 μs	4.16 eV	4.08 eV

3.5 Future work

Despite the similarity observed in the charge-weighted average of the maximum ion temperature, this correspondence has so far been confirmed only under the two hardest and simplest conditions discussed in Klenner et al. (2019). In that study, CDA spectra were reproduced by co-adding LILBID spectra obtained using multiple delay-time windows, rather than by a one-to-one correspondence between individual experimental conditions. Specifically, the authors combined spectra acquired under different laser irradiation conditions to simulate CDA impact velocity ranges, such as:

- 9–11 km s^{-1} impacts using laser intensities of 975 MW cm^{-2} (delay time: 3.8 μs) and 670 MW cm^{-2} (4.9 μs)
- 6.5–8.5 km s^{-1} impacts using 975 MW cm^{-2} (3.8 μs), 670 MW cm^{-2} (4.9 μs), and 540 MW cm^{-2} (5.7 μs)
- 4–6 km s^{-1} impacts using 975 MW cm^{-2} (3.8 μs), 670 MW cm^{-2} (4.9 μs), and 445 MW cm^{-2} (6.3 μs).

A direct quantitative comparison between these mixed conditions and the present simulation results remains to be performed.

In addition, Table 3-3 shows that the difference in the average ion temperature between two hypervelocity impact conditions or two laser irradiation conditions is on the order of 5%. We must be cautious that this modest change in temperature can lead to the drastic variations in the mass spectra observed in CDA and LILBID data shown in Figure 3-4. Therefore, a more comprehensive modeling framework is required, in which the thermodynamic parameters obtained from the P4P simulation are directly coupled to chemical reaction simulations capable of predicting mass spectra.

Such an approach would enable a more rigorous comparison between laser irradiation and hypervelocity impact experiments. The present study represents a first step toward this quantitative numerical comparison.

3.6 Summary

This chapter established a quantitative and physically grounded framework linking laser irradiation and hypervelocity impact as sources of impact-relevant plasmas and mass spectra. First, we clarified why direct laboratory reproduction of micrometeoroid impacts at several–tens of km s^{-1} is intrinsically limited, motivating the use of nanosecond-pulse laser irradiation to generate thermodynamically equivalent high-temperature, high-pressure states. We then formalized the similarities and differences in energy-deposition pathways by contrasting shock-Hugoniot trajectories (impact) with pressure-driven heating and partial vaporization (laser), and identified the physical quantities that should anchor phase equivalence (pressure, temperature, entropy, degree of ionization).

Using the P4P two-temperature radiation-hydrodynamics code validated in Chapter 2, we simulated both laser irradiation and hypervelocity impact under conditions comparable to Klenner et al. (2019) and to CDA observations. For laser cases, we reproduced the time-resolved ion yield and energy of ions selected by delay-time windows.

Despite these mechanistic differences, the charge-weighted average of the maximum ion temperature, for matched laser and impact conditions quantitatively coincide (e.g., laser 1150 MW cm^{-2} / 4.4 μs vs. impact 19.5 km s^{-1}; laser 975 MW cm^{-2} / 3.2 μs vs. impact 14.0 km s^{-1}). This supports the charge-weighted average of the maximum ion temperature as a practical bridge

variable connecting laser-driven and impact-driven plasmas and provides a physical basis for the spectral similarities reported in laboratory analogues and space observations.

These results justify treating laser irradiation as a controlled analog for hypervelocity impacts when matched in terms of ion temperature (and associated thermodynamic state) rather than by pressure or fluence alone. This motivates Chapter 4's experimental verification with EI-MS under LILBID-like conditions and sets the stage for Chapter 5's exploration of photoionization (PI) to reduce fragmentation while preserving molecular structures in impact-generated gas.

Chapter 4 Laser Ablation Experiments as Simulated Impacts and Electron-impact Ionization Mass Spectrometry Observations

4.1 Experimental Validation of Laser–Impact Ionization Analogy Using Organic Particle Analogs

In the previous chapter, we numerically investigated the physical correspondence between laser ablation and hypervelocity impact ionization using the P4P radiation–hydrodynamics code. Those simulations demonstrated that, under certain ion energy conditions, the plasma generation processes in both phenomena exhibit comparable chemical states, suggesting a potential equivalence between laser fluence and impact velocity. Building on this theoretical foundation, the present chapter transitions from numerical modelling to experimental validation, employing laser irradiation experiments as controlled analogues of impact events. Here, we aim to reproduce the vaporization and ionization processes of micrometeoroid impacts in the laboratory and to evaluate whether analysis of impact-sublimated gas can better preserve molecular structures than direct MS analysis of impact-induced plasma. Before presenting the experimental approach, it is essential to review previous impact studies that have investigated the underlying chemical and physical processes during hypervelocity impacts.

When micrometer-sized particles impact at several km s^{-1} or higher, the resulting shock heating causes rapid vaporization and ionization, accompanied by extensive molecular fragmentation and recombination. In-situ mass spectrometers (MS) onboard spacecraft have observed such events in planetary environments, providing insights into the chemical and physical

processes during dust impacts. Consequently, the measured MS spectra often contain a complex mixture of intact molecular ions, fragments, and secondary clusters, making it difficult to trace the original composition of the projectile material (e.g., Hsu et al., 2018; Postberg et al., 2018; Khawaja et al., 2019; Postberg et al., 2023). These projectiles can contain astrobiologically important organic compounds such as polymers (e.g., Postberg et al., 2018), aromatic hydrocarbons (e.g. Khawaja et al., 2019; Waite Jr. et al., 2018, Khawaja et al., 2025), and amino acid precursors (e.g., Elsila et al., 2009; Altwegg et al., 2016), which are known to exist in carbonaceous chondrites (e.g., Sephton 2002; Furukawa et al., 2019), cometary grains (e.g., Sandford et al., 2006), interplanetary dust particles (IDPs; e.g., Allamandola et al., 1987; Pizzarello et al., 2006), and surface of asteroids (e.g., Naraoka et al., 2023; Yabuta et al., 2023). These observations suggest that organic-rich dust grains may have played a central role in delivering prebiotic molecules to early planetary surfaces.

However, it is challenging to identify specific organic molecules from the complex mixture of intact molecular ions and fragments observed in these spectra. The ionization and fragmentation observed in previous Van de Graaff electrostatic accelerator experiments (Burchell et al., 1999; 2002; Burchell and Armes, 2011; Kissel and Krueger, 2001; Goldsworthy et al., 2002; 2003; Srama et al., 2009; Mikula et al., 2023) indicate that molecular identity is rapidly lost above several km s^{-1}, leading to largely atomic or small ionic fragments. This raises a crucial problem for in-situ compositional analysis: although impact ionization MS is sensitive, it may chemically destroy the very organic signatures we wish to detect.

In this context, studying organic polymer analogues such as polypyrrole(PPy) or polyaniline (PANi)-coated polystyrene particles provides a valuable proxy for understanding the degradation and survival of organic matter under impact conditions (e.g., Burchell et al., 1999). Their well-defined chemical structure makes them ideal for tracing the evolution of carbonaceous and heteroatomic fragments, directly relevant to organic matter in cometary and asteroidal dust. Early

experimental studies using electrostatic accelerators have greatly contributed to our understanding of impact-induced ionization. Burchell et al. (1999, 2002) demonstrated that organic microparticles coated by a conducting polymer (< 1μm diameter) can be efficiently charged and accelerated to velocities up to 38 km s^{-1} using the 2 MV Van de Graaff accelerator of the University of Kent at Canterbury. Subsequent work by Kissel and Krueger (2001) and Goldsworthy et al. (2002; 2003) expanded these findings by analyzing the time-of-flight (TOF) mass spectra of plasmas produced by hypervelocity impacts. Kissel and Krueger (2001) projected polystyrene microspheres coated with PEDOT %polyethylene-dioxythiophene) onto a silver target at the speeds of 6±16 km s-1 and revealed that the ions produced from organic matter impacting at high speeds are indeed not specific for their detailed structure. Goldsworthy et al. (2002; 2003) projected metal (iron), organic (polypyrrole and polystyrene latex) and mineral (aluminosilicate clay) microparticles onto rhodium targets. In these studies, the TOF spectra displayed complex fragmentation patterns with periodicities of 12–14 amu, reflecting extensive molecular breakdown and recombination.

A key benchmark in this field is the study by Srama et al. (2009), who used a Van de Graaff electrostatic accelerator to launch submicrometer PPy- or PANi-coated polystyrene particles at velocities up to 12 km s^{-1}. Their time-of-flight mass spectra showed a strong velocity dependence. Although the method provides powerful compositional diagnostics, the molecular identity of the projectiles is progressively lost as impact velocity increases. Burchell and Armes (2011) extended this approach using poly(methyl methacrylate) (PMMA) latex microparticles, which are chemically more labile than polystyrene. They accelerated to 4–8 km s^{-1} and demonstrated that the loss of molecular identity occurred at even lower velocities. More recently, Mikula et al. (2023) investigated chemically stable, aromatic-rich anthracene projectiles over a velocity range of 2–35 km s^{-1} and showed that hypervelocity impacts above ~10 km s^{-1} led to extensive structural destruction of anthracene and the formation of hydrocarbon clusters. These past studies all highlight a fundamental

limitation of direct plasma-based hypervelocity impact MS; it becomes increasingly and often irreversibly chemically destructive once the impact speed exceeds approximately 10 km s^{-1}.

To overcome this limitation, we propose a complementary strategy that focuses on neutral gas-phase products rather than the ionized plasma. Specifically, we reproduce the vaporization process of hypervelocity impacts by pulsed-laser ablation of solid polystyrene and subsequently analyze the generated vapor using electron-impact mass spectrometry (EI-MS). This approach enables us to isolate and analyze the post-vaporization gas, providing insights into whether characteristic molecular structures can be retained more effectively compared with direct plasma MS. By comparing the resulting spectra with the benchmark data of Srama et al. (2009), we aim to identify similarities and differences in fragmentation pathways between impact-induced plasma and laser-generated vapor, and evaluate the feasibility of gas-phase MS observation as a softer and chemically conservative analytical method for spaceborne dust analyzers.

This chapter hereafter demonstrates, through laboratory laser-ablation experiments, that MS analysis of neutral gas can serve as a gentler analogue of hypervelocity impact phenomena since it preserves more of the original molecular information than plasma-based methods.

4.2 Experimental Methods

4.2.1 Overview of the Previous Studies: Hypervelocity Impact Mass Spectrometry of Polystyrene

The seminal studies by Srama et al. (2009) following Goldsworthy et al., (2003) revealed a distinct velocity-dependent transition in fragmentation behavior, summarized as follows.

In the ~5 km s⁻¹ regime, shown in Figure 4-1, the mass spectrum exhibits intact styrene-related fragments together with a large number of lower-mass fragments. The most prominent peaks appear at m/z = 91 and 77 (shown in Figure 4-2), corresponding to the benzyl/tropylium cation and the phenyl cation, respectively. This pattern indicates that the aromatic ring structure can partially survive moderate shock energy, while substantial fragmentation of the polymer backbone simultaneously occurs.

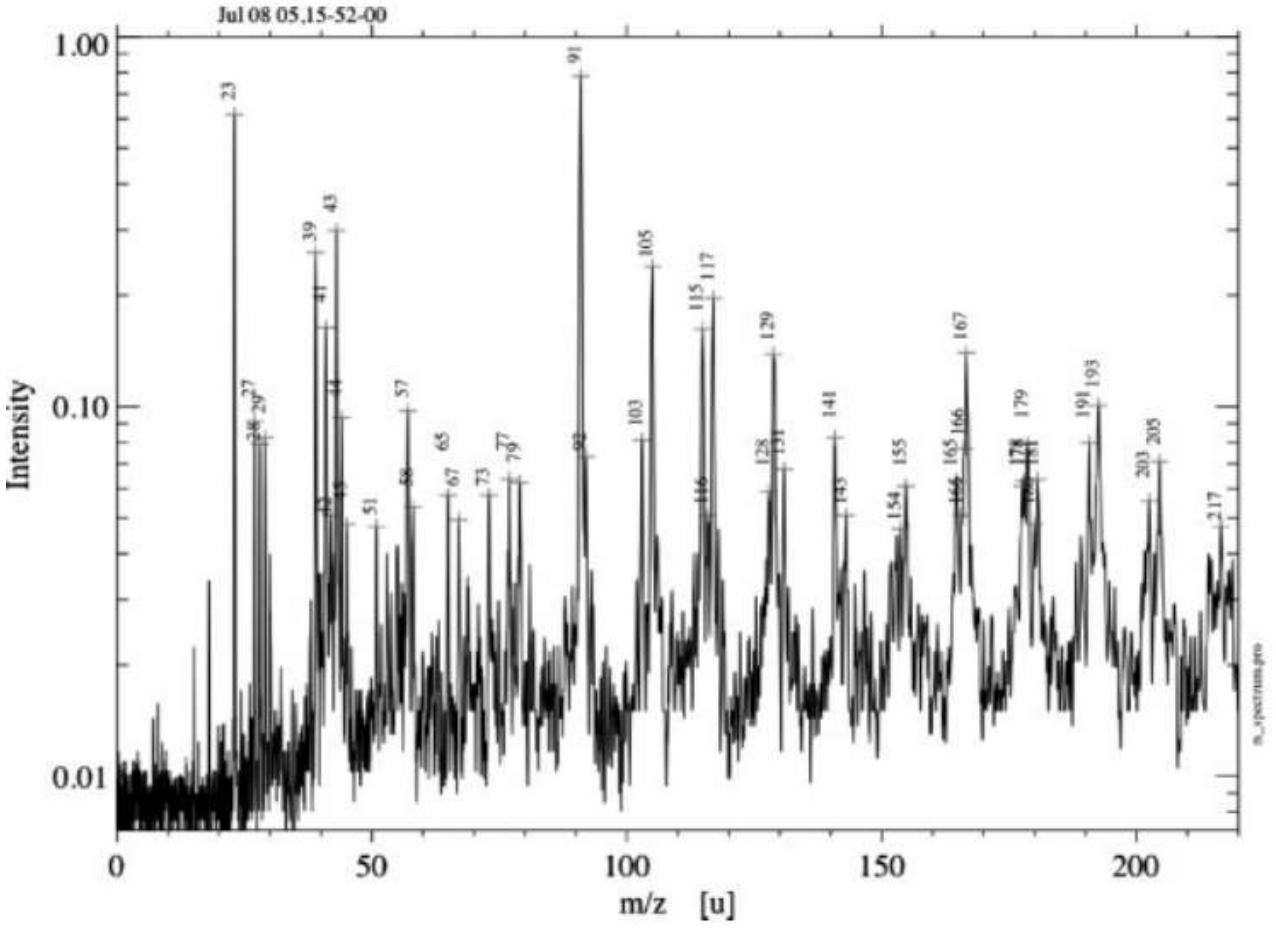

Figure 4-1. Cation spectrum obtained for a 1.81 μm diameter PPy-PS latex at a low impact velocity of approximately 5 km s^{-1}. Adapted from Srama et al. (2009).

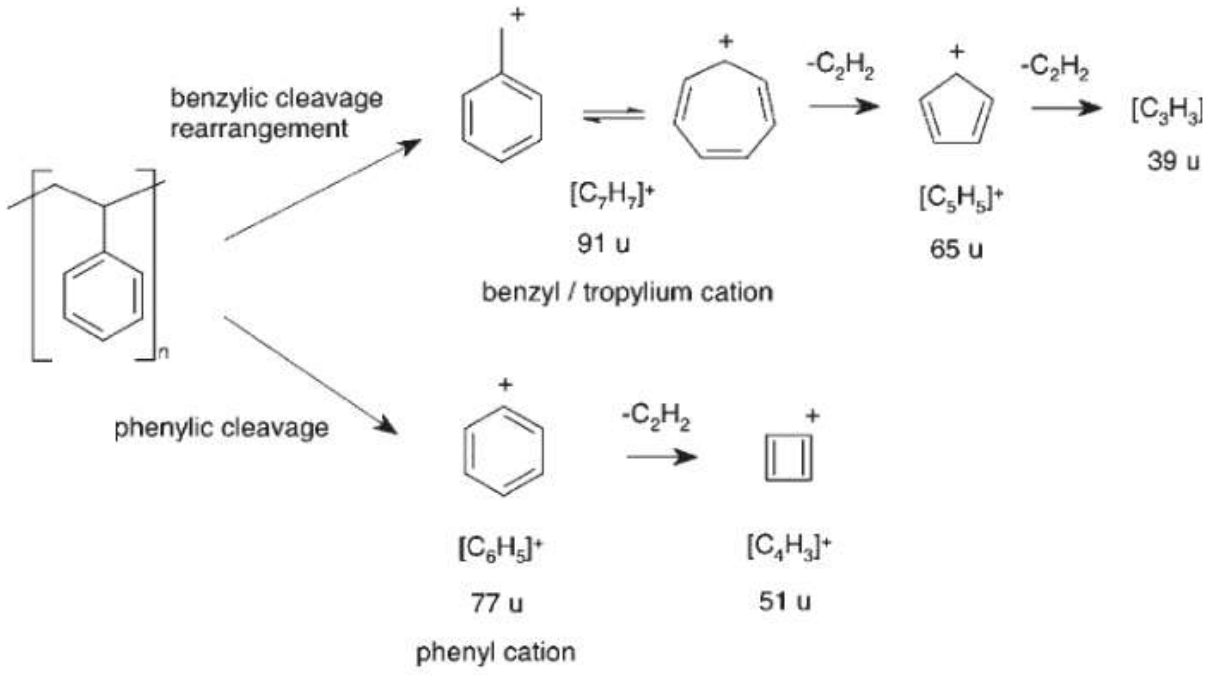

Figure 4-2. Primary fragmentation pathways of polystyrene leading to the formation of characteristic aromatic ions during energetic dissociation. Adapted from Srama et al. (2009).

At ~8 km s^{-1}, shown in Figure 4-3, the spectral characteristics change markedly. The peaks at m/z = 91 and 77 become strongly dominant, while most other fragments vanish. This behavior reflects a selective survival of stabilized aromatic cations, suggesting that shock-driven vaporization at this velocity regime favors robust ring-stabilized structures and suppresses formation of less stable molecular fragments.

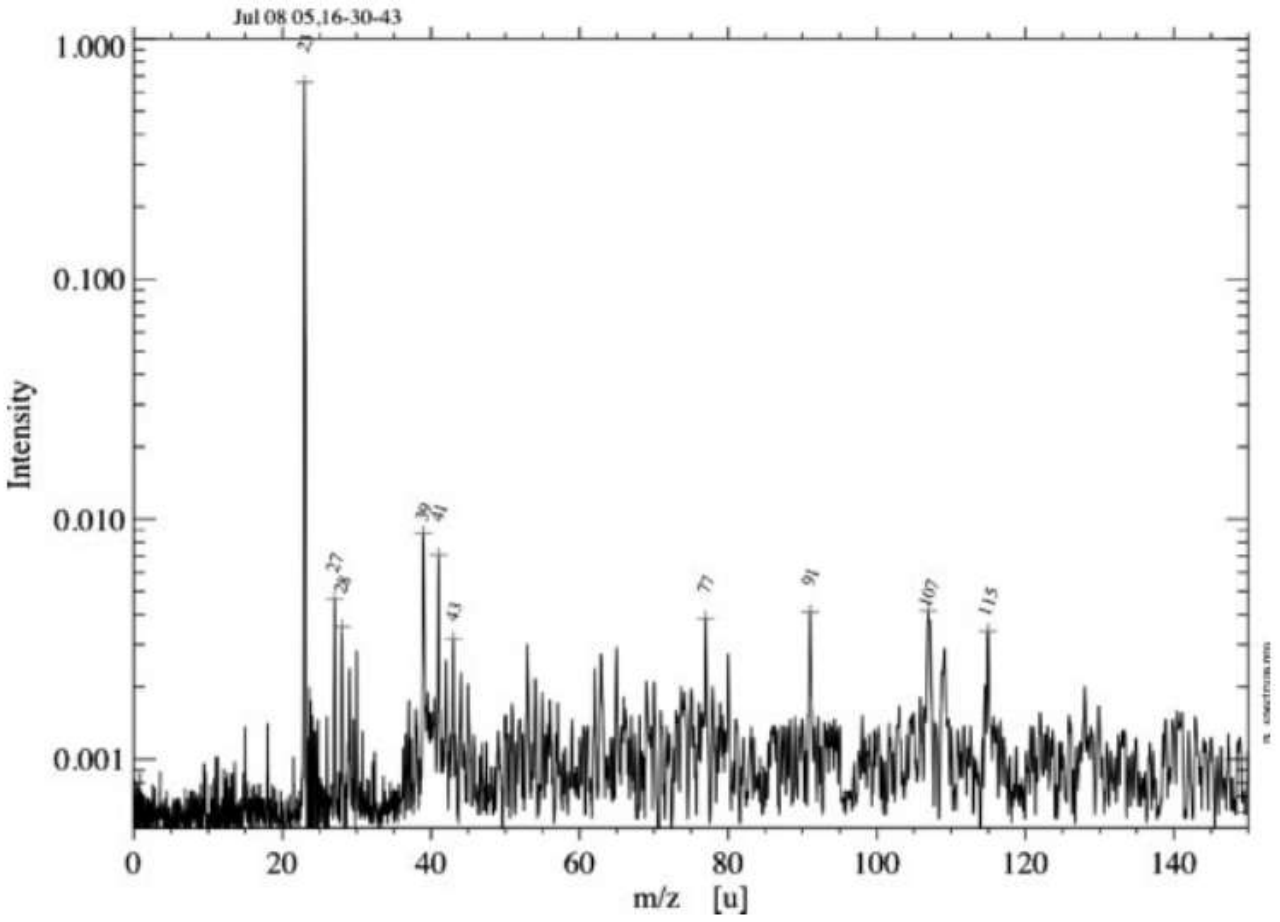

Figure 4-3. Cation spectrum obtained for a 0.76 μm diameter PANi-PS latex at an impact velocity of 8 km s^{-1}. Adapted from Srama et al. (2009).

Above ~12 km s^{-1}, shown in Figure 4-4, even the m/z = 91 ion begins to degrade, and the spectrum becomes dominated by hydrogenated carbon cluster ions ($C_nH_m^+$). At these extreme velocities, severe shock chemistry takes place, leading to extensive molecular degradation. The original molecular identity of the polymer is largely lost due to high-temperature plasma formation, rapid ion–electron recombination, and carbonization processes in the expanding impact plume. These results show that polystyrene retains identifiable molecular signatures only below ~10 km s^{-1}, beyond which aromatic ions fragment and complex carbon clusters dominate.

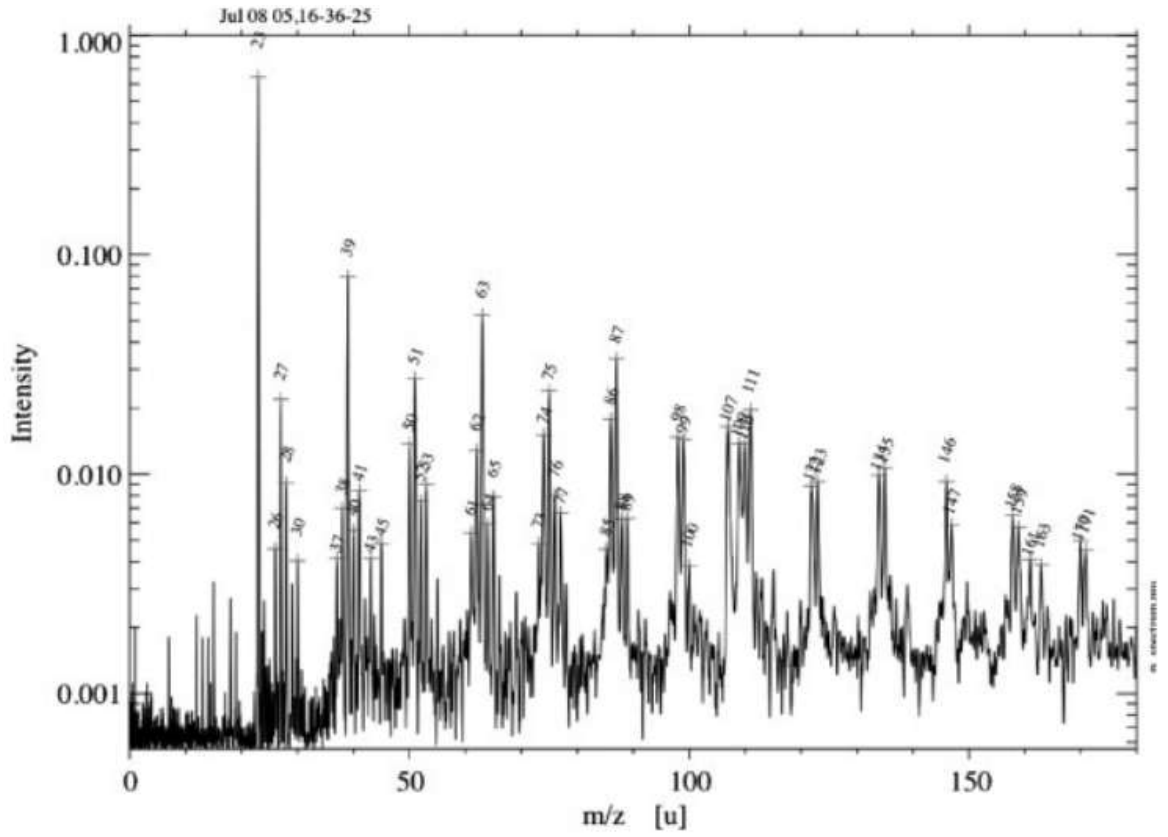

Figure 4-4. Cation spectrum obtained for a 0.70 μm PANi-PS latex at an impact velocity of 12 km s^{-1}. Adapted from Srama et al. (2009).

4.2.2 Experimental System Configuration

Our experiments were conducted using a vacuum chamber installed at the Institute of Laser Engineering, the University of Osaka. The overall system configuration is illustrated in Figures 4-5 and 4-6. The candidate designed, constructed, and operated the experimental apparatus, described in detail in the following section.

The vacuum chamber consisted of two cylindrical stainless-steel units such as a large chamber (φ15 cm × 30 cm) and a small chamber (φ10 cm × 25 cm). A two-stage pumping system combined a turbo molecular pump (TMP) and a rotary pump (RP) and achieved a base pressure of 1 × 10^{-4} Pa. During laser irradiation, transient gas release caused the chamber pressure to rise to 1 ×

10^{-2} Pa. By controlled leakage through a valve into the analytical chamber, stable gas analysis was maintained throughout the experiment. The quadrupole mass spectrometer (QMS) used was a Canon Anelva QMA-201, operated with a secondary electron multiplier (SEM) voltage of 2.5 kV and a gain of 10^4. The laser source was a Nd:YAG laser with wavelength = 532 nm, pulse width = 5.4 ns, and the maximum energy = 900 mJ. The spot diameter was approximately 20 μm, enabling localized surface heating and instantaneous evaporation of the sample.

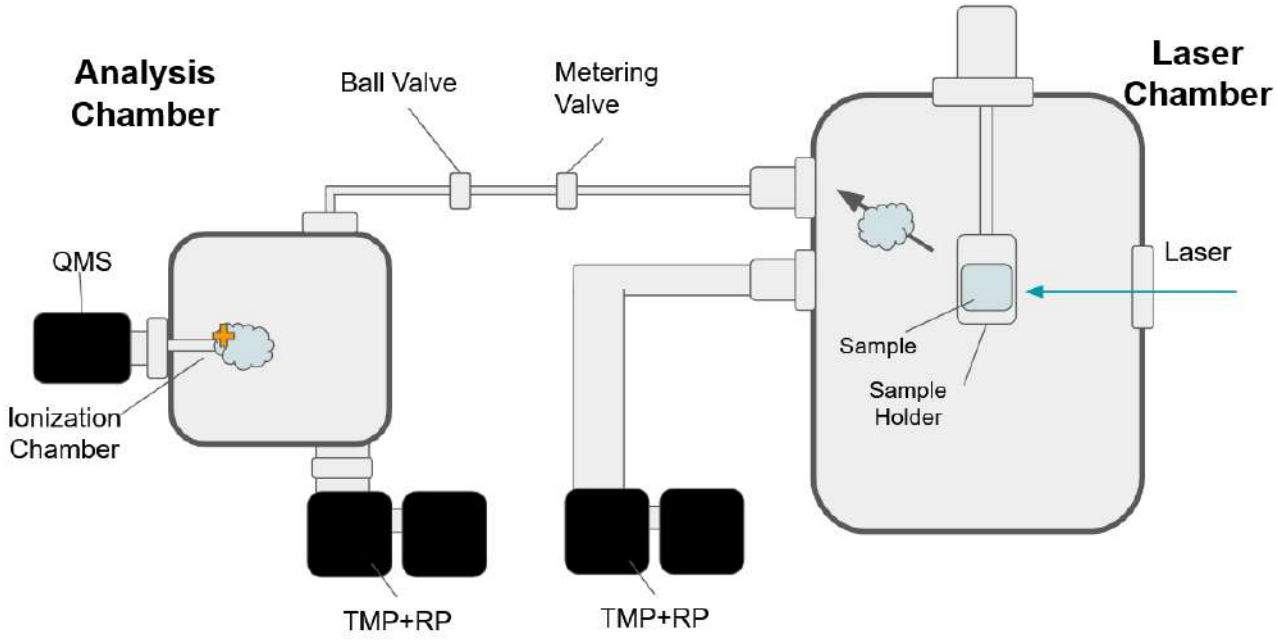

Figure 4-5. Configuration of the Experimental System

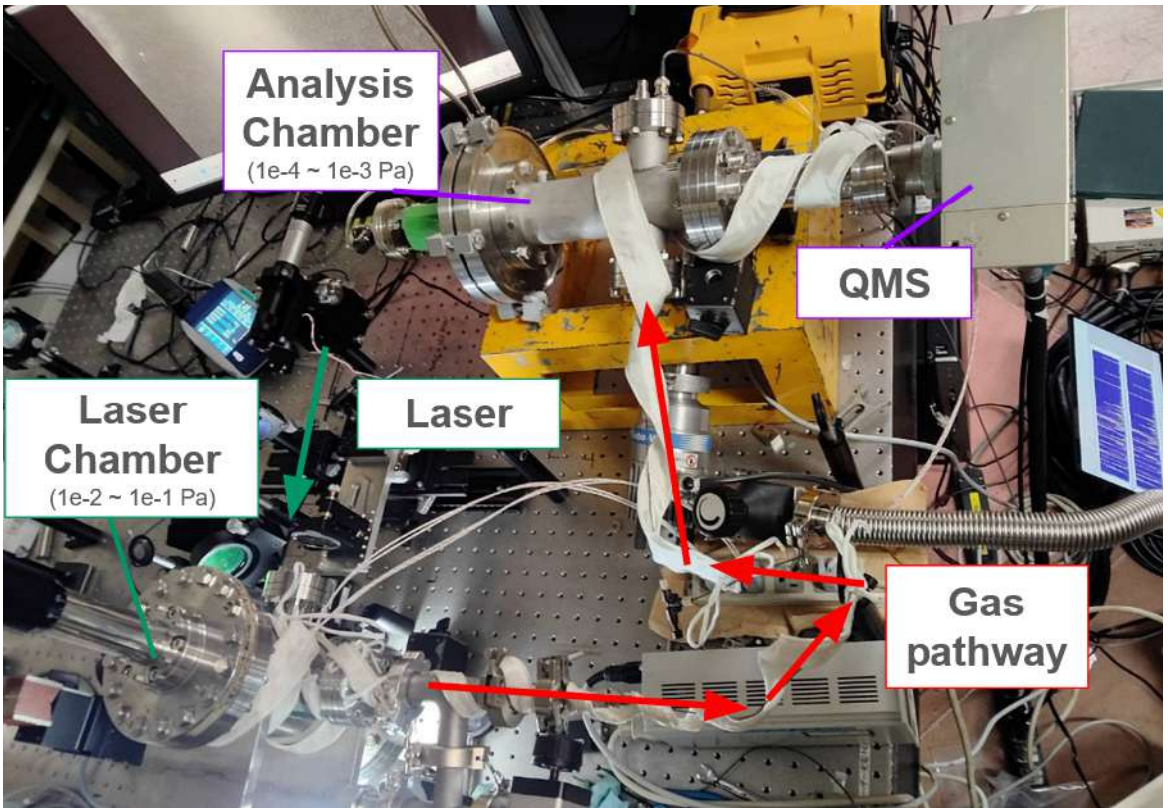

Figure 4-6. Photograph of the experimental arrangement.

4.2.3 Laser condition

In this study, we aim to obtain electron-impact (EI) mass spectra of impact-generated gas that can be directly compared with the impact ionization mass spectra reported by Srama et al. (2009). To this end, we estimate the laser intensity required in our laboratory experiments by means of P4P simulations.

For polystyrene, $(C_8H_8)_n$, the effective atomic number and atomic mass were evaluated as the mean values of the constituent atoms, following the same procedure used in Chapter 3 to convert water molecules into monoatomic species. Specifically, the effective atomic number and atomic mass are given by

$$\bar{Z} = 3.5 = (6 \times 8 \times n + 1 \times 8 \times n) / \{(8 + 8) \times n\} \quad (4\text{-}1),$$

$$\bar{A} = 6.5 = (12 \times 8 \times n + 1 \times 8 \times n) / \{(8 + 8) \times n\} \quad (4\text{-}2),$$

respectively. For consistency with the water calculations, the outer-shell potential in the ion-sphere model was set to −17.3 eV, corresponding to the binding energy of the C 2s orbital, based on X-ray photoelectron spectroscopy (XPS) data (Crist, 2018).

For the post-processing analysis, we adopted the same methodology as that employed in Chapter 3. There, we demonstrated that the charge-weighted average of the maximum ion temperature serves as a key indicator linking laser-irradiation-generated plasma mass spectra with those produced by hypervelocity impacts. In this study, we assume that the gas generated in the hypervelocity impact experiments of Srama et al. (2009) can be reproduced by laser irradiation if the mole-weighted average of the maximum gas thermal temperature is comparable in both cases.

In both the hypervelocity impact and laser irradiation simulations, the gas region was identified using Eq. (2–8), and the temporal evolution of the gas thermal temperature was tracked for each species. To achieve sufficiently high gas temperatures, laser irradiation simulations were conducted at significantly higher intensities than those employed in the LILBID experiments described in Chapter 3. Specifically, a laser intensity of 52.8 TW cm^{-2} was used, which is achievable with the Nd:YAG laser in our experimental apparatus. Unlike the LILBID experiments, the present analysis does not involve selection by delay time. Instead, ion and gas temperatures were averaged over the entire spatial domain. The detailed simulation parameters are provided in Appendix C.

Figures 4-7(a) and (b) show the temporal evolution of gas thermal temperatures obtained from the P4P simulations for hypervelocity impacts, in which 0.7- and 0.76-μm-diameter polystyrene particles collided with a rhodium target at velocities of 12.0 and 8.0 km s^{-1}, respectively (Srama et al., 2009). Under these conditions, the mole-weighted average of the maximum gas thermal temperature was found to be 1.66 eV for the 12.0 km s^{-1} impact and 0.99 eV for the 8.0 km s^{-1} impact. As shown in Fig. 4-7(c), the laser irradiation simulation at 52.8 TW cm^{-2} yielded a corresponding value of 1.22 eV. Recall that we identified a systematic offset of approximately +0.1

eV in the average maximum gas thermal temperature obtained from hypervelocity impact simulations relative to laser irradiation simulations in Section 3.4 (Table 3-3). Accounting for this offset, the laser-induced gas temperature closely matches with those produced by impacts at 12.0 and 8.0 km s^{-1}.

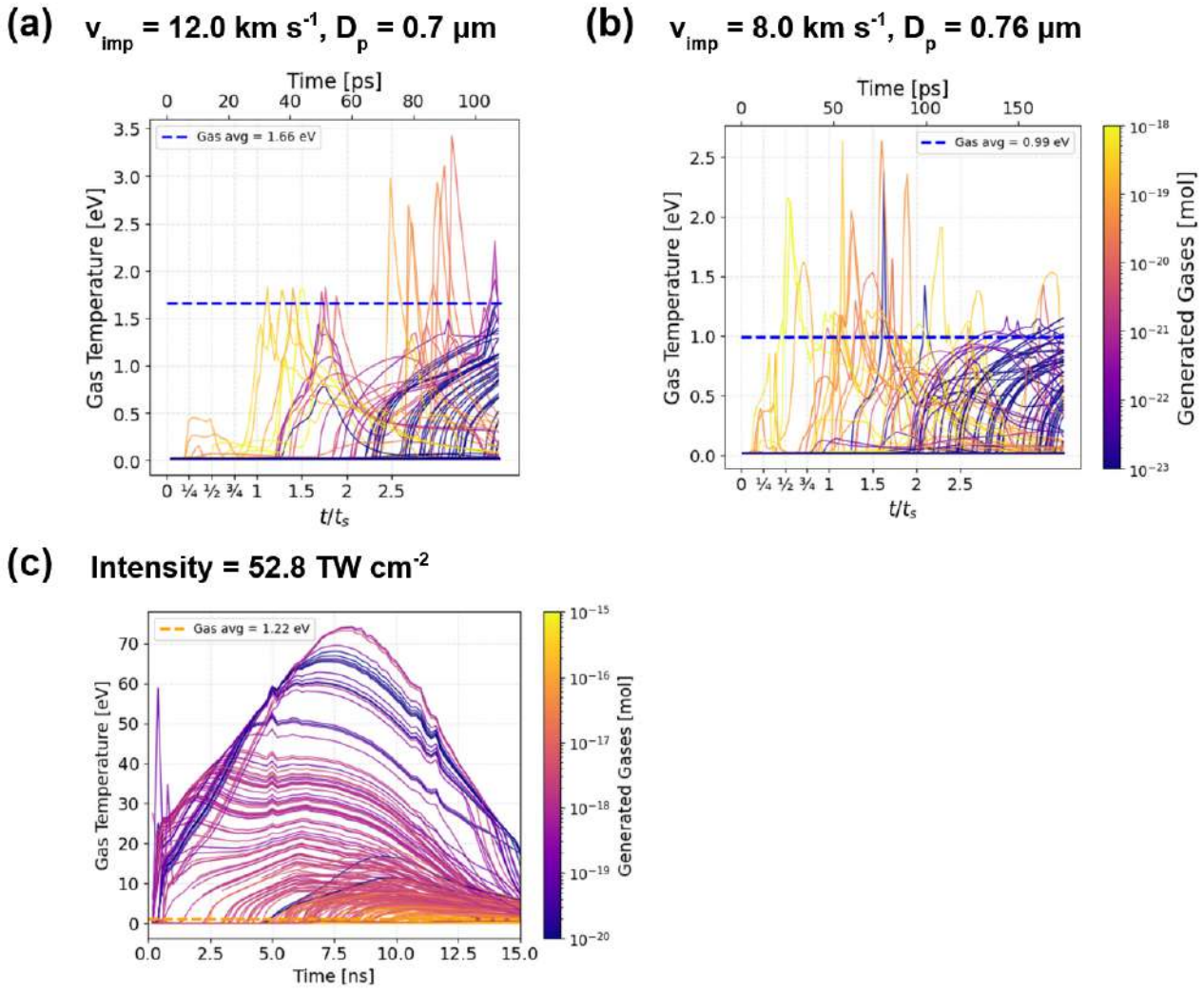

Figure 4-7. The comparison of the time evolution of the thermal gas temperature for individual gas species obtained from P4P simulations. The panels (a) and (b) are for hypervelocity impacts under an impact velocity of 12.0 and 8.0 km s^{-1}, while the panel (c) is for a laser ablation under a laser intensity of 52.8 TW cm^{-2}. The dotted horizontal lines in the Figures indicate the mol-weighted average of the maximum ion temperature experienced by each gas. The color bars represent the amount of the generated gases, and the color scale of the panels (a) and (b) is the same.

In Figures 4-7(a) and (b), the maximum gas temperature is approximately 3 eV, whereas in Figure 4-7 (c) it reaches values of up to ~70 eV. This difference arises despite the similarity in the average maximum gas temperatures. During laser irradiation, the deposited energy follows a Gaussian spatial profile, leading to intense electron heating near the focal center and comparatively cooler gas in the lower-fluence peripheral regions. In contrast, during hypervelocity impacts, energy deposition occurs primarily at the contact interface and is transported outward through thermal processes, resulting in a smaller spatial energy gradient and a narrower temperature distribution.

Figure 4-8 compares the distributions of the maximum gas thermal energy for the hypervelocity impact and laser irradiation cases. The impact simulations exhibit energy distributions confined to a relatively narrow range of 0–15 eV, whereas the laser irradiation case spans a much broader range of 0–80 eV. In particular, the high-energy tail observed in the laser case contains a substantial population of ions, indicating strong ionization near the laser focal center at intensities on the order of TW cm^{-2}. Nevertheless, in both cases, approximately 95 % of the gaseous species reside below 1 eV, demonstrating that the mole-weighted average gas temperature is dominated by these low-energy components.

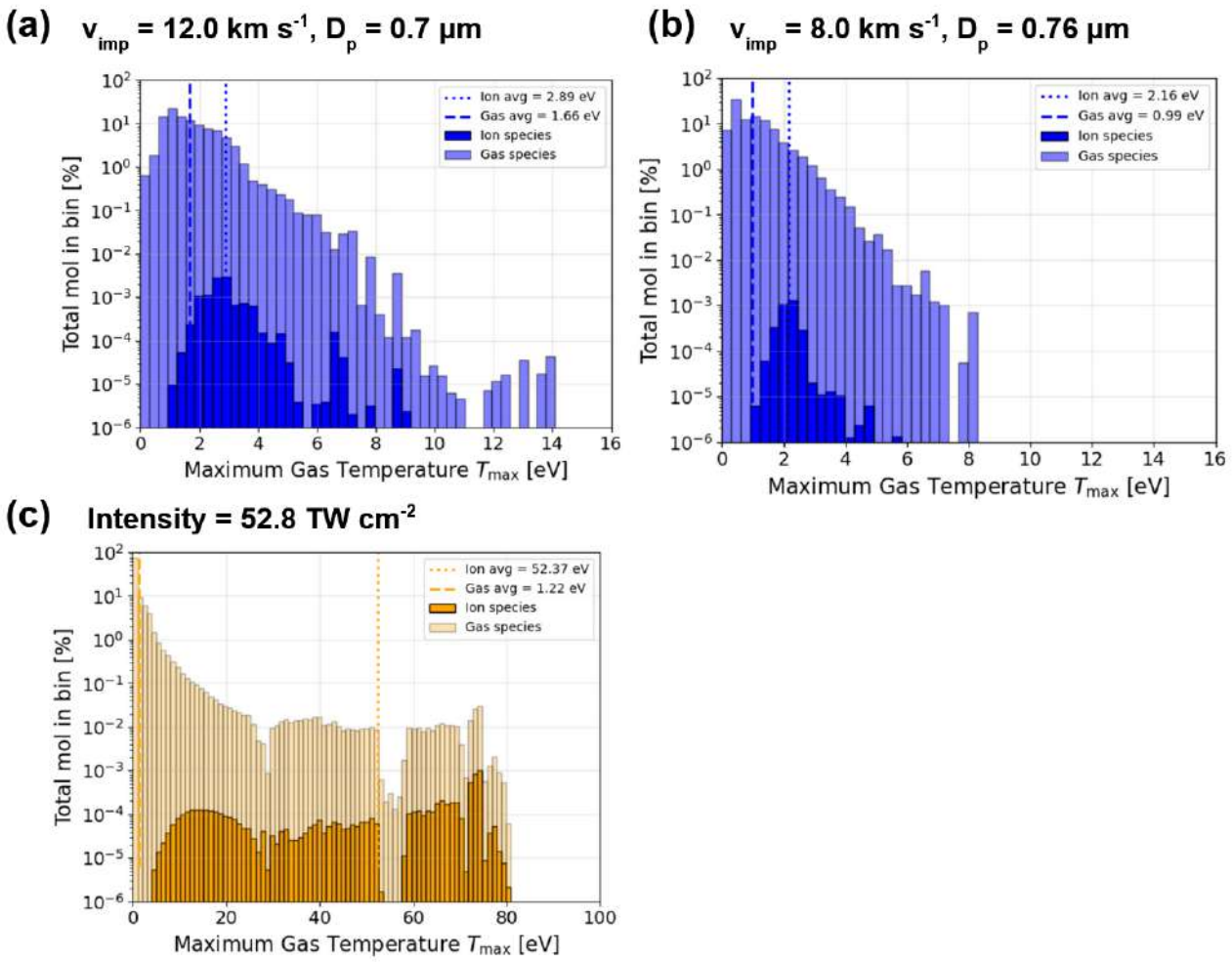

Figure 4-8. The comparison of the energy distribution of the maximum thermal gas temperature obtained from the P4P simulations. The panels (a) and (b) are for hypervelocity impacts under an impact velocity of 12.0 and 8.0 km s^{-1}, respectively, while the panel (c) is for a laser ablation under a laser intensity of 52.8 TW cm^{-2}. The dotted vertical lines in (a) and (b) indicate the mol-weighted average of the maximum thermal ion and gas temperature.

These results demonstrate that laser irradiation at an intensity of 52.8 TW cm^{-2} can successfully reproduce the maximum gas thermal temperatures generated by hypervelocity impacts across the velocity range of 8.0–12.0 km s^{-1}, as reported by Srama et al. (2009). In the subsequent experiments, laser shots at 7.3 TW cm^{-2} and 2.4 TW cm^{-2} were also conducted for comparison, and

the resulting neutral gases were analyzed using electron-impact ionization mass spectrometry (EI-MS).

4.2.4 Experimental Apparatus and Methods

As the organic target material, polystyrene film of ~25 μm thickness was used. The commercially available polystyrene film was first fragmented and dissolved in o-xylene. With the resulting solution, another polystyrene film was glued onto a tantalum (Ta) plate and air-dried, forming a thin polystyrene membrane. After drying, the film became thin enough to exhibit transparent and uniform optical reflection properties. The sample was mounted on a sample holder inside the vacuum chamber, and the laser incidence angle was precisely adjusted to be normal to the surface. Since ablation-induced gas emission occurred instantaneously upon irradiation, the gas transfer path was minimized to allow immediate introduction of ablated gas into the QMS for real-time analysis.

Because each laser pulse caused a localized pressure rise, both the pumping speed and gas introduction rate were actively controlled. The initial vacuum is $\sim 1 \times 10^{-2}$ Pa, and the pressure get higher approximately 2×10^{-1} Pa by one laser irradiation. After 10 consecutive pulses, the vacuum had reached at $\sim 1 \times 10^{0}$ Pa (Figure 4-9, a). The photograph of the surface of the polystyrene film is shown in Figure 4-9 (a), which also indicates sufficient fracture and vaporization of the material had occurred.

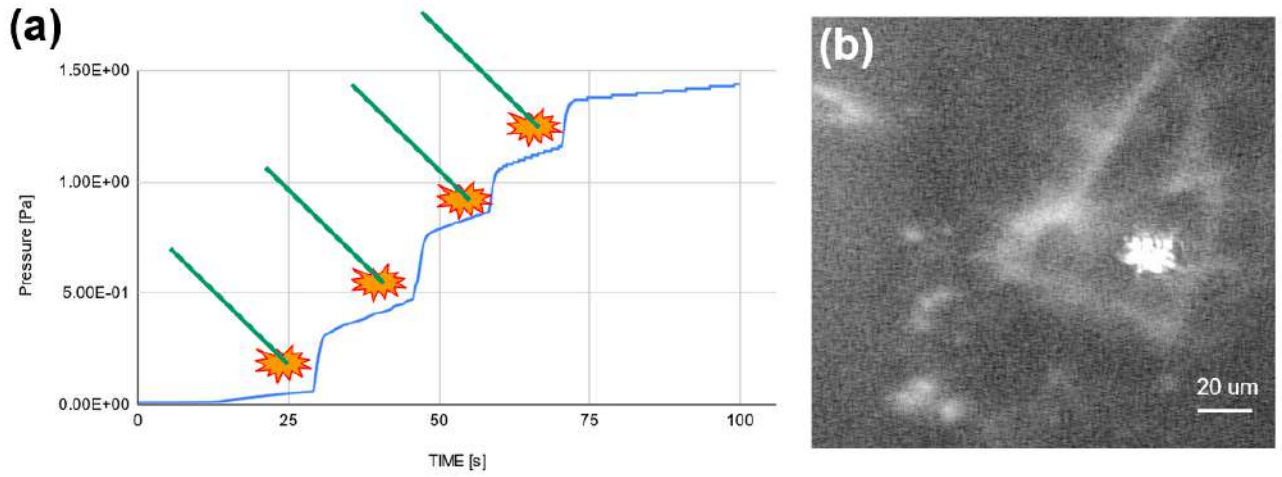

Figure 4-9. (a) Temporal evolution of chamber pressure during repeated laser shots. (b) Optical micrograph of the polystyrene film after laser irradiation (pulse energy: 900 mJ, pulse width: 5.4 ns, wavelength: 532 nm, spot diameter: ~20 μm). We can see a central hole in the polystyrene exposing the underlying Ta substrate while the bright ellipse slightly to the right marks the laser aiming.

The gas generated by laser ablation was leaked into the analytical chamber (EI/PI zone) through a metering valve, and then the vacuum of the analytical chamber was reached at 3 x 10^{-3} Pa. This process enabled in-situ ionization and mass spectrometric analysis of the organic components produced by laser ablation.

4.3 Results

In the lower m/z region, hydrocarbon fragment peaks centered at m/z = 29, 43, 57, 71, and 85 are observed as they increase systematically with laser pulse energy. These peaks correspond to typical linear alkyl carbenium ion series associated with the thermal decomposition of polymer backbones. During polystyrene pyrolysis, chain-end hydrogen abstraction and stepwise loss of C2 units have been reported (Faravelli et al., 1999; 2001; 2003; Achilias et al., 2007; Nisar et al., 2019; Sikes et al., 2021), and the resulting small hydrocarbon radicals can thermally recombine to form stable

carbenium ions. In particular, the peaks at m/z = 43, 57, 71, and 85 are characteristic of linear alkyl-derived fragments, and their increasing intensities at higher pulse energies likely reflect enhanced C2 production and subsequent recombination under elevated thermal load. This interpretation is consistent with Srama et al. (2009), who also identified peaks at m/z = 29, 43, and 57 as carbenium ions derived from the aliphatic backbone of polystyrene. These fragments have been reported to appear in impacts up to 5 km s^{-1} in Srama et al. (2009). This observation strongly indicates that the energy level of the gas phase produced by laser irradiation in the present experiment is lower than that of the ions generated during 5 km s^{-1} hypervelocity impacts.

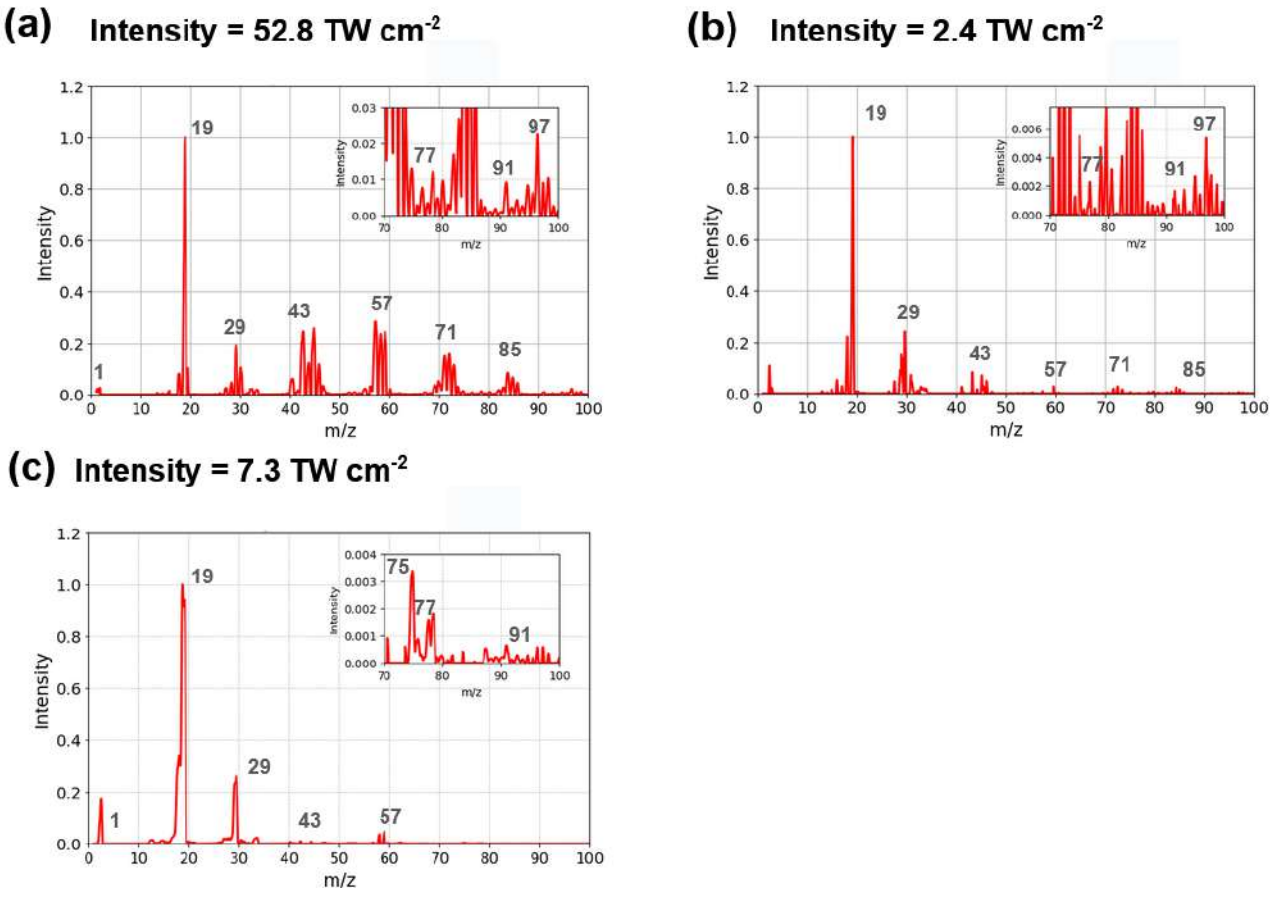

Figure 4-10. QMS mass spectra obtained after single laser shots on the polystyrene target at different laser pulse energies: (a) 52.8 TW cm^{-2}, (b) 7.3 TW cm^{-2}, and (c) 2.4 TW cm^{-2}. All spectra are shown over the 0–100 amu range, where characteristic hydrocarbon fragment series originating from the polystyrene polymer are observed. The intensity is normalized by the intensity of m/z = 19 (H_3O^+).

Conversely, the phenyl cation at m/z = 77 and the benzyl/tropylium cation at m/z = 91, reported as a dominant styrene signature in hypervelocity impact experiments (Srama et al., 2009), were detected at any laser energy in this study. Because the benzyl/tropylium fragment at m/z = 91 cannot be observed by electron impact, this pattern implies that these fragments are generated by the laser ablation. However, the intensities were not strong compared to those of the typical linear alkyl carbenium ion series. Additionally, peaks at m/z = 97 are present, especially in 52.8 TW cm^{-2} and 7.3 TW cm^{-2} mJ shots. These are plausibly assigned to $C_7H_{13}^+$, hydrogenated derivatives of the benzyl/tropylium cation at m/z = 91 formed via H pickup in the hot, H-rich ablation plume, consistent with cyclohexenyl cations. Such assignments are physically reasonable for the EI of laser-generated vapor, but they are not commonly emphasized in prior thermal decomposition studies of polystyrene (Sikes et al., 2021), suggesting a distinct recombination pathway under our experimental conditions.

In the high-mass region, the styrene monomer signal at m/z = 104 is observed at all pulse energies, confirming that neutral styrene is indeed volatilized by the laser and subsequently ionized in the EI source. More strikingly, pronounced peaks at m/z = 143, 160, and 182 appear systematically; these features were not reported in the hypervelocity impact spectra of Srama et al. (2009) and therefore represent a key difference. If the signals originated from a generic distribution of hydrogenated carbon clusters, one would expect a smooth, monotonic decrease of intensity with increasing m/z. Instead, the discrete, high-contrast peaks at 143, 160, and 182 indicate formation of specific, preferential recombination products or fragments of styrene oligomer.

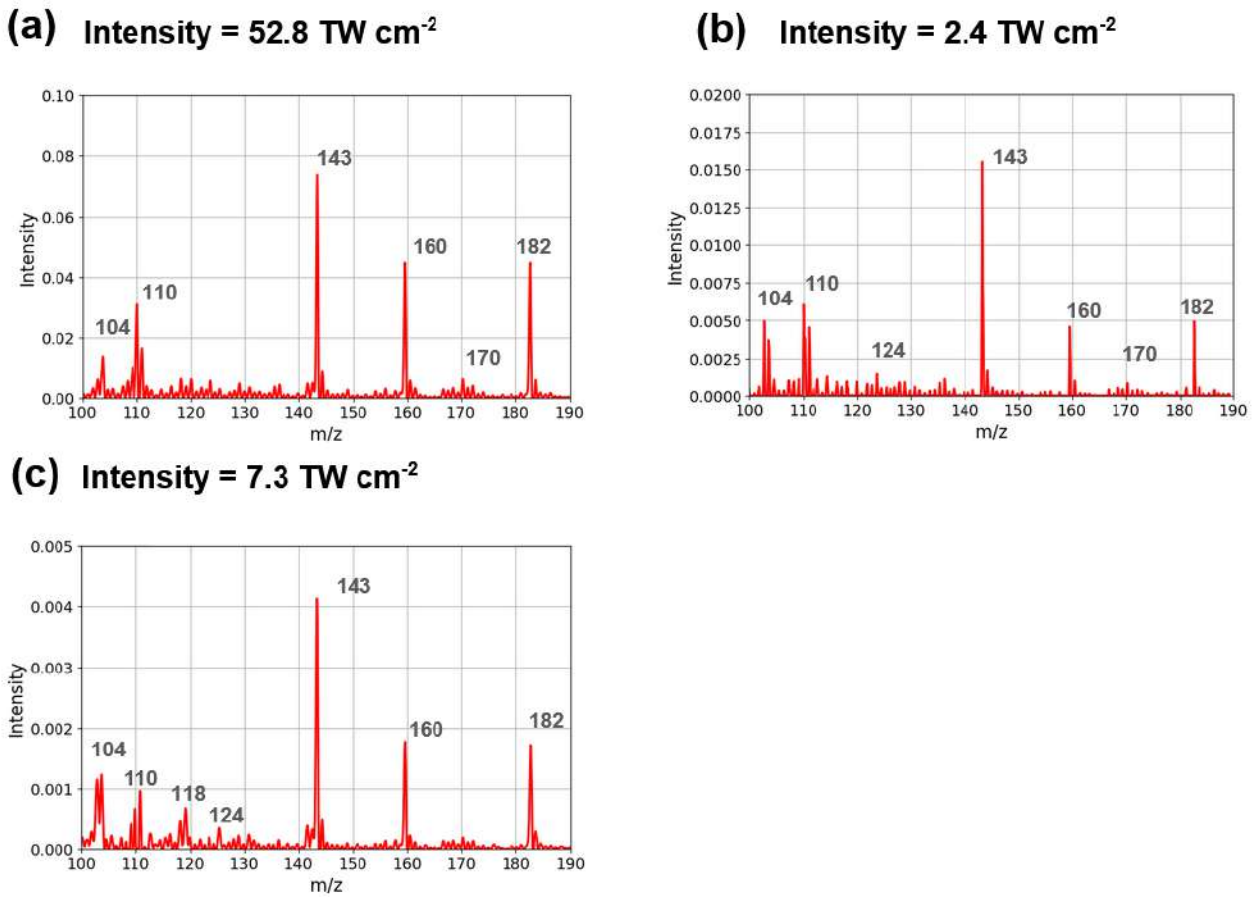

Figure 4-11. QMS mass spectra in the 100–190 amu range obtained after single laser shots on the polystyrene target at pulse energies of (a) 52.8 TW cm^{-2}, (b) 7.3 TW cm^{-2}, and (c) 2.4 TW cm^{-2}. Multiple high-mass hydrocarbon ion peaks (e.g., m/z = 104, 110, 143, 160, and 182) are observed, representing characteristic fragment series of polystyrene. The intensity is normalized by the intensity of m/z = 19 (H_3O^+).

Additionally, peaks at m/z = 110 are consistently observed at all laser energies. These ions can be plausibly assigned to $C_8H_{14}^+$, i.e., hydrogenated derivatives of styrene formed via H-addition processes, similar to the species at m/z = 97. Notably, the m/z = 110 signal increases with laser energy, while the styrene monomer peak at m/z = 104 decreases. This inverse correlation suggests that higher laser fluences promote hydrogenation of the aromatic ring in styrene, likely due to increased availability of reactive H-atoms in the hot plume and enhanced recombination kinetics.

4.4 Discussion

The discrete, high-contrast peaks observed at m/z = 143, 160, and 182 have not been reported in previous studies of styrene thermal decomposition (Faravelli et al., 2001; Achilias et al., 2007; Nisar et al., 2019; Sikes et al., 2021) or in prior laser-ablation studies of PAHs (Haefliger and Zenobi, 1998; Fukumura et al., 1993; Spencer et al., 2008). In contrast, Alsharaeh and El-Shall (2011), who investigated fragmentation of styrene oligomers following electron ionization and subsequent high-velocity collisions with helium—reported m/z = 143 and 180 as characteristic fragments of styrene trimers and dimers. In their study, the most abundant trimer isomer (T-1) undergoes aromatic-ring cleavage to form the dimer D-1, followed by ethylene loss to produce an intermediate at m/z = 180. In this experiment, the laser-plume environment appears to be strongly reducing (H-rich), as indicated by the formation of hydrogenated phenyl-based fragments. The canonical aromatic fragments at m/z = 91 ($C_7H_7^+$) and m/z = 104 ($C_8H_8^+$) are accompanied by hydrogenated counterparts at m/z = 97 ($C_7H_9^+$) and m/z = 110 ($C_8H_{10}^+$). The increase in H/C ratio indicates that the π-bonded (unsaturated) carbon framework becomes hydrogenated, implying a highly reducing chemical environment in the laser plume. Under such conditions, the intermediate at m/z = 180 could reasonably undergo hydrogen addition to yield m/z = 182 (1,2-diphenylethane). Similarly, the second most abundant trimer isomer (T-2) can undergo benzyl-group loss to generate an intermediate at m/z = 221, followed by aromatic-ring loss to form m/z = 143 (2-phenylpentane), as reported previously. Subsequent hydrogen addition to this fragment would plausibly yield m/z = 160 (3-phenyl-2-hexene). Notably, such fragments were not reported by Srama et al. (2009) in hypervelocity impact experiments at 8.0 - 12.0 km s^{-1}, indicating that the features at m/z = 143, 160, and 182 observed here likely originate from fragmentation of pre-existing styrene trimers, rather than from hypervelocity-induced aromatic condensation. However, although Alsharaeh and El-Shall (2011) predict that the D-1 dimer species can undergo aromatic-ring loss to yield a fragment at m/z = 130, no corresponding signal was observed in this experiment. This discrepancy may arise from

differences between the two experimental conditions, namely, electron-ionized styrene trimers accelerated into helium in Alsharaeh and El-Shall (2011) versus laser-generated fragments formed from condensed-phase polymer vaporization in this study. Nevertheless, the specific mechanism responsible for the absence of m/z = 130 remains unclear at this stage. A re-evaluation of the fragmentation and ring-loss pathways will be necessary in future work, including the possible suppression or alteration of this channel under high-temperature, hydrogen-rich plume conditions.

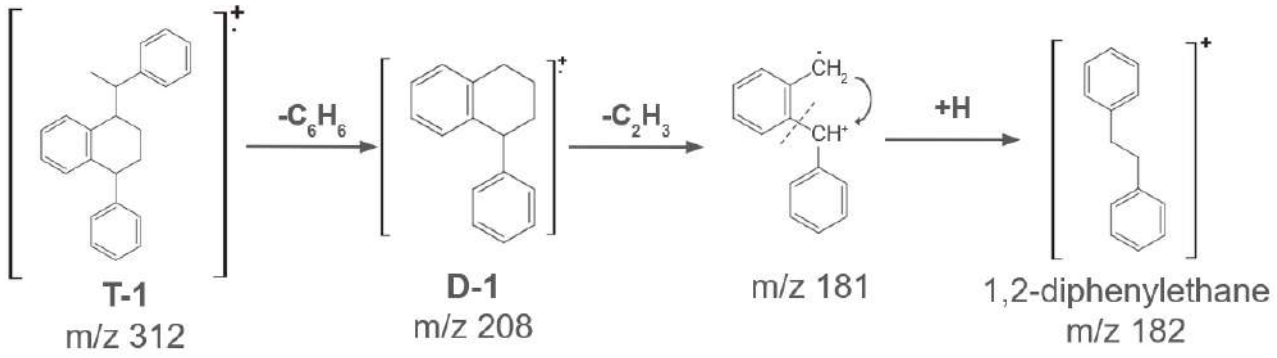

Figure 4-12. Fragmentation pathways of the styrene trimer ion $C_{24}H_{24}$ (T-1) and the styrene dimer ion $C_{16}H_{16}$ (D-1).

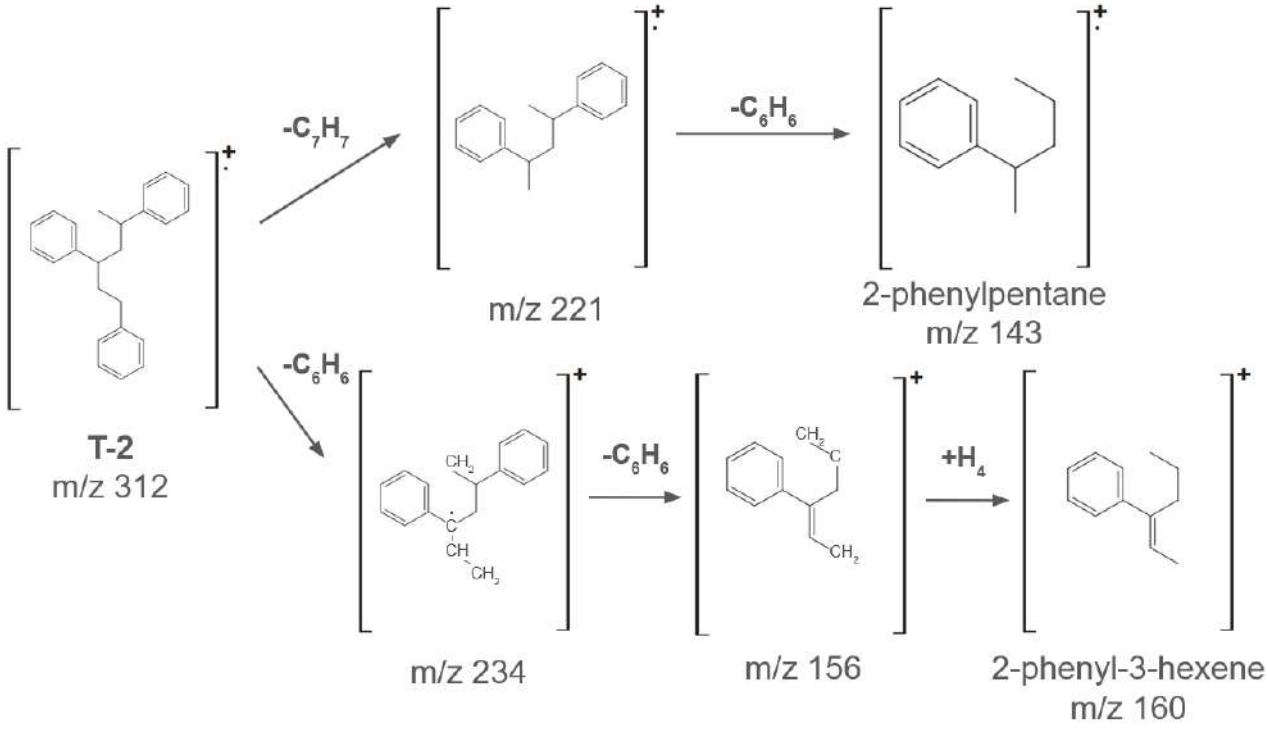

Figure 4-13. Fragmentation pathways of the styrene trimer ion $C_{24}H_{24}$ (T-2).

Unlike the CDA measurements in space or LILBID ground experiments, ions in this study are not sampled within microseconds after each impact, but they are transported through vacuum and detected after equilibration to near room temperature. While post-impact recombination cannot be fully excluded, Srama et al. (2009) showed that the impacts at 12.0 km s^{-1} destroy fundamental aromatic fragments (m/z = 77, 91), generating hydrogen-poor recombination products instead. Thus, the formation of intact styrene oligomers from vapor-phase carbon fragments appears unlikely in that regime. Moreover, the lifetime of the laser plume is on the order of nanoseconds and it rapidly expands and cools, sharply limiting the time window for large aromatic structures to reassemble. These findings strongly suggest that styrene oligomers of at least trimer size were already present in the gas-phase products generated by the molecular collisions, rather than being synthesized through post-fragmentation recombination.

This result provides compelling evidence that the gas-phase species produced during hypervelocity molecular impacts can retain more molecular integrity and, thus, be chemically softer than the plasma species generated under the same conditions. It further implies a survival pathway for larger aromatic structures under high-energy impact environments, with direct relevance to organic matter processing in space.

4.5 Future Work

Further investigation is required on the desorption pathways and the possible re-synthesis of styrene oligomers in the high-temperature gas phase, as discussed in the previous section. The mass spectra analyzed in this study correspond to samples that have undergone multiple processes: modification upon impact, chemical reactions during transport between chambers, and subsequent electron ionization. Therefore, the observed fragment ions might also originate from the electron

ionization process itself. To clarify this, future work should involve photoionization mass spectrometry (PI-MS) of the post-laser gas plume, which would allow the exclusion of fragmentation effects caused by electron ionization. This will enable a clearer understanding of the chemical evolution occurring during the gas transport stage following impact modification.

Through these steps, a more definitive discussion can be made on the importance of observing gas species at the moment of an impact of organic-bearing microparticles, providing stronger evidence for interpreting hypervelocity impact processes.

4.6 Summary

In this chapter, we experimentally investigated laser ablation of polystyrene as a controlled analogue of hypervelocity impacts, building directly on the radiation–hydrodynamics modelling framework developed in Chapter 3. Using the P4P code, we identified laser intensities (up to 52.8 TW cm^{-2}) that reproduce the characteristic temperatures of vaporized gas associated with a hypervelocity impact of polystyrene particles at 8 -12.0 km s^{-1}(Srama et al. 2009) can mimic the thermodynamic state of impact-sublimated gas. On this basis, we constructed a dedicated vacuum and QMS system to perform electron-impact ionization mass spectrometry (EI-MS) of laser-generated neutral vapor, enabling systematic comparison with benchmark hypervelocity impact spectra.

The EI-MS measurements reveal that laser-generated gas-phase products retain a richer set of molecular signatures than plasma-based hypervelocity impact MS. In the low-mass region, we observe systematic enhancement of linear alkyl carbenium ion series (m/z = 29, 43, 57, 71, 85) with increasing laser fluence, consistent with thermal decomposition and recombination of the polystyrene backbone at relatively moderate energies. These linear alkyl carbenium ions were not

observed in the impact spectra of polystyrene at 12.0 km s^{-1}, reported by Srama et al. (2009), but these were present at 5.0 km s^{-1}, indicating that the laser-analog conditions correspond more closely to the lower-energy impact regime in which partial molecular integrity is preserved.

In the higher-mass region, the persistent styrene monomer signal at m/z = 104 and the emergence of discrete, high-contrast peaks at m/z = 110, 143, 160, and 182 indicate the formation and survival of specific hydrogenated aromatic and oligomer-derived species, rather than a featureless continuum of carbon clusters. These features are not reported in the high-velocity impact spectra of Srama et al. (2009), where molecular identity is rapidly lost above ~10–12 km s^{-1}, and hydrogen-poor carbon clusters dominate. The contrast between these datasets demonstrates that analysis of neutral gas produced under laser-analog conditions can preserve more detailed molecular information than direct observation of impact-generated plasma.

These results provide experimental support for the central hypothesis of this chapter: laser-driven vaporization followed by MS analysis of neutral gas constitutes a chemically softer, more conservative diagnostic of impactor composition than conventional plasma-based hypervelocity impact MS. At the same time, the observed oligomer-related and hydrogenated fragments highlight the importance of plume chemistry, desorption pathways, and ionization mechanisms in shaping the detectable molecular inventory. These findings motivate the next step pursued in Chapter 5, where photoionization-based mass spectrometry is introduced as an even softer ionization technique to isolate the intrinsic composition of impact-generated gases, while minimizing EI-induced fragmentation, thereby advancing the design of future spaceborne, organic-bearing dust analysis instruments.

Chapter 5 Development and Fundamental Characterization of Photoionization Method

5.1 Advancing from Electron to Photoionization: A Softer Approach to Impact Gas Analysis

In the previous chapters, we have established the equivalence between laser ablation and hypervelocity impacts (Chapter 3) and demonstrated that gas-phase analysis via electron ionization (EI) can preserve molecular structures more effectively than direct plasma analysis (Chapter 4). This chapter explores the next step to assess the feasibility of replacing EI with photoionization (PI) for impact-generated gas analysis.

Traditional EI has been the standard ionization method in spacecraft-borne mass spectrometers, and it relies on high-energy electron collisions. While EI offers rich but fragmented information for molecular structure identification, it often causes excessive fragmentation, particularly for complex organic molecules and polymers, making it difficult to interpret their original structures. In the vicinity of planets and small bodies of the Solar System, where many molecular species can coexist, this over-fragmentation leads to spectral overlaps and reduced compositional accuracy. In contrast, PI offers a softer and more controllable ionization pathway. By tuning the photon energy to just above the ionization potential of target molecules, PI minimizes excess internal excitation and thus suppresses fragmentation. Previous laboratory studies (e.g., Arii et al., 2006) have shown that PI yields spectra dominated by intact molecular ions for organics, in stark contrast to the heavily fragmented spectra by EI (Figure 5-1) . Such gentle ionization characteristics make PI a promising candidate for high-precision organic analysis in future planetary missions, in which maintaining molecular integrity is essential.

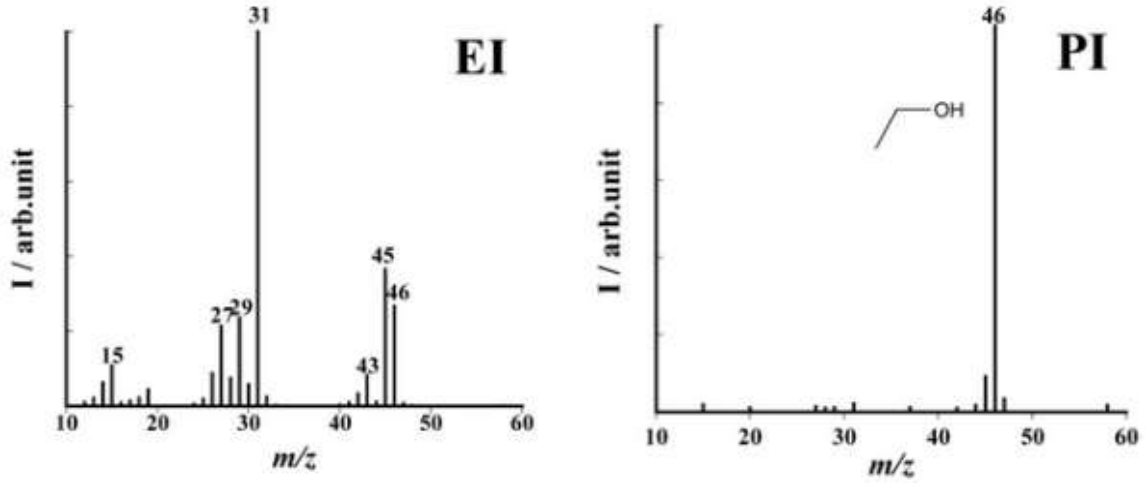

Figure 5-1. Difference in mass spectra of ethanol obtained by electron EI and PI. Adapted from Arii et al. (2006).

In this study, we have developed and evaluated a custom-built photoionization mass spectrometry (PI-MS) platform to examine whether PI can serve as a practical, low-fragmentation alternative to EI in analogue environment conditions for spacecraft instrumentation. This system integrates a vacuum-ultraviolet (VUV) light source, a quadrupole mass spectrometer, a high-vacuum chamber, and a precise gas-introduction module to measure the ionization efficiency and the fragmentation ratios. In the following sections, we describe the principles of photoionization, the design and construction of the experimental system, and the initial results to assess the effectiveness of PI as a soft ionization technique, which may potentially apply to future planetary exploration missions.

5.2 Experimental Methods

5.2.1 Construction of the Photoionization Experimental Apparatus

To quantitatively evaluate the effectiveness of the photoionization (PI) method, a custom experimental system was constructed with a vacuum ultraviolet (VUV) light source, a quadrupole mass spectrometer (QMS), and a gas introduction line. The overall configuration of the system is shown in Figure 5-2. The vacuum chamber is a stainless-steel cylinder with an inner diameter of 25 cm and a length of 40 cm. Gas samples are introduced through a high-precision gas handling system connected to the exterior of the chamber. The pumping system consists of a turbomolecular pump (TMP) backed by a rotary pump (RP) and equipped with a foreline trap to prevent oil backstreaming. Under these conditions, a base pressure of 8×10^{-5} Pa was achieved, and after the gas samples introduction, a stable operating pressure of 5×10^{-3} Pa was maintained.

A quadrupole mass spectrometer (QMS; Canon Anelva QMA-201) and a VUV lamp (Hamamatsu Photonics L10706) were installed at opposite ends of the chamber. The QMS was operated with the secondary electron multiplier (SEM) voltages of 1.5 kV for EI and 2.5 kV for PI, which acquired gains of approximately 10^3 and 10^4, respectively. The VUV lamp provided strong emission peaks in the 9–11 eV photon-energy range. Inside the chamber, the QMS head was positioned perpendicular to the VUV irradiation axis to ensure that the ionization region would coincide with the optical axis. In addition, the QMS electrode voltages were optimized, based on the simulated electric field distribution within the chamber to establish stable detection conditions for PI-derived ion signals. Furthermore, to minimize attenuation of VUV, the illumination window of the VUV lamp was positioned as close as possible (approximately 1 cm) to the QMS head (Figure 5-3(b)). This configuration maximized the effective light intensity from the VUV source and enhanced the photon density within the ionization region. The position of the lamp was carefully adjusted to irradiate the ionization zone precisely, while avoiding interference with the internal

structure of the QMS. The candidate designed, constructed, and operated the experimental apparatus, described in detail in the following section.

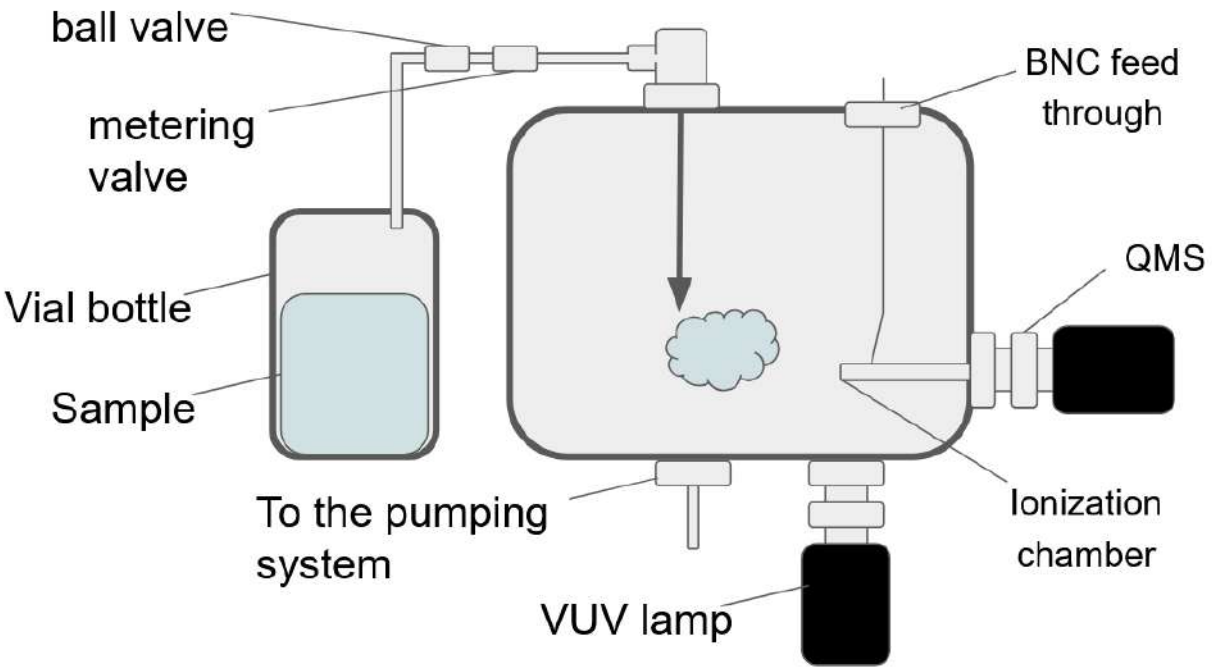

Figure 5-2. Configuration of the photoionization analysis system.

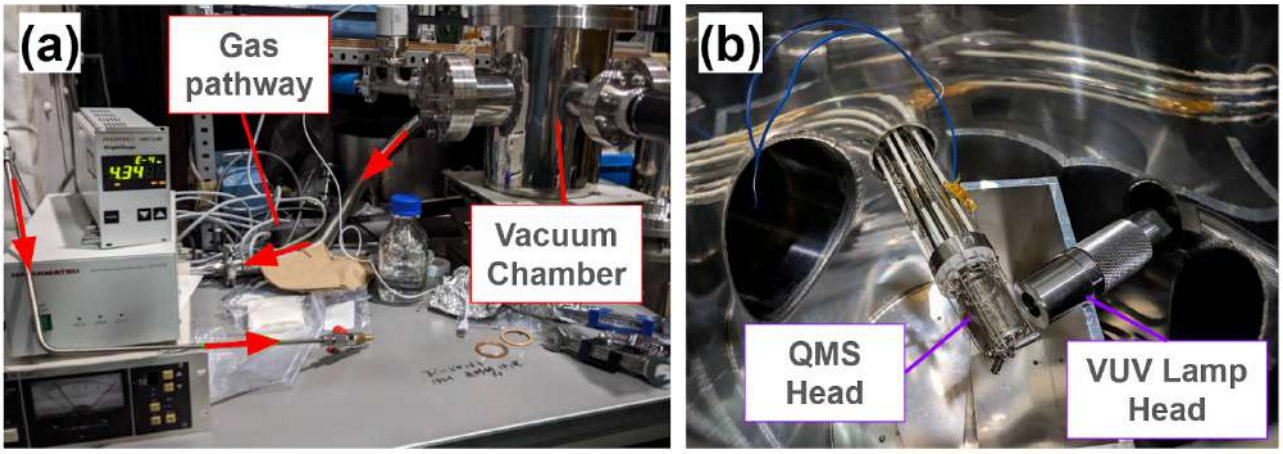

Figure 5-3. Photographs of the photoionization analysis system. (a) The vacuum chamber and the gas introduction system, and (b) QMS head and VUV lamp head inside the vacuum chamber.

5.2.2 Modification of the Quadrupole Mass Spectrometer for Photoionization Compatibility

The quadrupole mass spectrometer used in this study (QMA-201, Canon Anelva) was originally designed for EI and was found to malfunction when directly applied to PI measurements. Specifically, when the electron gun was turned off and the VUV lamp was turned on, abnormal current signals appeared in the electron-repeller circuit (Figure 5-4), leading to failure of the total pressure monitoring function. This issue was traced to photoelectric emission from the repeller electrode, which is directly exposed to VUV light during PI operation. The emitted photoelectrons introduced spurious currents into the repeller;when the repeller monitored the pressure but resulted in false readings and unstable operation. In a conventional EI mode, a negative potential (typically −20 to −120 V) was applied to the repeller electrode to direct electrons emitted from the electron gun into the ionization region. However, in the PI mode, the electron gun was deactivated, and such electron-beam control was not necessary. Moreover, if the repeller remained negatively biased, it would tend to draw away the positive ions generated by PI and drastically reduce ion collection efficiency.

With these reasons, we electrically disconnected the repeller circuit from the main EI circuitry and modified it to accept an externally supplied bias voltage through an independent power source. This modification effectively blocked unwanted photocurrents from entering the repeller circuit and restored stable pressure readings. Furthermore, by setting the repeller potential to +5 V, the local electric field inside the ionization region was gently shaped to guide the photoionized positive ions efficiently toward the quadrupole electrode assembly.

As the result of these modifications, stable photoionization measurements with the QMS were successfully achieved, allowing for the acquisition of pure PI spectra without the use of an electron gun. This method provides valuable technical insights for adapting the existing EI-based

instruments to PI measurements and offers a solid technological foundation of future mass spectrometer designs suitable for space missions.

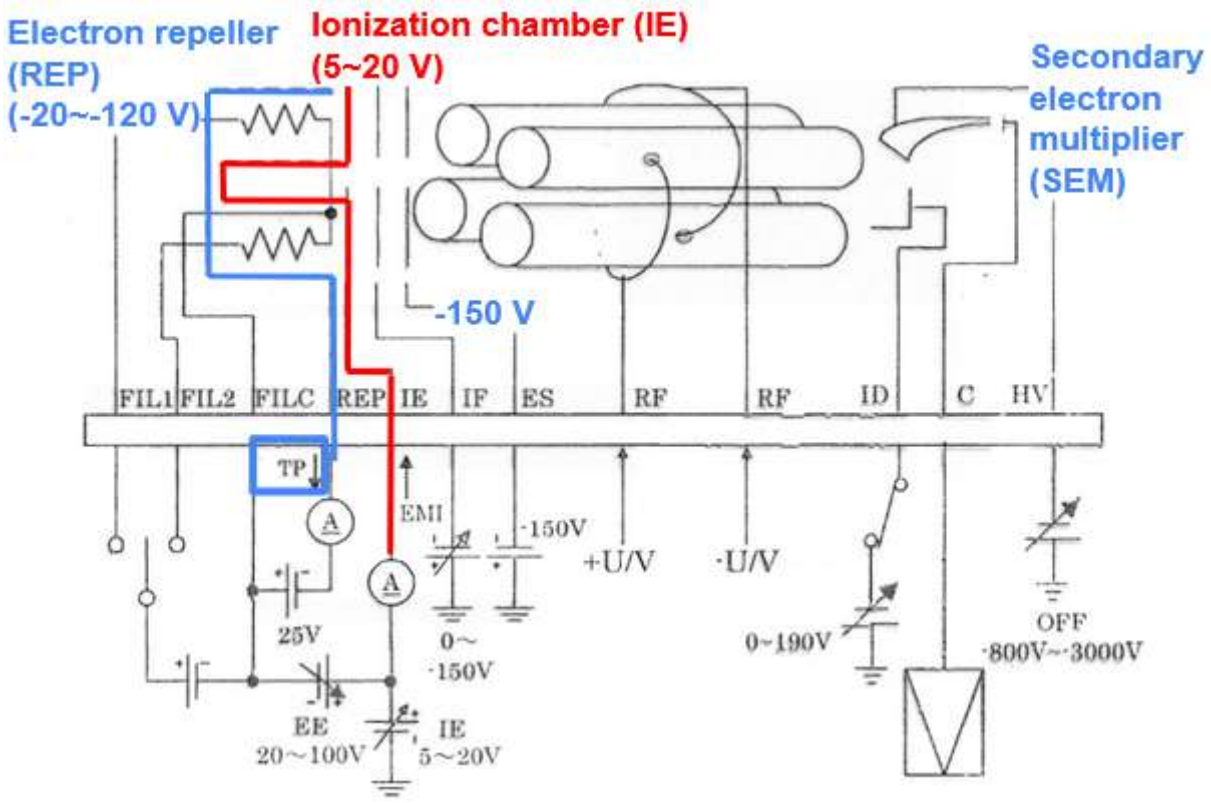

Figure 5-4. Circuit Diagram of the QMS (QMA-201, Canon Anelva)

5.2.3 Gas Sample Introduction System

In this experiment, it is essential to introduce the sample gas precisely and stably from atmospheric pressure into the high-vacuum chamber. To achieve this, an original gas introduction system was designed and constructed (Figure 5-2). For vaporizing liquid samples, vacuum vials of 50 mL (SVF-50,Nichiden Rika Glass) were used to tightly seal gas with PTFE-liner caps. After evacuating the vial with a diaphragm pump, nitrogen gas (N_2) and the liquid sample were introduced. The vial

was then heated to approximately 80 °C using a ribbon heater to promote vaporization. From the vial to the vacuum chamber, the connection was made with an ultimate plus-treated inert stainless-steel capillary tube (1/16"), whose inner diameter is 200 μm. This microcapillary was inserted through the PTFE-liner cap, allowing the vaporized gas inside the vial to be drawn into the vacuum line. Along the flow path, a 1/16" ball valve and a metering valve were installed, the former for on/off control, and the latter for fine adjustment of the flow rate. Through this configuration, gaseous components were generated from liquid samples under atmospheric pressure, enabling a stable molecular flux to be supplied into the chamber while minimizing the pressure increase inside. This gas introduction system allowed the gas concentration during PI measurements to be precisely and reproducibly controlled.

5.2.4 Sample Selection

In this experiment, three representative organic molecules, ethanol, acetone, and o-xylene, were selected as target samples. o-Xylene represents the analog of aromatic compounds observed in the icy plume of Enceladus, one of the satellites of Saturn (e.g., Khawaja et al., 2019; Waite Jr. et al., 2018, and Khawaja et al., 2025). Ethanol and acetone were typical low-mass organic molecules. These compounds exhibit distinct ionization potentials and molecular structures, making them suitable for evaluating the dependence of ionization efficiency on photon energy. The photoionization cross sections of these molecules and the emission spectrum of the deuterium lamp are shown in Figure 5-5. Specifically, ethanol (10.48 eV) (Person and Nicole, 1971), acetone (9.70 eV) (Zhou et al., 2009), and o-xylene (8.56 eV) (Zhou et al., 2009) can all be ionized within the high-intensity spectral region of the light source (9.5–10.5 eV), which makes them ideal samples for comparing and analyzing the relationship between photon energy and molecular response.

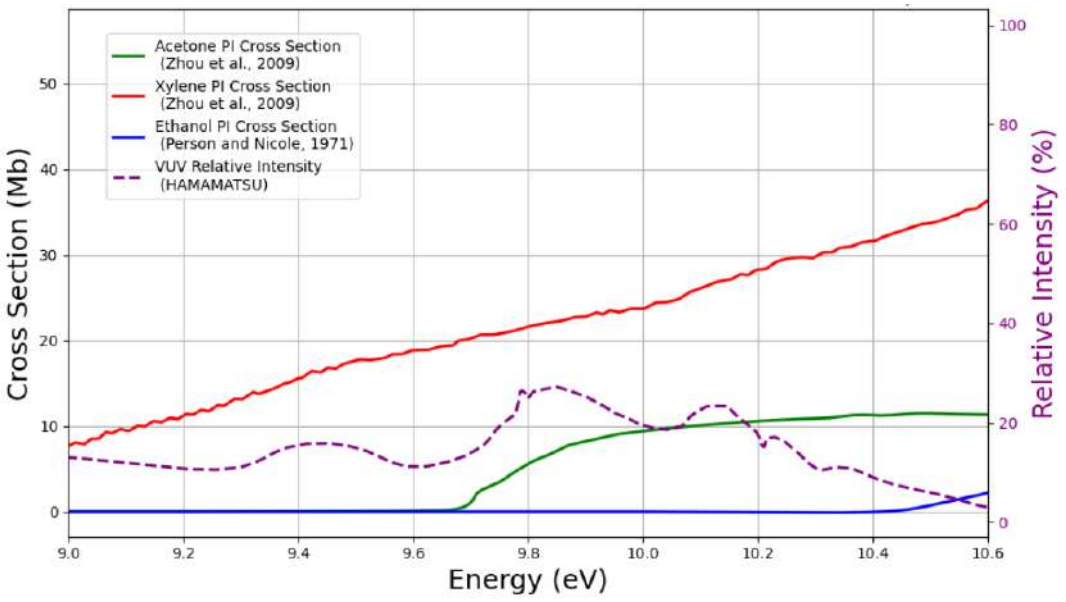

Figure 5-5. Photoionization cross sections and energy characteristics of the VUV deuterium light source. The values of the cross section are obtained by Person and Nicole (1971) and Zhou et al. (2009).

5.3 Results

In this section, we present the mass spectra obtained with the PI experimental apparatus explained in the previous sections and compare them with those acquired through conventional EI spectra also obtained with the same apparatus. As for the gas samples, o-xylene was used as a single-component specimen, and a mixture of ethanol and acetone was employed as a multi-component specimen. The o-xylene gas was introduced into the chamber at room temperature through the sample introduction system, while a mixture of ethanol and acetone was heated to 80°C before being introduced. The elevated temperature ensured sufficient vaporization of both components and stable pressure control during the measurement.

Figure 5-6 compares the mass spectra of o-xylene (molecular weight = 106, vapor pressure = 8.8 hPa) obtained under both EI and PI conditions. Figures 5-6 (a) and (b) show the raw spectra measured under the EI and PI modes, respectively.

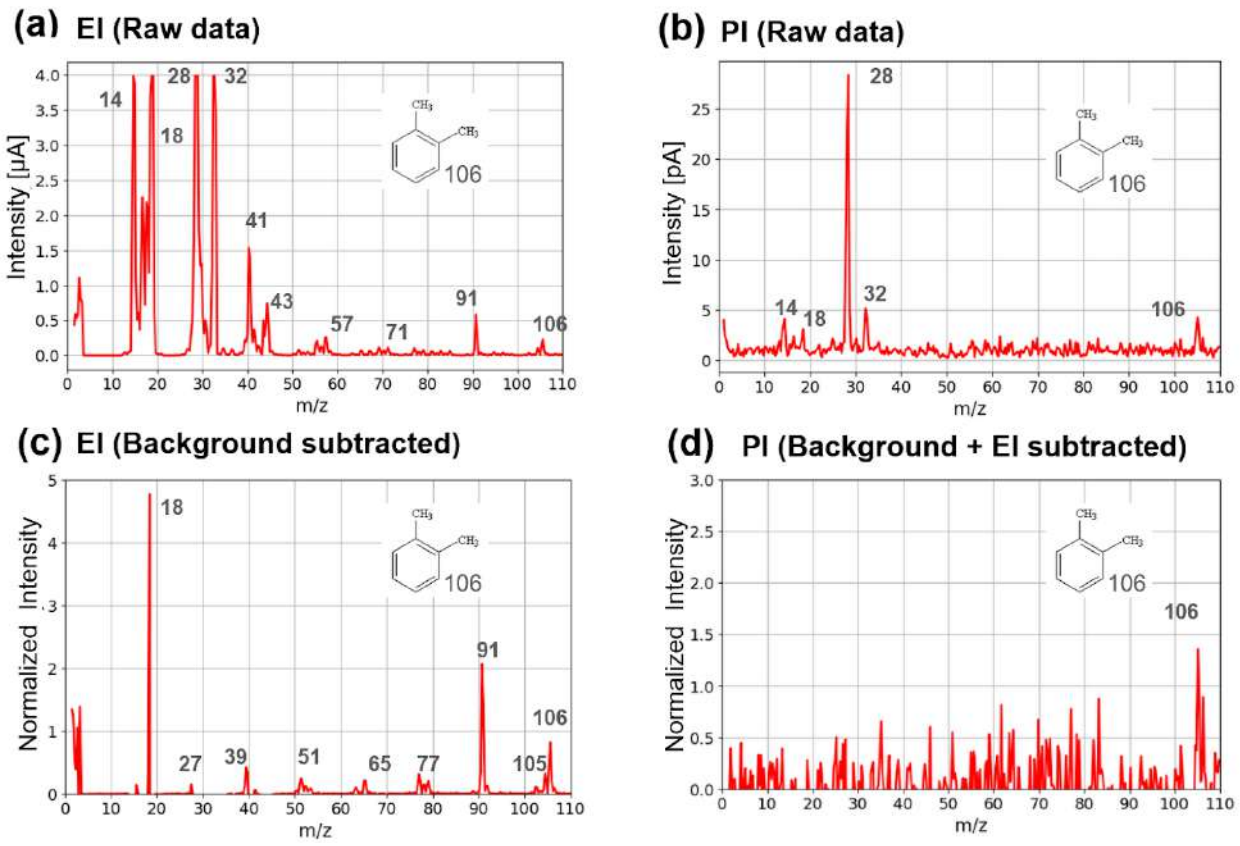

Figure 5-6. Comparison of mass spectra of o-xylene obtained by electron ionization (EI) and photoionization (PI). The panels (a) and (b) show the raw spectra measured under EI and PI conditions, respectively. The panel (c) represents the EI spectrum after background subtraction. The panel (d) shows the PI spectrum after subtraction of both background and residual EI contributions. The panel (c) and (d) is normalized at m/z = 28 at the background subtraction.

In addition to the molecular ion (m/z = 106) and the characteristic fragment ion (m/z = 91, tropylium ion), multiple peaks such as m/z = 14, 28 (N_2), 18 (H_2O), 32 (O_2), 41, 42, 57, and 71

(linear alkyl carbenium ions) were observed in the EI spectrum (Figures 5-6 (a)). These peaks are attributed to residual gas contamination, as also confirmed by the background gas analysis. After subtracting the background spectrum from the raw data, normalized at m/z = 28, the processed spectrum(Figures 5-6 (c)) revealed well-known minor fragment peaks of o-xylene at m/z = 27, 39, 51, 65, and 77.

In contrast, the PI spectrum (Figures 5-6 (b)) in Figure 5-6 exhibits a clear molecular ion peak at m/z = 106 and shows no signal at m/z = 91, which was the strongest peak in the EI spectrum. However, in the low-mass region (m/z = 10–40) of the PI raw spectrum, peaks at m/z = 14, 28 (N_2), 18 (H_2O), and 32 (O_2) were still observed. Because these stable molecules have ionization potentials of approximately 12–15 eV, which was higher than the maximum photon energy emitted by the VUV lamp (see Figure 5-5), these signals are attributable to secondary electron ionization. This phenomenon likely originates from photoelectrons emitted from metallic components such as the repeller electrode when irradiated by VUV light, thereby locally inducing residual EI. Although partial elimination was achieved through circuit modification and subtraction processing, complete suppression will require further optimization of optical shielding and potential control in future work.

To further reduce the influence of secondary electron ionization, the background-subtracted EI spectrum (Figures 5-6 (c)) was normalized at m/z = 28 and subtracted from the normalized PI spectrum (Figures 5-6 (b)), yielding the processed spectrum (Figures 5-6 (d)). In this final spectrum, only the molecular ion peak at m/z = 106 remains, indicating that no fragmentation occurred during the ionization process. The strong molecular-ion dominance and suppression of fragmentation observed in the PI spectra demonstrate that the newly developed system successfully achieved soft ionization of o-xylene . These results are consistent with the previous reports (e.g., Arii et al., 2006), confirming the effective operation of the photoionization process in this apparatus.

Figure 5-7 shows the EI and PI spectra obtained after introducing a gas sample prepared by evaporating the 1:1 volume mixture gas of ethanol and acetone. This experiment was designed to simulate a mixed organic sample, where multiple volatile compounds coexist in a planetary or ambient atmosphere. The gas mixture was preheated to 80°C to ensure complete vaporization before being introduced through the sample introduction system. The spectra were processed in the same manner as for o-xylene: the EI data were corrected by subtracting the background spectrum, and the PI data were corrected by subtracting both background and residual EI components. As shown in the EI spectrum, numerous fragment peaks appear due to molecular dissociation, making it difficult to distinguish between the two components. In contrast, the PI spectrum exhibits clear molecular ion peaks with minimal fragmentation, which simplifies the identification of individual compounds within the mixture. These results demonstrate that PI enables direct observation of parent molecular ions with reduced organic fragmentation, whereas EI provides detailed structural information through the characteristic fragment ions. Therefore, combining both EI and PI analyses can offer complementary insights, allowing comprehensive identification of organic species in complex environments.

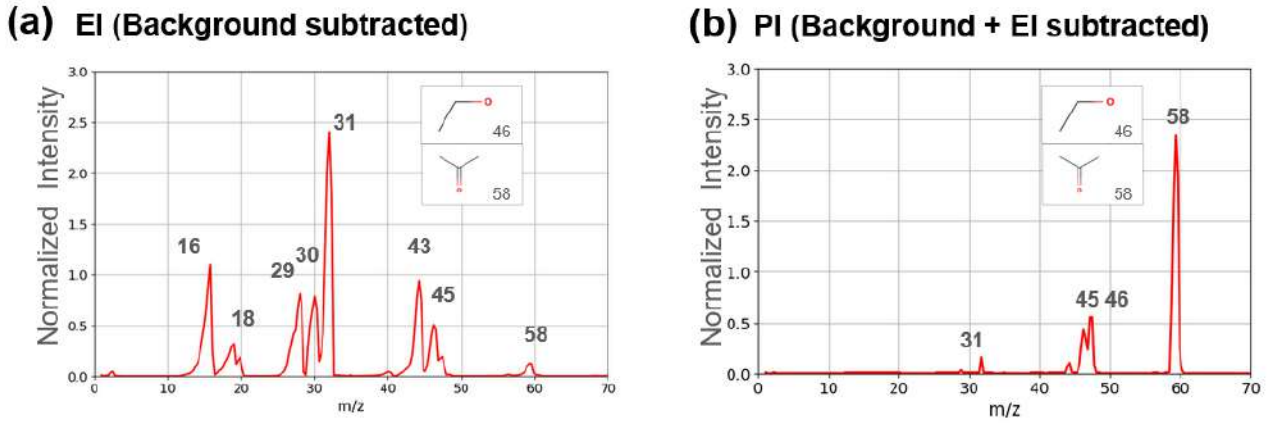

Figure 5-7. Comparison of processed mass spectra of the gas mixture of ethanol and acetone (molecular weight = 46 and 58, respectively) obtained under (a) EI and (b) PI conditions after the background corrections.

5.4 Discussion

5.4.1 Experimental Limitations and Sensitivity of PI

As shown in Figure 5-6 (a, b), the observed signal intensity differs significantly between EI and PI. In the EI mode, the peak current at m/z = 91 was approximately 5×10^{-7} A, whereas in the PI mode, the molecular ion at m/z = 106 yielded only 5×10^{-12} A. The QMS was operated with a secondary electron multiplier voltage of 1.5 kV (gain $\approx 10^3$) for EI and 2.5 kV (gain $\approx 10^4$) for PI, and with a scan speed of 0.1 s/amu for EI and 1 s/amu for PI. Therefore, under identical sample concentrations, the PI signal is about six orders of magnitude weaker. This difference in signal strength explains the large contrast in S/N ratios between the EI and PI spectra of o-xylene shown in Figure 5-6.

In contrast, the PI spectra of ethanol and acetone shown in Figure 5-7 (b) exhibit a much higher S/N ratio. This is largely attributed to the difference in vapor pressures of the samples. At 25°C, the saturation vapor pressure of o-xylene is 8.8 hPa, while those of ethanol and acetone are 55.8 hPa and 245 hPa, respectively. Furthermore, in this experiment, the ethanol–acetone mixture was heated to 80°C prior to introduction, resulting in a vapor pressure exceeding atmospheric pressure. These conditions indicate that, in PI measurements, sample concentration exerts a stronger influence on signal intensity than the photoionization cross section itself.

Indeed, Figure 5–6(d) suggests that o-xylene introduced at room temperature was close to the detection limit of the current system. Considering the partial pressure ratio, the introduced o-xylene concentration was approximately 0.78%, which represents the lower detection limit of this setup. In contrast, Naraoka et al. (2023) reported that aromatic hydrocarbons in the Ryugu return samples were present at sub-ppm abundances, including alkylbenzenes and polycyclic aromatic hydrocarbons (PAHs). Therefore, the present photoionization sensitivity is clearly insufficient to

detect such trace-level organics. Although this sensitivity is not comparable to the ppb-level performance achieved by modern high-sensitivity mass spectrometers, it should be noted that the QMS gain used here (≈10^4 at 2.5 kV) is also relatively low. The detection limit could be improved through optical focusing of the VUV source, enhancement of lamp intensity, optimization of the ionization chamber geometry, and sample preconcentration techniques.

5.4.2 Modeling of the Photoionization Process

In this section, a theoretical model is developed to interpret the experimental results presented in the previous sections. The model describes the propagation of VUV photons within the chamber and the resulting ion generation process. In particular, the photon transmission efficiency from the VUV light source to the QMS ionization region, as well as absorption and scattering interactions with gas molecules, are quantitatively evaluated to determine the spatial distribution of the ion generation density. The calculation is performed using a three-dimensional spatial model implemented in a Python program, with a uniform cell size of 0.1 mm. Within this framework, the ion generation rate in each cell is calculated based on the local photon flux and gas density, and photoionization cross section of o-xylene, acetone, and ethanol (Figure 5-8).

The total ion generation rate detected by the QMS, R_{ion}, is obtained by integrating the local ion production rate over the effective ionization volume of the PI region (Figure 5-8(a)). The local ion generation rate per unit volume at position r, $R_{ion}(r)$, is expressed as the product of the local neutral gas number density $n_{gas}(r)$ and the ionization rate per molecule $\Gamma(r)$. Accordingly, the total ion generation rate is given by the volume integral over the ionization region V_{QMS}:

$$R_{ion}(r) = \int n_{gas}(r)\Gamma(r)dV_{QMS} \qquad (5\text{-}1).$$

Here, $\Gamma(r)$ is determined by the photoionization cross section $\sigma_{PI}(\lambda)$ of the target molecule and the local photon flux $\Phi(r, \lambda)$, such that

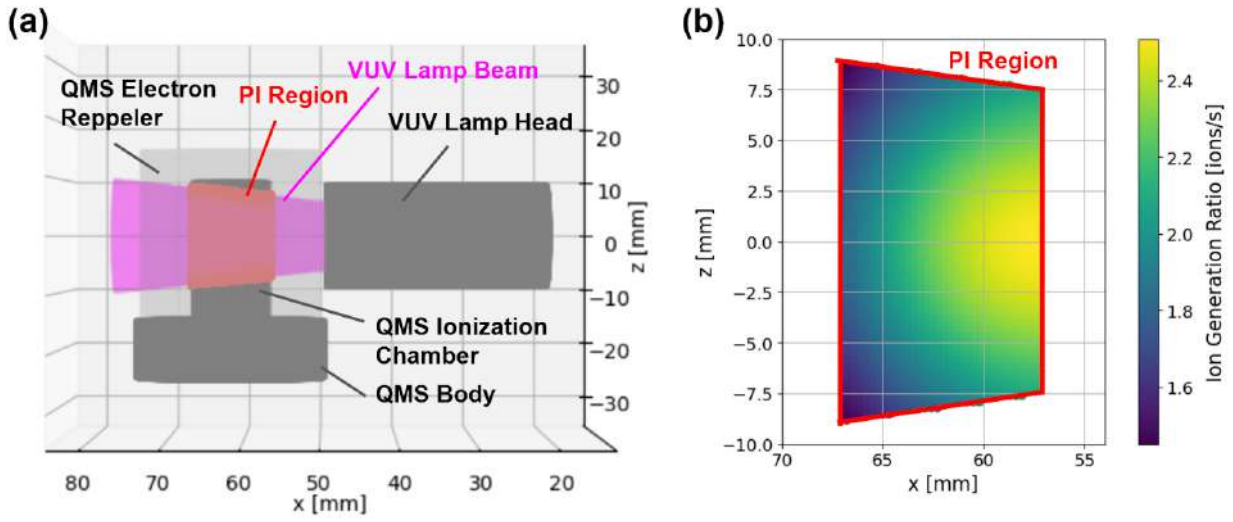

Figure 5-8. (a) Schematic view of the three-dimensional geometry used in the photoionization (PI) modelling, showing the relative positions of the VUV lamp head, the VUV lamp beam, the QMS ionization chamber, and the electron repeller electrode. The red-shaded region indicates the effective PI region where VUV photons overlap with the neutral gas inside the QMS head. (b) Cross-sectional distribution of the ion generation rate for o-xylene calculated within the PI region. The color scale represents the relative ion generation ratio (ions/seconds).

$$\Gamma(r) = \int \sigma_{PI}(\lambda)\Phi(r,\lambda)d\lambda \qquad (5\text{-}2).$$

The local photon flux is then determined by the spectral intensity of VUV source I_0 obtained from the manufacturer's catalog, and an attenuation factor $\alpha(r, \lambda)$:

$$\Phi(r,\lambda) = I_0(\lambda)\alpha(r,\lambda) \qquad (5\text{-}3).$$

The attenuation factor $\alpha(r,\lambda)$ accounts for geometric dilution due to the inverse-square law and for photon loss due to absorption and Rayleigh scattering along the propagation path, and is expressed as:

$$\alpha(r,\lambda) = \frac{1}{r^2} exp\{-n_{gas}(r)\{\sigma_{abs}(\lambda) + \sigma_{Rayleigh}(\lambda)\}r\} \quad (5\text{-}4),$$

where r denotes the distance from the VUV light source. The absorption cross section $\sigma_{absorption}$ was taken from experimental data reported by Rennie et al. (1998), Nobre et al. (2007), and Feng and Brion (2002) for o-xylene, acetone, and ethanol, respectively. The Rayleigh scattering cross section $\sigma_{Rayleigh}$ was calculated following the formulations by Sneep and Ubachs (2005) and Kawana et al. (2018).

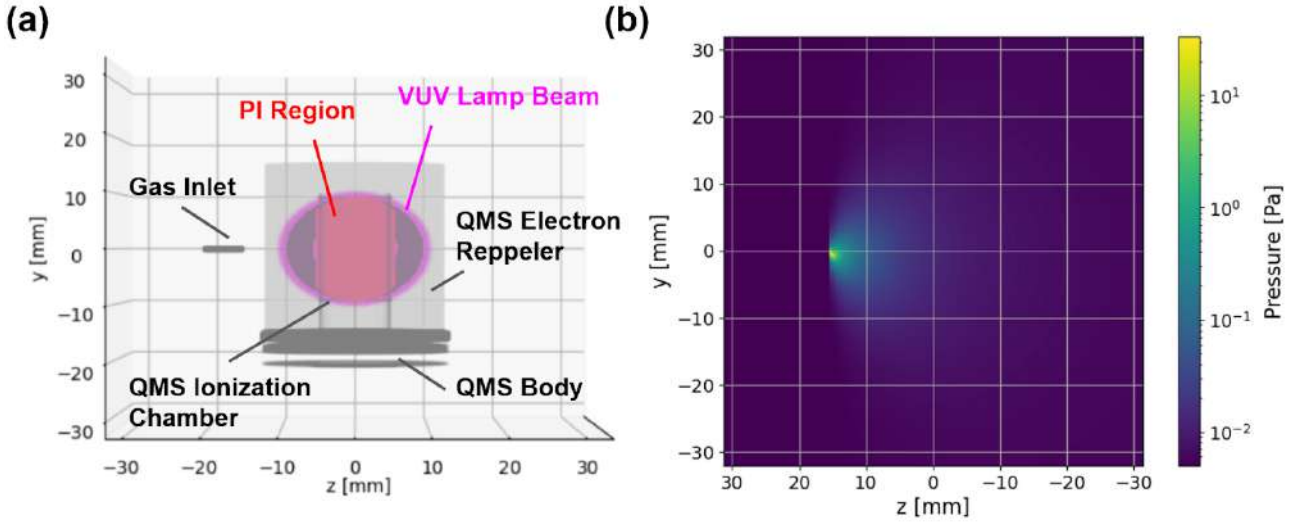

Figure 5-9. (a) Schematic view of the gas introduction geometry and the PI region used in the neutral gas density modelling. (b) Calculated spatial distribution of the neutral gas (o-xylene) pressure in the y–z plane under steady-state molecular flow conditions. The color scale represents the local pressure in units of Pa.

The local neutral gas number density $n_{gas}(r)$ is determined by the geometry of the PI region and the position of the sample gas inlet, which corresponds to the vacuum-side interface of the sample introduction system (Figure 5-9(a)). From this inlet, gas molecules enter the vacuum

chamber and propagate under molecular flow conditions. Under steady-state operation, the local pressure inside the chamber is governed by the effective pumping speed of the turbomolecular pump at 520 L s^{-1} and the steady pressure measured by the ion gauge as 5×10^{-3} Pa. The spatial distribution of the neutral gas is modelled, assuming that the molecular flow emitted from the inlet follows a cosine angular distribution, which is characteristic of diffuse molecular emission in the free-molecular regime. Based on these assumptions, the local neutral gas number density $n_{gas}(r)$ is calculated throughout the whole PI region, as shown in Figure 5-9(b), and is used as an input for the subsequent ion generation calculations. The resulting spatial distribution of the ion generation rate derived from this combined photon–gas model is shown in Figure 5-8(b).

To connect this model with the experimental output, it is necessary to extend the analysis to include ion transport and detection by the QMS. As shown in Figure 5-8(b), the ion generation within the PI region is spatially non-uniform. In particular, ions generated near the central axis of the PI region are expected to be efficiently extracted and transmitted into the quadrupole, whereas ions generated near the walls of the QMS ionization chamber are more likely to be lost due to unfavorable electric field configurations. To quantify this effect, the PI region was divided into six concentric zones according to the radial distance from the central axis of the PI region. For each zone, the ion collection efficiency was evaluated using ion trajectory simulations performed with an ion optics simulation software (SIMION; Dahl 2000) (Figure 5-10). The simulated collection efficiencies were then combined with the spatial ion generation rates derived from the photon–gas model to calculate the effective ion detection rate in units of Coulomb per second (C s^{-1}). This approach enables a direct quantitative comparison between the modelled ion detection rates and the experimental QMS signals presented in Figures 5-6 and 5-7.

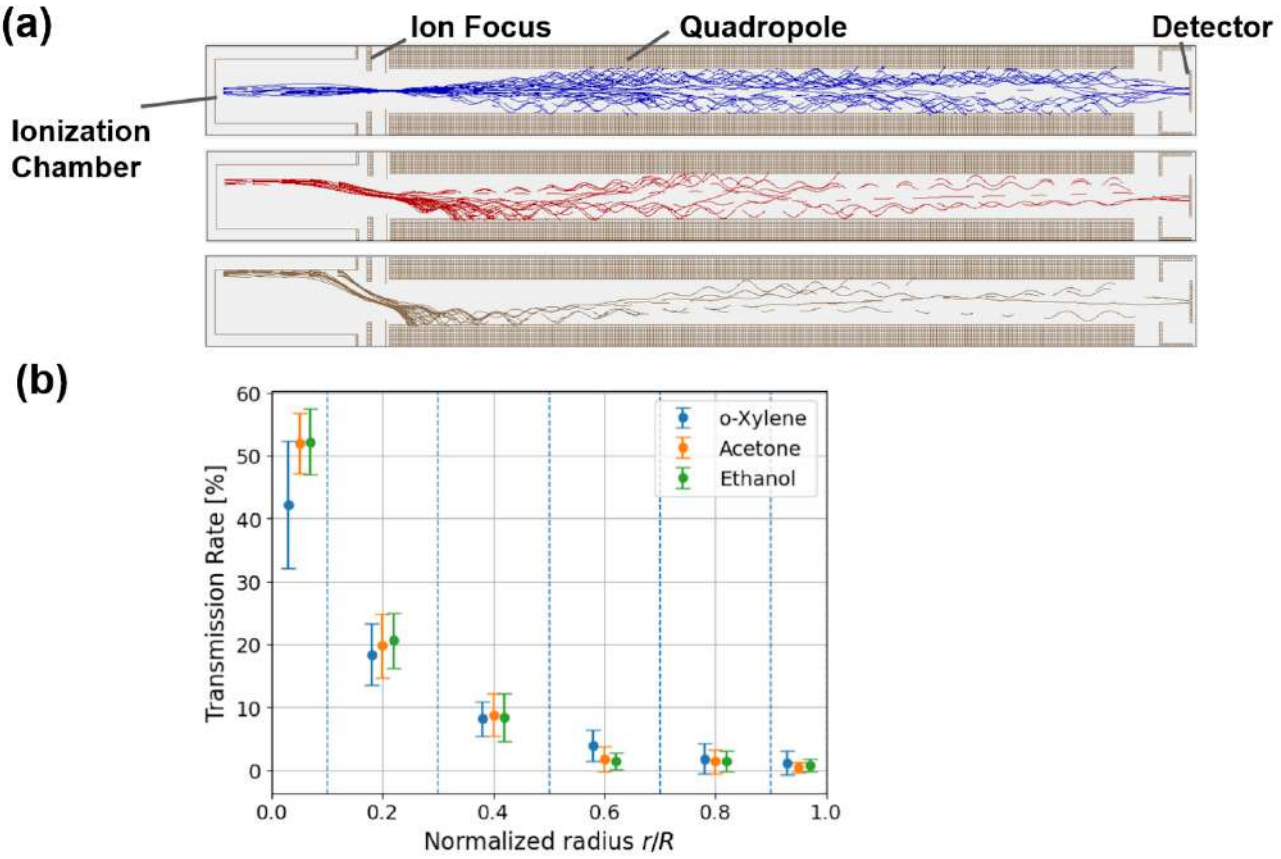

Figure 5-10. (a) o-Xylene ion trajectory simulations performed with SIMION for ions generated at different radial positions within the PI region. The three panels show representative ion trajectories originating from 0 - 0.1 (top), 0.3 - 0.5 (middle), and 0.9 -1.0 (bottom) in the normalized radial distance of r/R. (b) Ion transmission rate as a function of the normalized radial distance of r/R from the central axis of the PI region, also obtained from SIMION simulations.

Table 5-1 summarizes the experimentally measured ion detection rates and the corresponding modelling results for each sample. The experimentally measured ion detection rates were calculated from the mass spectra shown in Figure 5-6 (d) and 5-7(b). For o-xylene and acetone, the modelled ion detection rates are approximately a factor of two higher than the experimental values, which can be regarded as good agreement between the two results at the order-of-magnitude level. This discrepancy is attributed to loss processes that are not included in the present model, such

as recombination of generated ions, temporal degradation of the VUV lamp output, fluctuations in the QMS gain, and absorption of VUV photons by residual organic ions in the chamber.

In contrast, the modelled ion detection rate for ethanol reaches only approximately 16 % of the experimental value, resulting in significant underestimation. Although ethanol and acetone are introduced simultaneously into the vacuum chamber through the same gas introduction system, the observed enhancement of the ethanol signal cannot be explained solely by differences in molecular-flow jet diffusion, VUV photon attenuation, photoionization cross sections, or molecular-species-dependent transmission efficiencies of the QMS mass filter. Furthermore, QMS measurements performed under electron ionization conditions consistently show stronger signals for ethanol than for acetone, suggesting that the effective partial pressure of ethanol in the experimental system is selectively enhanced, relative to the supply conditions assumed in the model. A plausible explanation for this behavior lies in the polarity of ethanol molecules. Ethanol is prone to strong interactions with oxide layers and adsorbed water on the surfaces of the capillary and vacuum chamber walls, leading to temporary adsorption and accumulation on these surfaces (Salama et al., 2025). As a result, ethanol molecules retained on surfaces can be gradually released, depending on changes in gas introduction conditions or wall temperature, which increases the effective residence time and partial pressure of ethanol in the chamber. Such surface adsorption and delayed desorption effects, which are commonly reported for polarity of organic molecules under vacuum conditions, are not included in the simplified gas transport model employed in this study. Therefore they are considered to be the dominant cause of the systematic underestimation of the ethanol signal. It is important to note that this result does not invalidate the present mode but highlights that surface effects can play a critical role in determining detection sensitivity when analyzing polar molecules by photoionization.

Thus, at least for o-xylene and acetone, the ability of the simplified model to reproduce the experimentally observed ion detection rates within the same order of magnitude demonstrates that the model successfully captures the essential physical mechanisms governing photoionization and ion detection in the QMS, despite neglecting various loss processes. Consequently, the present model provides a valid first-order approximation for evaluating PI signal intensities and offers a useful framework for assessing the scaling behavior and dominant factors controlling detection sensitivity.

Table 5-1. Comparison between experimentally measured ion detection rates and model-predicted values for o-xylene, acetone, and ethanol.

	o-Xylene	**Acetone**	**Ethanol**
Experimental Result [ions s^{-1}]	1.01×10^3	6.43×10^4	2.31×10^4
Modeling Prediction [ions s^{-1}]	1.79×10^3	1.48×10^5	3.63×10^3
The experimental-to-model ratio [%]	56.4	43.4	636.4

Furthermore, sensitivity analyses performed during the construction of the present model revealed that, under low-pressure conditions on the sub-Pa order, attenuation of vacuum-ultraviolet (VUV) radiation is governed primarily by geometric dilution following the inverse-square law, rather than by molecular absorption or scattering processes. In this pressure regime, even a change of only a few centimeters in the distance between the gas inlet and the photoionization region of the QMS can lead to variations of more than two orders of magnitude in the amount of ionizable sample. The model also demonstrates that the photoionization region should be positioned as close as possible to the central axis of the QMS, and that the increase in ion yield resulting from enhanced VUV light intensity can be quantitatively evaluated within this framework.

These results indicate that the sensitivity of photoionization mass spectrometry is strongly influenced not only by the intrinsic photoionization cross sections of target molecules, but also by instrument geometry and optical configuration. Accordingly, the model developed in this chapter provides a robust basis for interpreting the experimental results and for guiding the optimization of photoionization-based mass spectrometric systems.

5.5 Future Work

Unlike EI, PI is inherently selective. Due to differences in photoionization cross section, stable molecules with high ionization potentials such as H_2O,its clusters, O_2, and N_2 are not efficiently detected. On the other hand, low ionization potentials such as O-bearing compounds and aromatic species are more readily ionized. Such compounds have been reported in Enceladean ice grains analyzed by Cassini CDA (e.g., Khawaja et al., 2019) and are also known to be abundant as PAHs in interstellar dust (e.g., Spencer et al., 2008). In addition, Feldmann et al. (1987) demonstrated that VUV irradiation of vaporized fragments generated by laser ablation of polystyrene selectively ionizes aromatic fragments via PI.

Taken these results together, they suggest that photoionization could realistically enable the detection of trace organic fragments generated by impacts, as in the hypervelocity impact experiments conducted by Burchell et al. (1999, 2002), Goldsworthy et al. (2002, 2003), Srama et al. (2009), Burchell and Armes (2011), Mikula et al. (2023) and in Chapter 4 of this study. However, actual spacecraft instruments must analyze highly heterogeneous mixtures of sublimated gas induced by microparticle impacts, rather than uniform samples such as polystyrene spheres, where the amount of analyzable material will be far smaller. Therefore, future work should focus on

sensitivity estimation and optimization for the detection of extremely low-abundance organic fragments, which are expected in realistic impact scenarios of space missions.

In this context, the sensitivity of the photoionization system can be tuned through several key parameters: increasing the detector voltage enhances gain, while increasing the photon flux of the VUV lamp improves ionization efficiency. However, higher photon flux inevitably demands effective thermal management of the lamp. To quantitatively assess these trade-offs, this study models photoionization processes under vacuum conditions, using both the experimental data obtained and the catalog specifications of the VUV lamp. The objective is to evaluate how photon flux correlates with detectable molecular concentrations, and to estimate the associated requirements in terms of electrical power, heat dissipation, and mass budget of the instrument that are critical for the design of future PI-MS instruments to be onboard spacecraft.

However, sensitivity alone is not sufficient for the detection of impact-generated volatile species in space environments. In the present experiments, the SEM installed in the QMS provided a relatively low gain of approximately 10^4 at an applied voltage of 2 kV. To achieve a sufficient signal-to-noise ratio, a scan speed of 1 s amu^{-1} was required in the PI mode. As a consequence, scanning up to 104 amu for o-xylene required more than 100 s, during which a stable and steady gas concentration had to be maintained. In contrast, according to Perry et al. (2014), volatile molecules generated by ice grain impacts in the Cassini Ion and Neutral Mass Spectrometer (INMS) remained in the system for only approximately one integration period (IP), corresponding to about 31 ms (Wu et al., 2022). To detect such short-lived volatile species, a benchmark requirement is to scan a mass range up to ~100 amu within 31 ms, implying a scan speed on the order of 300 μs amu^{-1}. This represents a required improvement of approximately four orders of magnitude compared to the present experimental conditions. Achieving such performance will require either a substantial

increase in the SEM gain, the development of mechanisms to increase the effective sample introduction rate, or a combination of both approaches.

5.6 Summary

In this chapter, a new PI-MS system was developed and characterized to evaluate the applicability of PI as a soft and selective ionization method for analyzing gas species generated by impacts. The system integrates a VUV light source, a QMS, and a custom-designed gas introduction and heating line, enabling controlled experiments under laboratory conditions analogous to spacecraft-based analysis.

To adapt the conventional QMS for PI measurements, electrical modifications were implemented to eliminate photoelectric disturbances in the repeller circuit and to optimize ion collection efficiency. These adjustments allowed stable operation and successful acquisition of pure PI spectra without the use of an electron gun. The experimental platform thus established provides a practical framework for evaluating the ionization characteristics of organic molecules under VUV irradiation.

Comparative measurements between EI and PI revealed clear differences in fragmentation behavior and sensitivity. For o-xylene, the EI spectrum exhibited extensive fragmentation, dominated by the tropylium ion (m/z = 91), while the PI spectrum showed a single molecular ion peak at m/z = 106, confirming the effectiveness of PI as a soft ionization process. For mixed samples of ethanol and acetone, PI spectra exhibited strong parent-ion signals with minimal fragmentation, demonstrating its capability for compositional identification in complex organic mixtures. These results verify that the developed PI-MS system successfully achieved gentle ionization while maintaining sufficient selectivity for molecular analysis.

However, the overall PI signal intensity was found to be about six orders of magnitude lower than that of EI under identical conditions, primarily due to differences in ionization efficiency and sample concentration. The PI signal intensity showed a strong dependence on the vapor pressure of the analyte, as demonstrated by the markedly higher S/N ratios for ethanol and acetone compared to o-xylene. Under the present experimental conditions, this result indicates that analyte concentration plays a more critical role in determining detectable signal strength than differences in photoionization cross section. The current detection limit for o-xylene, corresponding to a concentration of approximately 0.78 %, therefore defines the sensitivity threshold of the present system.

A simplified photon–gas transport model combined with SIMION-based ion-collection efficiency calculations further revealed that, in the sub-Pa pressure regime, attenuation of VUV radiation is dominated by geometric dilution following the inverse-square law rather than by molecular absorption or scattering. The model also indicates that centimeter-scale variations in the distance between the gas inlet and the photoionization region, as well as off-axis ion generation, can alter the effective ionizable sample amount by more than two orders of magnitude, highlighting instrument geometry as a key driver of PI sensitivity.

Future improvements should focus on enhancing sensitivity through optical focusing of the VUV beam, increasing photon flux, optimizing the ionization chamber geometry, and implementing sample enrichment techniques. In addition, achieving time-resolved detection relevant to spacecraft measurements will require substantially faster mass scanning and/or higher detector gain, motivating improvements in SEM performance and sample delivery strategies. These advances will further establish photoionization as a powerful tool for in-situ analysis of trace organic materials in hypervelocity impact experiments and future planetary missions.

Chapter 6 Conclusions and Future Perspectives

6.1 Conclusions

6.1.1 Summary of the Present Study

This dissertation presented an integrated study combining theoretical, numerical, and experimental approaches to understand ionization and fragmentation processes during hypervelocity impacts. The central objective was to demonstrate that mass spectrometric (MS) analysis of gas-phase products generated by impact-analog laser ablation can preserve molecular structures more effectively than direct MS analysis of impact-induced plasma. To achieve this goal, a sequential framework was established: (1) development and validation of a radiation–hydrodynamics code capable of describing non-equilibrium ionization, (2) theoretical formulation of the equivalence between laser irradiation and hypervelocity impacts, (3) experimental verification of molecular preservation through electron-impact (EI) MS, and (4) exploration of photoionization (PI) as a softer ionization technique for future applications.

In Chapter 2, a two-temperature radiation–hydrodynamics code called P4P was developed and adapted to describe non-equilibrium plasma generation during hypervelocity impacts. The model incorporated electron–ion temperature exchange, heat conduction, radiative transport, and ionization processes based on the QEOS, with a potential-barrier-based correction for partial ionization. These simulations have successfully reproduced the velocity scaling of ion yield ($Q/m \propto v^{4.8}$) observed in previous experiments (Ratcliff et al., 1997; Burchell et al., 1999) and confirmed that the essential physics of impact ionization including its spatial localization, temporal evolution,

and velocity dependence were consistently captured. These results demonstrated the reliability of the P4P framework as a quantitative tool for describing transient, non-equilibrium ionization in hypervelocity impacts.

In Chapter 3, the validated P4P framework was used to establish a physically grounded correspondence between laser irradiation and impact ionization. The simulations clarified how nano-second laser pulses can thermodynamically reproduce the high-temperature and high-pressure states of hypervelocity impacts. By comparing the temporal evolution of ion yield, ion temperature, it was shown that matching with the charge-weighted average of the maximum ion temperature provides a potential equivalence criterion between these two processes. Ion energies obtained under certain laser fluences (~1 GW cm^{-2}) which were quantitatively coincided with those produced by impacts at 14–19 km s^{-1}. This result justified the use of laser irradiation as a controlled analog for hypervelocity impacts, providing a theoretical and practical foundation for designing laser-driven experiments that mimic natural dust impacts.

Building on this foundation, Chapter 4 experimentally investigated laser ablation of polystyrene under the conditions derived from Chapter 3. We used electron-impact (EI) mass spectrometry to analyze the resulting vapor. The results demonstrated that laser-generated gas-phase products retained a much richer set of molecular features, compared with plasma-based hypervelocity impact MS. The persistence of styrene monomer and oligomer-derived peaks, together with enhanced linear alkyl carbenium ions, indicated that the laser-analog gas represents a chemically softer regime, corresponding to partial vaporization rather than full plasma ionization. These findings provided the first experimental validation of the central hypothesis that gas-phase MS analysis of impact-analog vapor can preserve molecular structures more effectively than direct plasma analysis, thereby offering a gentler and more compositionally faithful diagnostic of impactor molecules such as long-chained organics.

In Chapter 5, the study advanced toward the realization of a truly soft ionization technique by developing a photoionization mass spectrometry (PI-MS) system. The instrument was composed with a VUV light source, a quadrupole mass spectrometer, and a custom gas-handling system and enabled laboratory measurements of organic gases under spacecraft-analog conditions. Comparative analyses between EI and PI revealed the clear advantages of photoionization. For o-xylene and mixed organic vapors, PI produced dominant parent-ion peaks with much less fragmentation than EI, confirming its ability to better preserve molecular integrity. Although the absolute signal intensity was lower than that of EI, primarily due to differences in ionization efficiency and sample concentration, the achieved selectivity toward molecules with low ionization potentials highlights PI's potential utility in detecting oxygenated and aromatic organics relevant to planetary and astrophysical environments. These results have proven the PI-MS as a promising analytical technique for future in-situ dust and volatile analysis missions. To interpret these experimental results and to identify the key factors that govern PI sensitivity, a simplified photon–gas transport model combined with ion-trajectory simulations was also developed. The modelling demonstrated that, in the sub-Pa pressure regime relevant to the present experiments, attenuation of vacuum-ultraviolet radiation is dominated by geometric dilution, following the inverse-square law rather than by molecular absorption or scattering. Furthermore, the model revealed that centimeter-scale variations in the distance between the gas inlet and the photoionization region, as well as off-axis ion generation relative to the QMS central axis, can alter the effective ionizable sample amount. Taken together, the experimental and modelling results have established PI-MS as a promising analytical technique for future in-situ dust and volatile detection missions, while also providing quantitative design guidelines for optimizing sensitivity through geometric configuration and photon delivery in photoionization-based mass spectrometers. Overall, this dissertation has established a coherent and quantitative framework that links the microscopic physics of impact-induced gas ionization with practical analytical strategies for molecular detection. The

combination of radiation–hydrodynamics modeling, laser-analog experimentation, and advanced ionization techniques collectively provides a physically consistent bridge from fundamental plasma physics to applied planetary mass spectrometry. The results demonstrate that laser-based analogs, when guided by ion temperature equivalence, can reproduce key aspects of hypervelocity impact phenomena, and that photoionization enables molecularly soft, compositionally selective detection of impact-generated gases. These achievements lay the foundation for the development of soft impact mass spectrometry as a next-generation approach that can extend the chemical reach of spaceborne dust analyzers and enhance the scientific return of future planetary missions.

6.1.2 Conclusions

As discussed in Chapter 1, the first analysis of neutral gases generated by hypervelocity impacts using an EI-MS system had been incidentally realized with INMS onboard the Cassini spacecraft (ref.). Yet it had never been systematically validated through ground-based experiments until this study. In Chapter 4 of this dissertation, it was experimentally demonstrated that molecular structures can be preserved to a significantly greater extent by separating impact-generated neutral gas produced by sublimation and vaporization from the impact plasma, and by introducing it into an EI-MS system. This result constitutes the first experimental verification that EI-MS analysis of impact-induced neural gas does not necessarily entail excessive molecular fragmentation, challenging the previous assumption that hypervelocity impacts inevitably destroy most of molecular information of the impacting particles.

From the perspective of space exploration heritage, Cassini's observations of the Enceladus plume provide an important reference case. Waite Jr. et al. (2009) reported that, among several targeted flybys, the E5 encounter on October 9 in 2008 yielded the highest signal-to-noise ratio (S/N), enabling the first identification of complex organic molecules including benzene (C_6H_6) within the Enceladus' plume particles. According to Teolis et al. (2010), individual ice-grain

impacts were detected as sharp spikes within a single INMS integration period (31 ms). Even though INMS scanned masses sequentially in 1 Da steps, instantaneous spectra obtained during hypervelocity flybys did not directly reflect chemical composition. To address this limitation, Waite Jr. et al. (2009) constructed integrated datasets over the full plume-influenced interval, which enabled the detection and quantification of organic species. Detailed analyses by Teolis et al. (2010) indicate that approximately 33 ice-grain impact events were detected during the E3 flyby and approximately 41 events during the E5 flyby, all of which corresponded to impacts of sub-micrometer-scale particles. Under these conditions, Waite Jr. et al. (2009) reported benzene mixing ratios of 3.3×10^{-5} for E3 and 8.1×10^{-5} for E5, corresponding to concentrations on the order of 10–100 ppm. In contrast, benzene was not detected during the E2 flyby, which was inferred to have involved a substantially lower particle flux. These results suggest that a particle flux comparable to that encountered during the E3 and E5 flybys represents a necessary condition for detecting polymeric or aromatic organic species at the 10–100 ppm level using this measurement scheme. Although organic detection by INMS has often been described as “incidental,” the accumulated results of these prior works provide quantitative basis for discussing the reproducibility and operational requirements of such observations.

These considerations indicate that impact-generated gas EI-MS represents a measurement approach that is potentially capable of delivering substantial scientific returns at relatively low development risk and cost by leveraging the technological heritage of existing neutral gas analyzers (such as INMS) and compact mass spectrometers like QMS as an example. While detector performance in spaceborne mass spectrometers has improved significantly in recent decades (Figure 1-10), maximizing scientific output still requires optimization of upstream physical processes, including impact, sublimation, gas collection, transport, and ionization before introduction into mass spectrometers.

In conclusion, this dissertation demonstrates that neutral gases generated by hypervelocity dust impacts can be analyzed by mass spectrometry with substantial preservation of molecular information, even using conventional EI, provided that impact plasma and sublimated gas are physically separated and appropriately handled, thereby establishing impact-generated gas analysis as a viable and scalable strategy for high-fidelity organic detection in future planetary missions.

6.2 Future Work

At the end of each chapter, future challenges corresponding to the respective research topics have been discussed. Here we summarise the overall achievements of this dissertation,together with the remaining issues and future perspectives toward the development of an impact gas mass spectrometer for potential spaceborne applications.

6.2.1 The Advancement of Impact-Generated Gas EI-MS

As discussed in the previous section, observations of the Enceladus plume by the Cassini spacecraft demonstrated that the highest signal-to-noise ratios (S/N) were achieved during the E3 and E5 flybys, enabling the identification of complex organic molecules including benzene (C_6H_6) for the first time (Waite Jr. et al., 2009). During these flybys, ram pointing (incidence angle of 0°), in which the spacecraft velocity vector was aligned with the INMS aperture, was adopted, and the relative velocities with respect to Enceladus were as high as 14.4 km s^{-1} and 17.7 km s^{-1}, respectively. As a result, neutral molecules and icy grains within the plume were efficiently introduced into the closed-source antechamber of the INMS, leading to a substantial enhancement of the neutral gas density.

In contrast, during the E2, E4, and E6 flybys, where similar organic identification was difficult, the incidence angles were significantly larger (57°, 80°, and 73°, respectively), resulting in a drastic reduction in gas intake efficiency. These observations indicate that organic detection by the Cassini INMS strongly depended on highly constrained operational conditions, namely ram pointing combined with hypervelocity flybys.

Moreover, under such hypervelocity impact conditions, molecules entered the INMS antechamber with kinetic energies on the order of several eV per atomic mass unit. Consequently, not only direct impact-induced fragmentation but also chemical reactions with the chamber wall material, titanium, were unavoidable. Indeed, it has been reported that particle impacts exposed fresh titanium surfaces, leading to hydrogen production and secondary molecular transformations through reactions with water and organic species (Waite Jr. et al., 2009). As a result, it was difficult to unambiguously distinguish whether the organic signals observed by INMS originated from volatile molecules inherently present in the plume or from secondary products generated by impact fragmentation and intra-instrument reactions.

In summary, the Cassini INMS observations represent a critical proof-of-concept demonstrating that impact-sublimated neutral gas can be detected down to the organic molecular level using EI-MS. Yet this success was achieved under highly specific conditions of the Cassini mission, including hypervelocity flybys, encountering angles with respect to the ram pointing direction, and elevated particle flux. The instrument was not originally designed to intrinsically suppress molecular fragmentation or intra-instrument chemical reactions of impacting organic dust particles. These limitations strongly suggest that future spaceborne implementations of impact-generated gas EI-MS require a fundamentally new measurement architecture, rather than a direct extension of existing instrument designs, in which the processes of impact, sublimation, gas introduction, and ionization are deliberately controlled and optimized.

From the perspective of detector performance, the effective gain of the secondary electron multiplier (SEM) used in INMS was approximately 10^7 (Teolis et al., 2015), which is sufficiently high even when compared to the maximum detector gain ($\sim 10^8$) of the latest impact-plasma dust mass spectrometer SUDA currently onboard the Europa Clipper mission since 2024 (Kempf et al., 2025). Therefore, the most critical development challenge for future impact-generated gas EI-MS instruments lies not in the detector itself, but rather in the upstream design of sample collection, gas generation, and gas transport processes to the mass spectrometer.

The closed-source configuration of INMS was originally designed to improve the accuracy and sensitivity of inert neutral measurements by exploiting ram density enhancement. This was achieved by suppressing thermal leakage through a narrow aperture while limiting conductance via an orifice, thereby allowing temporary gas confinement within the chamber. Building on this design philosophy, a new geometric configuration for future impact-generated gas EI-MS is proposed, as schematically illustrated in Figure 6-1, in which a nozzle structure is introduced upstream of the antechamber.

Specifically, taking advantage of the fact that the relative velocity between the spacecraft and the plume is largely determined by the flyby velocity, incoming icy grains from the forward direction are made to undergo oblique impacts on a wide-aperture nozzle made of rhodium (Rh) at shallow incidence angles. This configuration allows control of the normal component of the impact energy while guiding the generated vapor plume toward the downstream, central axis of the nozzle. The gas is then introduced into a chemically inert Rh-coated antechamber, potentially enabling the maintenance or even enhancement of internal gas density, despite an increased aperture size.

Furthermore, in such an oblique impact geometry, the temperature achieved during shock compression is expected to decrease as a function of impact angle, thereby suppressing the generation of high-temperature plasma components during impact. As demonstrated in Chapter 3,

higher ion temperatures lead to increased degrees of molecular fragmentation; therefore, the proposed design is also advantageous from the perspective of preserving molecular structures. In addition, because this concept relies primarily on the geometric properties of the nozzle, no additional power consumption is required. The impact on spacecraft resources is thus limited to the mass of the nozzle itself. A notional estimate is approximately 4 kg for a representative design with a 20 cm aperture diameter, a nozzle half-angle of 30°, and a thickness of 5 mm. This can be even lighter if the structural design is advanced.

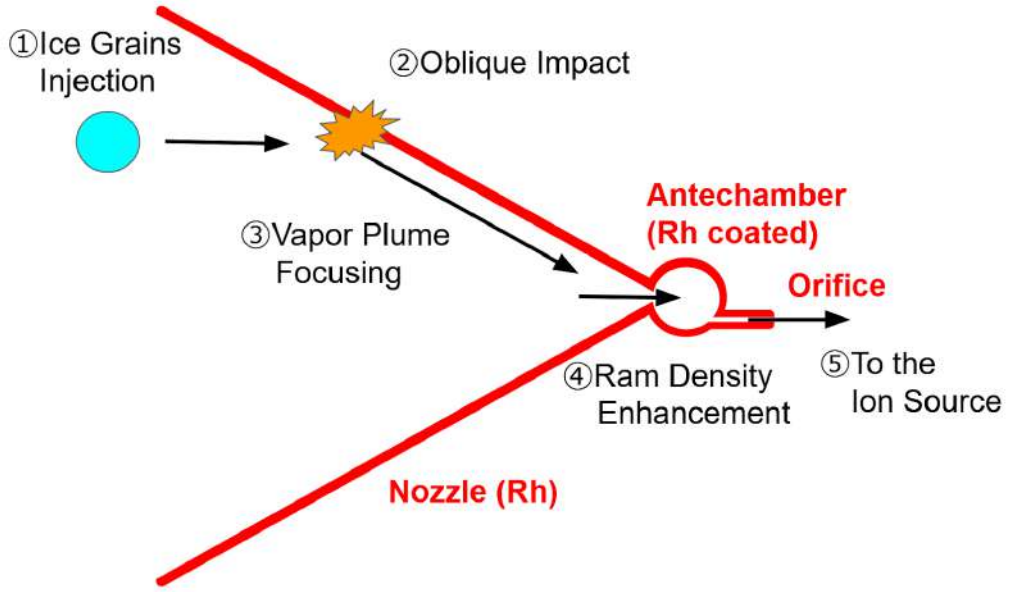

Figure 6-1. Schematic concept of a proposed measurement architecture for an impact-generated gas EI-MS. (1) Icy grains injected from the forward direction enter a wide-aperture rhodium (Rh) nozzle. (2) The grains undergo oblique impacts on the nozzle inner wall, allowing control of the normal component of the impact energy. (3) The generated vapor plume is preferentially directed toward the downstream central axis of the nozzle. (4) The gas is introduced into an Rh-coated antechamber, where ram density enhancement is achieved through temporary gas confinement, and subsequently transported through an orifice to the ion source. This geometry enables efficient gas collection while mitigating excessive molecular fragmentation and intra-instrument chemical reactions.

Future studies should investigate the feasibility and performance of this architecture through numerical modelling, laboratory experiments, and system-level trade-off analyses for spaceborne implementation.

6.2.2 The Advancement of Impact-Generated Gas PI-MS

In the experiments described in Chapter 5, o-xylene at a concentration of 1000 ppm (corresponding to a partial pressure of 5×10^{-6} Pa) was detected at a rate of approximately 1800 ions s^{-1} under a background pressure of 5×10^{-3} Pa, which is considered to be close to the detection limit. As discussed in Section 6.1.2, the abundance of polycyclic aromatic hydrocarbons (PAHs) in the Enceladus plume is assumed on the order of 10–100 ppm by Waite Jr. et al. (2009). Thus, the feasibility of detecting comparable concentrations of o-xylene in impact-induced neutral gas from Enceladus plume particles using PI-MS can be evaluated.

Using the ice grain fluxes measured during the Cassini E7 and E21 flybys at altitudes of 50–100 km and relative velocities of 7–9 km s^{-1}, as reported by Ershova et al. (2024), the total number of ice grain impacts can be estimated. Assuming the nozzle aperture area of 300 cm^2, as proposed in Section 6.2.1, the total number of particle impacts is estimated to be on the order of 3×10^5, corresponding to a total impacting mass of approximately 10^{-8} kg. Under the idealized assumption that all impacting particles undergo impact-induced sublimation and that the generated gas is fully retained, the pressure inside the antechamber is estimated to reach approximately 10^{-4} Pa, assuming an antechamber volume of about 3 cm^3. Furthermore, considering that CDA's"Type 2 particles",potentially containing organic material, account for approximately 25 % of the Enceladus plume particles (Postberg et al., 2018), the expected partial pressure of o-xylene at an abundance level of 10–100 ppm is estimated to be on the order of 10^{-10}–10^{-9} Pa.

In comparison, the detection limit achieved in the experiments of Chapter 5 was a partial pressure of 5×10^{-6} Pa for o-xylene, indicating a sensitivity gap of approximately three to four orders of magnitude relative to the expected plume conditions. However, while the detector gain employed in the Chapter 5 experiments was on the order of 10^4, detector sensitivities of approximately 10^7 are achievable with state-of-the-art spaceborne mass spectrometers (Teolis et al., 2015; Kempf et al., 2025). In addition, taking into account the optimization of the detection geometry discussed in Chapter 5, these improvements are expected to enable photoionization detection with sufficient signal-to-noise ratio even under the same VUV light source output conditions used in the laboratory experiments (Like Figure 5-8 (a) and 5-9 (a)).

In this case, the additional spacecraft resources required for photoionization are estimated, based on catalog specifications, to be approximately 0.5 – 1 kg in mass and 10–30 W in power consumption. It should be noted, however, that the VUV lamp used in the laboratory experiments was not space-qualified, and other consideration factors such as thermal management, deuterium containment, and spacecraft interface requirements may lead to deviations from these estimates. The values presented here should therefore be regarded as indicative rather than definitive.

6.3 Prospects for Future Spaceborne Implementation

Based on the investigations presented in Sections 6.2.1 and 6.2.2, initial requirements regarding power consumption and mass have been established for implementing both impact-generated gas EI-MS and impact-generated gas PI-MS as potential spaceborne instruments in the near future.

For convenience, impact-generated gas EI-MS and impact-generated gas PI-MS are hereafter referred to as I-EI-MS and I-PI-MS, respectively. Both concepts share a fundamental design philosophy with the Cassini INMS instrument. Accordingly, their power and mass requirements are estimated relative to INMS as a baseline. For I-EI-MS, the instrument mass is defined as the mass of

INMS plus the additional mass of the nozzle connected upstream of the antechamber, while the power consumption is assumed to be equivalent to that of INMS. For I-PI-MS, the instrument mass is defined as the mass of INMS plus the mass of the nozzle and a VUV lamp, and the power consumption is estimated as the sum of the INMS power consumption (NASA, 2024) and the VUV lamp power requirement.

A comparison between these estimated power–mass requirements and those of existing spaceborne dust analyzers and neutral gas mass spectrometers is shown in Figure 6-2. The estimated power and mass of I-EI-MS fall entirely within the range occupied by conventional spaceborne mass spectrometers, indicating a very high level of feasibility for spacecraft implementation. In contrast, I-PI-MS is expected to require higher power than conventional instruments, mainly due to the additional power demand of the VUV lamp. This increased power requirement can pose a critical challenge for deep-space missions, where available electrical power is severely limited. Consequently, optimizing the trade-off between VUV lamp power consumption and instrument sensitivity is a key requirement for practical mission implementation.

Nevertheless, the power and mass requirements of I-PI-MS remain well below those of extreme high-end instruments such as MASPEX onboard the Europa Clipper mission. Consequently, I-PI-MS may still represent a viable candidate depending on overall mission design and resource allocation. While the use of VUV lamps in spaceborne applications has limited heritage, necessitating further research and technology demonstration with respect to environmental robustness and long-term operation, the estimated power and mass budgets suggest that I-PI-MS can be a realistic option for future missions from a system-level perspective.

Furthermore, when integrated with state-of-the-art ground-based instruments such as MULTUM (Multiple Turn Mass Spacetrometer) (Toyoda et al., 2003; Aoki and Toyoda, 2021) or Orbitrap (Makarov, 2000; Hu et al., 2005) systems, the developed PI-MS framework could serve as

a powerful platform for detailed organic analysis under controlled laboratory conditions. Such integration would not only provide deeper insights into impact-induced chemistry but also inform the design of future space-qualified soft-ionization mass spectrometers, enabling molecularly faithful detection of complex organic compounds in Solar System exploration missions.

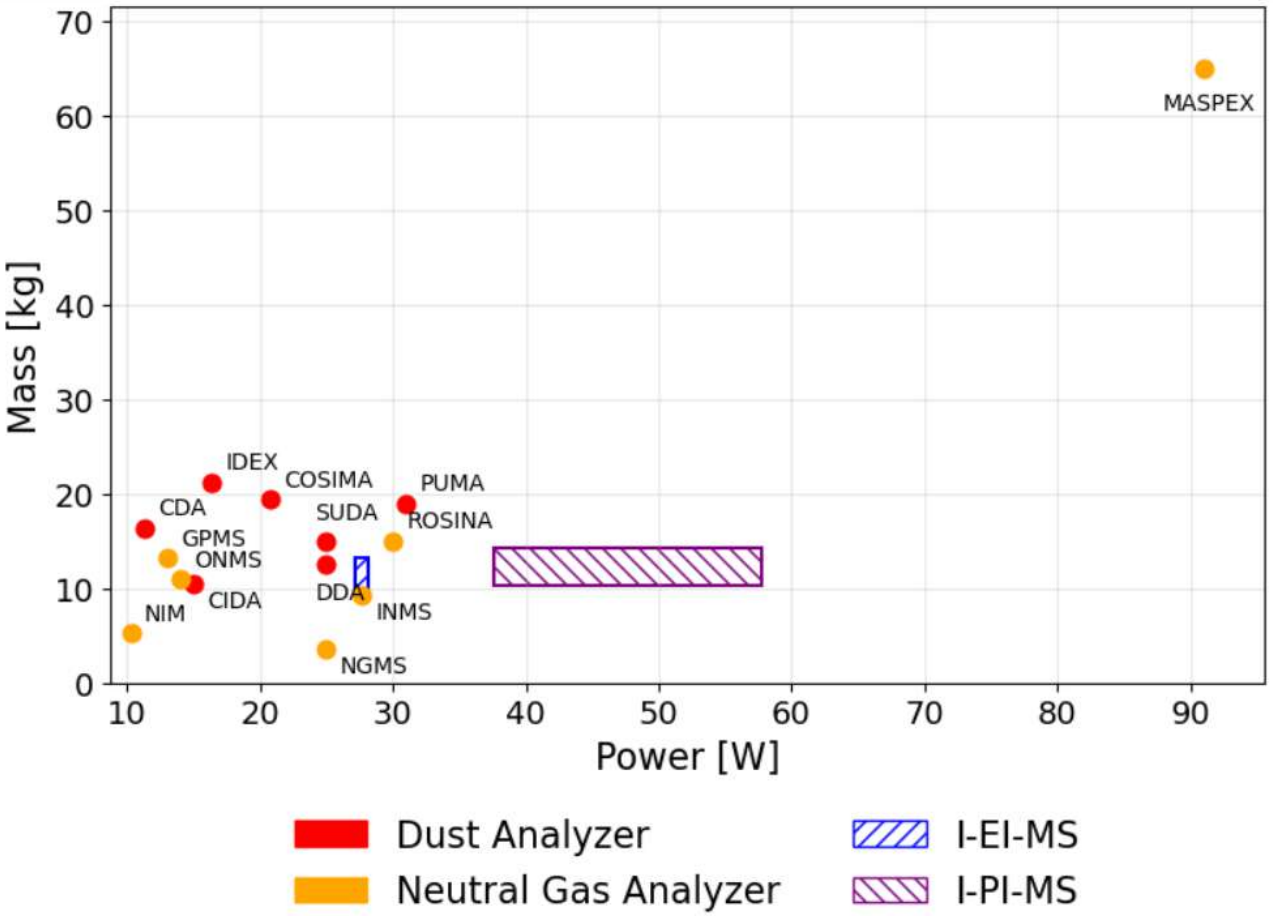

Figure 6-2. Comparison of power consumption and mass among existing spaceborne dust analyzers and neutral gas mass spectrometers, together with estimated design ranges for the proposed impact-generated gas EI-MS (I-EI-MS) and impact-generated gas PI-MS (I-PI-MS). Red symbols indicate dust analyzers and orange symbols indicate neutral gas analyzers, respectively. The shaded blue region represents the initially estimated power–mass range of I-EI-MS, assuming an INMS-based architecture with the addition of a nozzle upstream of the antechamber. The shaded purple region represents the initially estimated range for I-PI-MS, which further includes the mass and power requirements of a VUV lamp.

Acknowledgements

This study was carried out over five years as part of the doctoral program in the Department of Space and Astronautical Science, School of Physical Sciences, SOKENDAI (The Graduate University for Advanced Studies). I would like to take this opportunity to express my heartfelt gratitude to all those who have supported and guided me throughout the course of this research.

This work was supported by JSPS KAKENHI Grant Number JP23KJ1007. I was also privileged to receive support from the JSPS Overseas Challenge Program for Young Researchers, the Tobitate! Study Abroad Initiative, and the SOKENDAI Student Dispatch Program. Numerical computations were performed using the general-purpose PC cluster at the Center for Computational Astrophysics, National Astronomical Observatory of Japan. The joint research project conducted in collaboration with Profs. Hideo Nagatomo and Hirotaka Nakamura was supported by the Institute of Laser Engineering, the University of Osaka.

First and foremost, I would like to express my deepest gratitude to my supervisor Prof. Hajime Yano at the Institute of Space and Astronautical Science (ISAS), Japan Aerospace Exploration Agency (JAXA). His dedicated guidance has not only shaped the direction of my research but also taught me the importance of deep thinking, integrity, and professionalism. I am especially grateful for his generosity in allowing me to participate in fundamental research related to his own inventions, and for the opportunities to explore new themes and collaborations. These experiences have become invaluable foundations for my future career.

I am also sincerely indebted to my deputy supervisor Prof. Takashi Takashima of ISAS/JAXA for his kind and constant support. During the early stages of my experimental work,

when I was still inexperienced, he generously lent me essential instruments, including the vacuum chamber that were indispensable to this study.

I would like to express my sincere gratitude to the members of my doctoral dissertation committee, as well as to the faculty members who participated in Special Research I, Special Research II, and the doctoral thesis examination. Through their careful reviews and insightful comments, they provided invaluable guidance that greatly deepened and refined the content of this research. In particular, I would like to thank Professor Koji Tanaka, Associate Professor Hideo Nagatomo, Professor Mark Burchell, Professor Ralf Srama, Professor Yuko Inatomi, Associate Professor Yoshitsugu Sone, Associate Professor Kosuke Fujishima, Professor Toshihiko Kadono, and Professor Yoshifumi Saito for their expert advice and constructive feedback.

I am also deeply grateful to the students of the M&D Impact Seminar over the past five years. Although I do not list individual names here, I would like to acknowledge that this research was continuously developed through close collaboration and shared discussions with them throughout the entire period.

In addition, I would like to thank the administrative staff of the Department of Space Science at SOKENDAI, especially Mr. Kohira, Ms. Nakayama, and Ms. Fukayama, for their consistent and flexible support. At various stages of my doctoral study, they regularly helped confirm the progress and direction of my research and provided assistance that enabled me to focus fully on my work.

My sincere appreciation also goes to Prof. Shino Suzuki of Riken and Dr. Asuka Shima, Prof. Haruna Sugahara, Prof. Shunta Kimura, Dr. Kazuaki Amikura, Dr. Oya Kawashima, Mr. Takamitsu Iwaya, Mr. Masahiro Yoneda, Dr. Sunao Hasegawa, and Prof. Yoshifumi Saito of ISAS/JAXA. Through stimulating discussions in the laboratory, they provided invaluable suggestions and encouragement. Their warm conversations and daily interactions created an atmosphere of support that greatly enriched my research life. I am also deeply grateful to Ms. Erika

Ito and Ms. Eriko Khan, secretaries of the Inatomi Laboratory at ISAS, for their generous administrative assistance. Despite my frequent and sudden requests, they always responded with patience and kindness.

I wish to express my gratitude to Prof. Hideo Nagatomo, Prof. Hirotaka Nakamura, andProf. Takayoshi Sano of the Institute of Laser Engineering, the University of Osaka for their collaboration in the fundamental experiments and plasma simulations that formed the basis of this study. I also thank the members of the Advanced Manufacturing Technology Group at ISAS/JAXA for their invaluable help in fabricating experimental components. Furthermore, I am grateful to Prof. Mark Burchell, Dr. Penelope Wozniakiewicz, Dr. Jon Tandy, and Dr. Luke Alesbrook at the University of Kent at Canterbury, U.K,, who warmly welcomed me during my stay and provided stimulating discussions on the fundamentals and applications of my experimental and numerical studies. The research results were obtained using the Hypervelocity Impact Facility (former name: Space Plasma Laboratory) of ISAS, JAXA.

I would also like to extend my appreciation to Prof. Koichiro Oyama, Dr. Teruaki Ohno, Dr. Yoshiaki Ando, Dr. Hiromitsu Ryuto, and Mr. Joe Tachibana for their valuable discussions and encouragement as fellow researchers. Their insights and enthusiasm have been a constant source of inspiration.

Finally, I would like to express my deepest love and gratitude to my family: especially to my parents who have supported my education with boundless affection, to my sister and her family who provided comfort during challenging times, and to my partner whose unwavering support has sustained me through both hardships and joy.

Once again, I extend my most sincere appreciation to all those who have contributed to this work through their guidance, collaboration, and kindness. This dissertation would not have been possible without their support.

References

- Ahrens, T. J., & O'Keefe, J. D. (1972). Shock melting and vaporization of lunar rocks and minerals. The Moon, 4(1), 214-249.
- Ahrens, T. J., Gupta, S. C., Jyoti, G., & Beauchamp, J. L. (2003). Mass spectrometer calibration of cosmic dust analyzer. Journal of Geophysical Research: Planets, 108(E2).
- Allamandola, L. J., Sandford, S. A., & Wopenka, B. (1987). Interstellar polycyclic aromatic hydrocarbons and carbon in interplanetary dust particles and meteorites. Science, 237(4810), 56-59.
- Alsharaeh, E. H., & El-Shall, M. S. (2011). Ion mobility study of the mechanism of the gas phase thermal polymerization of styrene and the structures of the early oligomers. Polymer, 52(24), 5551-5559.
- Altwegg K, Balsiger H, Bar-Nun A, Berthelier JJ, Bieler A, Bochsler P, Briois C, Calmonte U, Combi MR, Cottin H, De Keyser J. (2016). Prebiotic chemicals—amino acid and phosphorus—in the coma of comet 67P/Churyumov-Gerasimenko. Science advances, 2(5), e1600285.
- Anderson, J. D., Jacobson, R. A., McElrath, T. P., Moore, W. B., Schubert, G., & Thomas, P. C. (2001). Shape, mean radius, gravity field, and interior structure of Callisto. Icarus, 153(1), 157-161.
- Aoki, J., & Toyoda, M. (2021). Development of novel projection-type imaging mass spectrometer. Review of Scientific Instruments, 92(5).
- Arad, B., Eliezer, S., Gilath, I., Moshe, E., & Simon, C. G. (1996). Laser simulation of hypervelocity impacts in space. WIT Transactions on The Built Environment, 22.
- Arevalo Jr, R., Ni, Z., & Danell, R. M. (2020). Mass spectrometry and planetary exploration: A brief review and future projection. Journal of mass spectrometry, 55(1), e4454.

- Arii, T., Otake, S., Takata, Y., & Matsuura, S. (2006). Evolved gas analysis using photoionization mass spectrometry. Journal of the Mass Spectrometry Society of Japan, 54(6), 243-249.
- Aubert, B., Hebert, D., Rullier, J. L., Lescoute, E., Videau, L., & Berthe, L. (2019). Simulation of laser-driven cratering experiments on aluminum. Journal of Laser Applications, 31(4).
- Bergeron, N. P., Hollerman, W. A., Goedeke, S. M., Hovater, M., Hubbs, W., Finchum, A., ... & Edwards, D. L. (2006). Experimental evidence of triboluminescence induced by hypervelocity impact. International journal of impact engineering, 33(1-12), 91-99.
- Berthias, F., Buridon, V., Abdoul-Carime, H., Farizon, B., Farizon, M., Dinh, P. M., ... & Märk, T. D. (2014). Collision-induced dissociation of protonated water clusters. Physical Review A, 89(6), 062705.
- Born, M., & Wolf, E. (1999). Principles of Optics, 7th (expanded) edition. United Kingdom: Press Syndicate of the University of Cambridge, 461, 401-424.
- Brockwell TG, Meech KJ, Pickens K, Waite JH, Miller G, Roberts J, Lunine JI, Wilson P. (2016). The mass spectrometer for planetary exploration (MASPEX). In 2016 IEEE aerospace conference (pp. 1-17). IEEE.
- Brundage, A. L. (2013). Implementation of Tillotson equation of state for hypervelocity impact of metals, geologic materials, and liquids. Procedia Engineering, 58, 461-470.
- Burchell, M. J., Cole, M. J., & Ratcliff, P. R. (1996). Light flash and ionization from hypervelocity impacts on ice. Icarus, 122(2), 359-365.
- Burchell MJ, Cole MJ, Lascelles SF, Khan MA, Barthet C, Wilson SA, Cairns DB, Armes SP. (1999). Acceleration of conducting polymer-coated latex particles as projectiles in hypervelocity impact experiments. Journal of Physics D: Applied Physics, 32(14), 1719.

- Burchell, M. J., Cole, M. J., McDonnell, J. A. M., & Zarnecki, J. C. (1999). Hypervelocity impact studies using the 2 MV Van de Graaff accelerator and two-stage light gas gun of the University of Kent at Canterbury. Measurement Science and Technology, 10(1), 41.
- Burchell, M. J., Willis, M. J., Armes, S. P., Khan, M. A., Percy, M. J., & Perruchot, C. (2002). Impact ionization experiments with low density conducting polymer-based micro-projectiles as analogues of solar system dusts. Planetary and Space Science, 50(10-11), 1025-1035.
- Burchell, M. J., & Armes, S. P. (2011). Impact ionisation spectra from hypervelocity impacts using aliphatic poly (methyl methacrylate) microparticle projectiles. Rapid Communications in Mass Spectrometry, 25(4), 543-550.
- Burchell, M. J., & Wozniakiewicz, P. J. (2024). Icy ocean worlds, plumes, and tasting the water. Meteoritics & Planetary Science, 59(6), 1385-1406.
- Carlson, R. W., Anderson, M. S., Mehlman, R., & Johnson, R. E. (2005). Distribution of hydrate on Europa: Further evidence for sulfuric acid hydrate. Icarus, 177(2), 461-471.
- Christiansen, E. L., Cykowski, E., & Ortega, J. (1993). Highly oblique impacts into thick and thin targets. International Journal of Impact Engineering, 14(1–4), 157–168.
- Close, S., Linscott, I., Lee, N., Johnson, T., Strauss, D., Goel, A., ... & Bugiel, S. (2013). Detection of electromagnetic pulses produced by hypervelocity micro particle impact plasmas. Physics of Plasmas, 20(9).
- Cowan, H. J. (1956). Representation of the inelastic deformation of concrete by means of a mechanical model. Nature, 178(4527), 278–279.
- Crawford, D. A., & Schultz, P. H. (1999). Electromagnetic properties of impact-generated plasma, vapor and debris. International Journal of Impact Engineering, 23(1), 169-180.
- Cracknell, A. P., & Varotsos, C. A. (2007). Editorial and cover: Fifty years after the first artificial satellite: from sputnik 1 to envisat.

- Crist, B. V. (2018). XPS in industry—Problems with binding energies in journals and binding energy databases. Journal of Electron Spectroscopy and Related Phenomena. (https://doi.org/10.1016/j.elspec.2018.02.005)
- Dahl, D. A. (2000). SIMION 3D Version 7.0 User's manual. Idaho National Engineering and Environmental Laboratory, Idaho Falls, ID, 2-1.
- Dalmann, B. K., Grün, E., Kissel, J., & Dietzel, H. (1977). The ion-composition of the plasma produced by impacts of fast dust particles. Planetary and Space Science, 25(2), 135-147.
- Eichelberger, B. R., Snow, T. P., & Bierbaum, V. M. (2003). Collision rate constants for polarizable ions. Journal of the American Society for Mass Spectrometry, 14(5), 501-505.
- Eichhorn, G. (1976). Analysis of the hypervelocity impact process from impact flash measurements. Planetary and Space Science, 24(8), 771-781.
- Eliezer, S., Ghatak, A. K., Hora, H., & Teller, E. (1986). An introduction to equations of state: Theory and applications. Cambridge University Press.
- Elsila, J. E., Glavin, D. P., & Dworkin, J. P. (2009). Cometary glycine detected in samples returned by Stardust. Meteoritics & planetary science, 44(9), 1323-1330.
- Ershova A, Schmidt J, Postberg F, Khawaja N, Nölle L, Srama R, Kempf S, Southworth B. (2024). Modeling the Enceladus dust plume based on in situ measurements performed with the Cassini Cosmic Dust Analyzer. Astronomy & Astrophysics, 689, A114.
- Faravelli, T., Bozzano, G., Scassa, C., Perego, M., Fabini, S., Ranzi, E. L. I. S. E. O., & Dente, M. (1999). Gas product distribution from polyethylene pyrolysis. Journal of Analytical and Applied Pyrolysis, 52(1), 87-103.
- Faravelli, T., Pinciroli, M., Pisano, F., Bozzano, G., Dente, M., & Ranzi, E. L. I. S. E. O. (2001). Thermal degradation of polystyrene. Journal of analytical and applied pyrolysis, 60(1), 103-121.

- Faravelli, T., Bozzano, G., Colombo, M., Ranzi, E., & Dente, M. (2003). Kinetic modeling of the thermal degradation of polyethylene and polystyrene mixtures. Journal of Analytical and Applied Pyrolysis, 70(2), 761-777.
- Farley KA, Williford KH, Stack KM, Bhartia R, Chen A, de la Torre M, Hand K, Goreva Y, Herd CD, Hueso R, Liu Y. (2020). Mars 2020 mission overview. Space Science Reviews, 216(8), 1-41.
- Feldmann, D., Kutzner, J., Laukemper, J., MacRobert, S., & Welge, K. H. (1987). Mass spectroscopic studies of the ArF-laser photoablation of polystyrene. Applied Physics B, 44(2), 81-85.
- Fletcher, A., Close, S., & Mathias, D. (2015). Simulating plasma production from hypervelocity impacts. Physics of Plasmas, 22(9).
- Fransson, T., Harada, Y., Kosugi, N., Besley, N. A., Winter, B., Rehr, J. J., ... & Nilsson, A. (2016). X-ray and electron spectroscopy of water. Chemical reviews, 116(13), 7551-7569.
- Friichtenicht, J. F., & Slattery, J. C. (1963). Ionization associated with hypervelocity impact (No. NASA-TN-D-2091).
- Fukumura, H., Mibuka, N., Eura, S., & Masuhara, H. (1993). Mass spectrometric studies on laser ablation of polystyrene sensitized with anthracene. The Journal of Physical Chemistry, 97(51), 13761-13766.
- Furukawa Y, Chikaraishi Y, Ohkouchi N, Ogawa NO, Glavin DP, Dworkin JP, Abe C, Nakamura T. (2019). Extraterrestrial ribose and other sugars in primitive meteorites. Proceedings of the National Academy of Sciences, 116(49), 24440-24445.
- Fuse, R., Abe, S., Yanagisawa, M., & Hasegawa, S. (2020). An experimental study of the impact flash: the relationship between luminous efficiency and vacuum level. Planetary and Space Science, 187, 104921.

- Gao, P., & Stevenson, D. J. (2013). Nonhydrostatic effects and the determination of icy satellites' moment of inertia. Icarus, 226(2), 1185-1191.
- Glassmeier, K. H., Boehnhardt, H., Koschny, D., Kührt, E., & Richter, I. (2007). The Rosetta mission: flying towards the origin of the solar system. Space Science Reviews, 128(1), 1-21.
- Glavin, D. P., Elsila, J. E., Burton, A. S., Callahan, M. P., Dworkin, J. P., Hilts, R. W., & Herd, C. D. (2012). Unusual nonterrestrial l-proteinogenic amino acid excesses in the Tagish Lake meteorite. Meteoritics & Planetary Science, 47(8), 1347-1364.
- Glavin, D. P., Burton, A. S., Elsila, J. E., Aponte, J. C., & Dworkin, J. P. (2019). The search for chiral asymmetry as a potential biosignature in our solar system. Chemical reviews, 120(11), 4660-4689.
- Goel, A., Tarantino, P. M., Lauben, D. S., & Close, S. (2015). Design and testing of miniaturized plasma sensor for measuring hypervelocity impact plasmas. Review of Scientific Instruments, 86(4).
- Goel, A. (2016). Detection and characterization of meteoroid and orbital debris impacts in space. Stanford University.
- Goldsworthy, B. J., Burchell, M. J., Cole, M. J., Green, S. F., Leese, M. R., McBride, N., ... & Khan, M. A. (2002). Laboratory calibration of the cassini cosmic dust analyser (CDA) using new, low density projectiles. Advances in Space Research, 29(8), 1139-1144.
- Goldsworthy, B. J., Burchell, M. J., Cole, M. J., Armes, S. P., Khan, M. A., Lascelles, S. F., ... & Bigger, S. W. (2003). Time of flight mass spectra of ions in plasmas produced by hypervelocity impacts of organic and mineralogical microparticles on a cosmic dust analyser. Astronomy & Astrophysics, 409(3), 1151-1167.
- Göller, J. R., & Grün, E. (1989). Calibration of the Galileo/Ulysses dust detectors with different projectile materials and at varying impact angles. Planetary and Space Science, 37(10), 1197-1206.

- Grasset O, Dougherty MK, Coustenis A, Bunce EJ, Erd C, Titov D, Blanc M, Coates A, Drossart P, Fletcher LN, Hussmann H. (2013). JUpiter ICy moons Explorer (JUICE): An ESA mission to orbit Ganymede and to characterise the Jupiter system. Planetary and Space Science, 78, 1-21.
- Griesmann, U., & Burnett, J. H. (1999). Refractivity of nitrogen gas in the vacuum ultraviolet. Optics letters, 24(23), 1699-1701.
- Grün, E., Fechtig, H., Kissel, J., Linkert, D., Maas, D., McDonnell, J. A. M., ... & Giese, R. H. (1992). The Ulysses dust experiment. Astronomy and Astrophysics Supplement Series (ISSN 0365-0138), vol. 92, no. 2, Jan. 1992, p. 411-423., 92, 411-423.
- Haefliger, O. P., & Zenobi, R. (1998). New sample preparation for quantitative laser desorption mass spectrometry and optical spectroscopy. Review of scientific instruments, 69(4), 1828-1832.
- Hamann C, Luther R, Ebert M, Hecht L, Deutsch A, Wünnemann K, Schäffer S, Osterholz J, Lexow B. (2016). Correlating laser-generated melts with impact-generated melts: An integrated thermodynamic-petrologic approach. Geophysical Research Letters, 43(20), 10-602.
- Harlow, F. H., & Pracht, W. E. (1966). Formation and penetration of high-speed collapse jets. The Physics of Fluids, 9(10), 1951-1959.
- Hayhurst, C. J., Ranson, H. J., Gardner, D. J., & Birnbaum, N. K. (1995). Modelling of microparticle hypervelocity oblique impacts on thick targets. International Journal of Impact Engineering, 17(1–3), 375–386.
- Hew, Y. M., & Close, S. (2021). Hypervelocity impact flash expansion geometry under various spacecraft surface electrical conditions. International Journal of Impact Engineering, 150, 103792.

- Hsu HW, Postberg F, Sekine Y, Shibuya T, Kempf S, Horányi M, Juhász A, Altobelli N, Suzuki K, Masaki Y, Kuwatani T. (2015). Ongoing hydrothermal activities within Enceladus. Nature, 519(7542), 207-210.
- Hsu HW, Schmidt J, Kempf S, Postberg F, Moragas-Klostermeyer G, Seiß M, Hoffmann H, Burton M, Ye S, Kurth WS, Horányi M. (2018). In situ collection of dust grains falling from Saturn's rings into its atmosphere. Science, 362(6410), eaat3185.
- Hu, Q., Noll, R. J., Li, H., Makarov, A., Hardman, M., & Graham Cooks, R. (2005). The Orbitrap: a new mass spectrometer. Journal of mass spectrometry, 40(4), 430-443.
- Huang, S. S. (1960). Life-supporting regions in the vicinity of binary systems. Publications of the Astronomical Society of the Pacific, 72(425), 106-114.
- Hughes, D. W. (1987). The history of Halley's Comet. Philosophical Transactions of the Royal Society of London. Series A, Mathematical and Physical Sciences, 323(1572), 349-367.
- Iess, L., Stevenson, D. J., Parisi, M., Hemingway, D., Jacobson, R. A., Lunine, J. I., ... & Tortora, P. (2014). The gravity field and interior structure of Enceladus. Science, 344(6179), 78-80.
- Jean, B., & Rollins, T. L. (1970). Radiation from hypervelocity impact generated plasma. AIAA Journal, 8(10), 1742-1748.
- Kadono, T., Sugita, S., Mitani, N. K., Fuyuki, M., Ohno, S., Sekine, Y., & Matsui, T. (2002). Vapor clouds generated by laser ablation and hypervelocity impact. Geophysical research letters, 29(20), 40-1.
- Kasting, J. F., Whitmire, D. P., & Reynolds, R. T. (1993). Habitable zones around main sequence stars. Icarus, 101(1), 108-128.
- Katayama, M., Abe, A., & Takeba, A. (2017). Investigation on Mie-Grüneisen type shock Hugoniot equation of state for concrete. International Journal of Multiphysics, 11(3).

- Kempf, S. (2018, September). The Surface Dust Analyzer (SUDA) on Europa Clipper. In European Planetary Science Congress (pp. EPSC2018-462).
- Kempf S, Tucker S, Altobelli N, Briois C, Cable ML, Grün E, Gudipati MS, Henderson BL, Hsu HW, Hand K, Horanyi M. (2025). SUDA: A SUrface Dust Analyser for compositional mapping of the Galilean moon Europa. Space Science Reviews, 221(1), 10.
- Khawaja N, Postberg F, Hillier J, Klenner F, Kempf S, Nölle L, Reviol R, Zou Z, Srama R. (2019). Low-mass nitrogen-, oxygen-bearing, and aromatic compounds in Enceladean ice grains. Monthly Notices of the Royal Astronomical Society, 489(4), 5231-5243.
- Khawaja, N., Hillier, J., Klenner, F., Nölle, L., & Postberg, F. (2020). Comparative Study of Mass Spectrometry Techniques Relevant to Current and Future Space Missions (No. EPSC2020-827). Copernicus Meetings.
- Khawaja N, Postberg F, O'Sullivan TR, Napoleoni M, Kempf S, Klenner F, Sekine Y, Craddock M, Hillier J, Simolka J, Hortal Sánchez L. (2025). Detection of organic compounds in freshly ejected ice grains from Enceladus's ocean. Nature Astronomy, 1-10.
- Kirk, R. L., Soderblom, L. A., Brown, R. H., Kieffer, S. W., & Kargel, J. S. (1995). Triton's plumes: discovery, characteristics, and models. Neptune and Triton, 949-989.
- Kissela, J., Krueger, F. R., Silenc, J., & Haerendela, G. (2001). The Probable Chemical Nature of Interstellar Dust Particles Detected by" CIDA" Onboard" STARDUST. The Outer Heliosphere: The Next Frontiers, 11.
- Kissel, J. (1986). The Giotto particulate impact analyzer. The Giotto Mission: Its Scientific Investigations, 67-83.
- Kissel, J., & Krueger, F. R. (1987). Ion formation by impact of fast dust particles and comparison with related techniques. Applied physics A, 42(1), 69-85.
- Kissel, J., & Krueger, F. R. (2001). Time-of-flight mass spectrometric analysis of ion formation in hypervelocity impact of organic polymer microspheres: comparison with

secondary ion mass spectrometry, 252Cf mass spectrometry and laser mass spectrometry. Rapid Communications in Mass Spectrometry, 15(18), 1713-1718.

- Kissel, J., Krueger, F. R., Silén, J., & Clark, B. C. (2004). The cometary and interstellar dust analyzer at comet 81P/Wild 2. Science, 304(5678), 1774-1776.
- Klenner F, Postberg F, Hillier J, Khawaja N, Reviol R, Srama R, Abel B, Stolz F, Kempf S. (2019). Analogue spectra for impact ionization mass spectra of water ice grains obtained at different impact speeds in space. Rapid Communications in Mass Spectrometry, 33(22), 1751-1760.
- Klenner F, Umair M, Walter SH, Khawaja N, Hillier J, Nölle L, Zou Z, Napoleoni M, Sanderink A, Zuschneid W, Abel B. (2022). Developing a laser induced liquid beam ion desorption spectral database as reference for spaceborne mass spectrometers. Earth and Space Science, 9(9), e2022EA002313.
- Knabe, W., & Krueger, F. R. (1982). Ion formation from alkali iodide solids by swift dust particle impact. Zeitschrift für Naturforschung A, 37(12), 1335-1340.
- Krueger, F. R., & Kissel, J. (1984). Experimental investigations on ion emission with dust impact on solidsurfaces. ESA Special Publication, 224, 43-48.
- Krueger, F. R. (1984). Ion emission from solid surfaces: comparison of dust impact with other excitations. ESA Special Publication, 224, 49-54.
- Krueger, F. R., & Kissel, J. (1987). The chemical composition of the dust of comet P/Halley as measured by “PUMA” on board VEGA-1. Naturwissenschaften, 74(7), 312-316.
- Krueger, F. R., & Kissel, J. (2006). Interstellar and cometary dust in relation to the origin of life. In Comets and the Origin and Evolution of Life (pp. 325-339). Berlin, Heidelberg: Springer Berlin Heidelberg.

- Lebreton JP, Witasse O, Sollazzo C, Blancquaert T, Couzin P, Schipper AM, Jones JB, Matson DL, Gurvits LI, Atkinson DH, Kazeminejad B. (2005). An overview of the descent and landing of the Huygens probe on Titan. Nature, 438(7069), 758-764.
- Lee N, Close S, Lauben D, Linscott I, Goel A, Johnson T, Yee J, Fletcher A, Srama R, Bugiel S, Mocker A. (2012). Measurements of freely-expanding plasma from hypervelocity impacts. International Journal of Impact Engineering, 44, 40-49.
- Li, J., Song, W., Ning, J., & Tang, H. (2014). Characteristics of impact-generated plasma with different electron temperature and gas temperature. Modern Physics Letters B, 28(18), 1450152.
- Lin MF, Singh N, Liang S, Mo M, Nunes JP, Ledbetter K, Yang J, Kozina M, Weathersby S, Shen X, Cordones AA. (2021). Imaging the short-lived hydroxyl-hydronium pair in ionized liquid water. Science, 374(6563), 92-95.
- Mackay, N. G., Green, S. F., Gardner, D. J., & McDonnell, J. A. M. (1995, February 1). Experimental investigation of the relationship between impact crater morphology and impacting particle velocity and direction. In LDEF: 69 months in space. Third post-retrieval symposium (Part 1). NASA Langley Research Center.
- MacKenzie, S. M., Neveu, M., Davila, A. F., Lunine, J. I., Craft, K. L., Cable, M. L., ... & Spilker, L. J. (2021). The Enceladus Orbilander mission concept: Balancing return and resources in the search for life. The Planetary Science Journal, 2(2), 77.
- Maimone, M. W., Leger, P. C., & Biesiadecki, J. J. (2007, April). Overview of the mars exploration rovers' autonomous mobility and vision capabilities. In IEEE international conference on robotics and automation (ICRA) space robotics workshop.
- Makarov, A. (2000). Electrostatic axially harmonic orbital trapping: a high-performance technique of mass analysis. Analytical chemistry, 72(6), 1156-1162.

- Matson, D. L., Spilker, L. J., & Lebreton, J. P. (2003). The Cassini/Huygens mission to the Saturnian system. The Cassini-Huygens Mission, 1-58.
- McDonnell, J. A. M. (1993). Hydrocode modelling in the study of space debris impact crater morphology. In Proceedings of the First European Conference on Space Debris (pp. 425–431). Darmstadt, Germany.
- McEwen AS, Keszthelyi L, Geissler P, Simonelli DP, Carr MH, Johnson TV, Klaasen KP, Breneman HH, Jones TJ, Kaufman JM, Magee KP. (1998). Active volcanism on Io as seen by Galileo SSI. Icarus, 135(1), 181-219.
- Melosh, H. J. (1989). Impact cratering: A geologic process. Oxford University Press.
- Melosh, H. J. (2007). A hydrocode equation of state for SiO2. Meteoritics & planetary science, 42(12), 2079-2098.
- Mihalas, D., & Mihalas, B. W. (2013). Foundations of radiation hydrodynamics. Courier Corporation.
- Mihaly, J. M., Rosakis, A. J., Adams, M. A., & Tandy, J. T. (2013). Imaging ejecta and debris cloud behavior using laser side-lighting. Procedia Engineering, 58, 363-368.
- Mikula R, Sternovsky Z, Armes SP, Ayari E, Bouwman J, Chan DH, Fontanese J, Horanyi M, Hillier JK, Kempf S, Khawaja N. (2024). Impact ionization mass spectra of polypyrrole-coated anthracene microparticles: a useful mimic for cosmic polycyclic aromatic hydrocarbon dust. ACS Earth and Space Chemistry, 8(3), 586-605.
- Mocker, A., Grün, E., Sternovsky, Z., Drake, K., Kempf, S., Hornung, K., & Srama, R. (2012). On the applicability of laser ionization for simulating hypervelocity impacts. Journal of Applied Physics, 112(10).
- Mocker A, Hornung K, Grün E, Kempf S, Collette A, Drake K, Horányi M, Munsat T, O'Brien L, Sternovsky Z, Srama R. (2013). On the application of a linear time-of-flight mass

spectrometer for the investigation of hypervelocity impacts of micron and sub-micron sized dust particles. Planetary and Space Science, 89, 47-57.

- More, R. M., Warren, K. H., Young, D. A., & Zimmerman, G. B. (1988). A new quotidian equation of state (QEOS) for hot dense matter. The Physics of fluids, 31(10), 3059-3078.
- Nagatomo, H., Johzaki, T., Sunahara, A., & Mima, K. (2006). The formation of high-density core plasma in non-spherical implosion using high-resolution two-dimensional integrated implosion code. Journal of plasma physics, 72(6), 791-794.
- Nagatomo H, Johzaki T, Asahina T, Sunahara A, Sano T, Sakagami H, Mima K, Fujioka S, Shiraga H, Azechi H. (2015). Computational study of magnetic field compression by laser-driven implosion. Nuclear Fusion, 55(9), 093028.
- Naraoka H, Takano Y, Dworkin JP, Oba Y, Hamase K, Furusho A, Ogawa NO, Hashiguchi M, Fukushima K, Aoki D, Schmitt-Kopplin P. (2023). Soluble organic molecules in samples of the carbonaceous asteroid (162173) Ryugu. Science, 379(6634), eabn9033.
- National Aeronautics and Space Administration. (2017). Enceladus hydrothermal activity [Illustration]. (https://science.nasa.gov/resource/enceladus-hydrothermal-activity/)
- National Aeronautics and Space Administration. (2024, November 2). INMS engineering technical write-up. NASA Science. (https://science.nasa.gov/mission/cassini/spacecraft/cassini-orbiter/ion-and-neutral-mass-spectrometer/inms-technical-write-up/)
- National Academies of Sciences, Engineering, and Medicine. (2022). Origins, Worlds, and Life: A Decadal Strategy for Planetary Science and Astrobiology 2023-2032.
- Neau A, Al Khalili A, Rosén S, Le Padellec A, Derkatch AM, Shi W, Vikor L, Larsson M, Semaniak J, Thomas R, Någård MB. (2000). Dissociative recombination of D 3 O+ and H 3 O+: absolute cross sections and branching ratios. The Journal of Chemical Physics, 113(5), 1762-1770.

- Neveu, M., Hays, L. E., Voytek, M. A., New, M. H., & Schulte, M. D. (2018). The ladder of life detection. Astrobiology, 18(11), 1375-1402.
- Neveu M, Anbar AD, Davila AF, Glavin DP, MacKenzie SM, Phillips-Lander CM, Sherwood B, Takano Y, Williams P, Yano H. (2020). Returning samples from Enceladus for life detection. Frontiers in Astronomy and Space Sciences, 7, 26.
- Nimmo F, Hamilton DP, McKinnon WB, Schenk PM, Binzel RP, Bierson CJ, Beyer RA, Moore JM, Stern SA, Weaver HA, Olkin CB. (2016). Reorientation of Sputnik Planitia implies a subsurface ocean on Pluto. Nature, 540(7631), 94-96.
- Nimmo, F., & Pappalardo, R. T. (2016). Ocean worlds in the outer solar system. Journal of Geophysical Research: Planets, 121(8), 1378-1399.
- Nisar, J., Ali, G., Shah, A., Shah, M. R., Iqbal, M., Ashiq, M. N., & Bhatti, H. N. (2019). Pyrolysis of expanded waste polystyrene: influence of nickel-doped copper oxide on kinetics, thermodynamics, and product distribution. Energy & Fuels, 33(12), 12666-12678.
- Ohno, S., Sugita, S., Kadono, T., Hasegawa, S., & Igarashi, G. (2004). Sulfur chemistry in laser-simulated impact vapor clouds: implications for the K/T impact event. Earth and Planetary Science Letters, 218(3-4), 347-361.
- Öjekull, J. (2007). Dissociative Recombination of Ammonia and Water Cluster Ions with Free Electrons.
- Öjekull, J., Andersson, P. U., Pettersson, J. B., Marković, N., Thomas, R. D., Al Khalili, A., Källberg, A. (2008). Dissociative recombination of water cluster ions with free electrons: Cross sections and branching ratios. The Journal of chemical physics, 128(4).
- Okada, Y., Yamaguchi, S., Kawai, Y., Orii, T., & Takeuchi, K. (2003). Incorporation probability of a water molecule into a water cluster. Chemical physics, 294(1), 37-43.
- Overbye, D. (2013). Far-Off Planets Like the Earth Dot the Galaxy. New York Times.

- Peck, E. R., & Khanna, B. N. (1966). Dispersion of nitrogen. Journal of the Optical Society of America, 56(8), 1059-1063.
- Person, J. C., & Nicole, P. P. (1970). Isotope effects in the photoionization yields and the absorption cross sections for acetylene, propyne, and propene. The Journal of Chemical Physics, 53(5), 1767-1774.
- Peterson, G., Nimmo, F., & Schenk, P. (2015). Elastic thickness and heat flux estimates for the uranian satellite Ariel. Icarus, 250, 116-122.
- Phillips, C. B., & Pappalardo, R. T. (2014). Europa Clipper mission concept: Exploring Jupiter's ocean moon. Eos, Transactions American Geophysical Union, 95(20), 165-167.
- Pierazzo, E., & Melosh, H. J. (2000). Understanding oblique impacts from experiments, observations, and modeling. Annual Review of Earth and Planetary Sciences, 28(1), 141-167.
- Pirri, A. N. (1977). Theory for laser simulation of hypervelocity impact. The Physics of Fluids, 20(2), 221-228.
- Pizzarello, S., Cooper, G. W., & Flynn, G. J. (2006). The nature and distribution of the organic material in carbonaceous chondrites and interplanetary dust particles. Meteorites and the early solar system II, 1, 625-651.
- Porco CC, Helfenstein P, Thomas PC, Ingersoll AP, Wisdom J, West R, Neukum G, Denk T, Wagner R, Roatsch T, Kieffer S. (2006). Cassini observes the active south pole of Enceladus. science, 311(5766), 1393-1401.
- Postberg F, Hillier JK, Armes SP, Bugiel S, Butterworth A, Dupin D, Fielding LA, Fujii S, Gainsforth Z, Grün E, Li YW. (2014). Stardust Interstellar Preliminary Examination IX: High-speed interstellar dust analog capture in Stardust flight-spare aerogel. Meteoritics & Planetary Science, 49(9), 1666-1679.

- Postberg F, Kempf S, Rost D, Stephan T, Srama R, Trieloff M, Mocker A, Goerlich M. (2009). Discriminating contamination from particle components in spectra of Cassini's dust detector CDA. Planetary and Space Science, 57(12), 1359-1374.
- Postberg F, Khawaja N, Abel B, Choblet G, Glein CR, Gudipati MS, Henderson BL, Hsu HW, Kempf S, Klenner F, Moragas-Klostermeyer G. (2018). Macromolecular organic compounds from the depths of Enceladus. Nature, 558(7711), 564-568.
- Postberg F, Sekine Y, Klenner F, Glein CR, Zou Z, Abel B, Furuya K, Hillier JK, Khawaja N, Kempf S, Noelle L. (2023). Detection of phosphates originating from Enceladus's ocean. Nature, 618(7965), 489-493.
- Ratcliff, P. R., Burchell, M. J., Cole, M. J., Murphy, T. W., & Alladfadi, F. (1997). Experimental measurements of hypervelocity impact plasma yield and energetics. International journal of impact engineering, 20(6-10), 663-674.
- Ratcliff, P. R., Reber, M., Cole, M. J., Murphy, T. W., & Tsembelis, K. (1997). Velocity thresholds for impact plasma production. Advances in Space Research, 20(8), 1471-1476.
- Roy SK, Trabia M, O'Toole B, Hixson R, Becker S, Pena M, Jennings R, Somasoundaram D, Matthes M, Daykin E, Machorro E. (2016). Study of hypervelocity projectile impact on thick metal plates. Shock and Vibration, 2016(1), 4313480.
- Salama, I. E., Slavchov, R. I., Filip, S. V., & Clarke, S. M. (2025). Chemisorption and physisorption of alcohols on iron (III) oxide-terminated surfaces from nonpolar solvents. Journal of Colloid and Interface Science, 685, 15-28.
- Sanderink A, Klenner F, Zymak I, Žabka J, Postberg F, Lebreton JP, Gaubicher B, Charvat A, Abel B, Polášek M, Cherville B. (2023). OLYMPIA-LILBID: a new laboratory setup to calibrate spaceborne hypervelocity ice grain detectors using high-resolution mass spectrometry. Analytical Chemistry, 95(7), 3621-3628.

- Sandford SA, Aléon J, Alexander CM, Araki T, Bajt S, Baratta GA, Borg J, Bradley JP, Brownlee DE, Brucato JR, Burchell MJ. (2006). Organics captured from comet 81P/Wild 2 by the Stardust spacecraft. Science, 314(5806), 1720-1724.
- Schultz, P. H. (1996). Effect of impact angle on vaporization. Journal of Geophysical Research: Planets, 101(E9), 21117-21136.
- Schultz, P. H., & Eberhardy, C. A. (2015). Spectral probing of impact-generated vapor in laboratory experiments. Icarus, 248, 448-462.
- Sekine Y, Shibuya T, Postberg F, Hsu HW, Suzuki K, Masaki Y, Kuwatani T, Mori M, Hong PK, Yoshizaki M, Tachibana S. (2015). High-temperature water–rock interactions and hydrothermal environments in the chondrite-like core of Enceladus. Nature Communications, 6(1), 8604.
- Sephton, M. A. (2002). Organic compounds in carbonaceous meteorites. Natural product reports, 19(3), 292-311.
- Shibaguchi, T., Onuki, H., & Onaka, R. (1977). Electronic structures of water and ice. Journal of the Physical Society of Japan, 42(1), 152-158.
- Sikes, T., Banyon, C., Schwind, R. A., Lynch, P. T., Comandini, A., Sivaramakrishnan, R., & Tranter, R. S. (2021). Initiation reactions in the high temperature decomposition of styrene. Physical Chemistry Chemical Physics, 23(34), 18432-18448.
- Simpson, G., Moreno, J., Shaeffer, M., & Ramesh, K. T. (2023). First contact: Fine structure of the impact flash and ejecta during hypervelocity impact. PNAS nexus, 2(7), pgad214.
- Som, S. M. (2019, December). The" Life Detection Forum" Project. In AGU Fall Meeting Abstracts (Vol. 2019, pp. P21E-3422).
- Song, W., Lv, Y., Li, J., Wang, C., & Ning, J. (2016). Influence of impact conditions on plasma generation during hypervelocity impact by aluminum projectile. Physics of Plasmas, 23(7).

- Sparks, W. B., Hand, K. P., McGrath, M. A., Bergeron, E., Cracraft, M., & Deustua, S. E. (2016). Probing for evidence of plumes on Europa with HST/STIS. The Astrophysical Journal, 829(2), 121.
- Spencer, M. K., Hammond, M. R., & Zare, R. N. (2008). Laser mass spectrometric detection of extraterrestrial aromatic molecules: Mini-review and examination of pulsed heating effects. Proceedings of the National Academy of Sciences, 105(47), 18096-18101.
- Spitzer, L., & Harm, R. (1953). Heat conductivity of an electron gas. Phys. Rev., 89, 977.
- Spohn, T., & Schubert, G. (2003). Oceans in the icy Galilean satellites of Jupiter?. Icarus, 161(2), 456-467.
- Srama, R., Ahrens, T. J., Altobelli, N., Auer, S., Bradley, J. G., Burton, M., ... & Zook, H. A. (2004). The Cassini cosmic dust analyzer. Space Science Reviews, 114(1), 465-518.
- Srama R, Woiwode W, Postberg F, Armes SP, Fujii S, Dupin D, Ormond-Prout J, Sternovsky Z, Kempf S, Moragas-Klostermeyer G, Mocker A. (2009). Mass spectrometry of hyper-velocity impacts of organic micrograins. Rapid Communications in Mass Spectrometry: An International Journal Devoted to the Rapid Dissemination of Up-to-the-Minute Research in Mass Spectrometry, 23(24), 3895-3906.
- Srinivasan, J. M., Barltrop, C., Berman, S., Bushman, S., Dickson, J., Drain, T., ... & Tuszynski, M. (2025). Europa Clipper flight system overview. Space Science Reviews, 221(1), 1-30.
- Slater, J. C. (1930). Atomic shielding constants. Physical review, 36(1), 57.
- Stübig, M. (2002). New insights in impact ionization and in time-of-flight mass spectroscopy with micrometeoroid detectors by improved impact simulations in the laboratory (Doctoral dissertation).

- Sugita, S., Schultz, P. H., & Adams, M. A. (1998). Spectroscopic measurements of vapor clouds due to oblique impacts. Journal of Geophysical Research: Planets, 103(E8), 19427-19441.
- Sugita, S., & Schultz, P. H. (1999). Spectroscopic characterization of hypervelocity jetting: Comparison with a standard theory. Journal of Geophysical Research: Planets, 104(E12), 30825-30845.
- Sugita, S., & Schultz, P. H. (2002). Initiation of run-out flows on Venus by oblique impacts. Icarus, 155(2), 265-284.
- Sugita, S., & Schultz, P. H. (2003). Interactions between impact-induced vapor clouds and the ambient atmosphere: 2. Theoretical modeling. Journal of Geophysical Research: Planets, 108(E6).
- Sugita, S., Schultz, P. H., & Hasegawa, S. (2003). Intensities of atomic lines and molecular bands observed in impact-induced luminescence. Journal of Geophysical Research: Planets, 108(E12).
- Takabe, H. (1993). Hydrodynamic Simluation Code for Laser Driven Implosion. Laser and Part. Beams.
- Takabe, H., & Nishikawa, T. (1994). Computational model for non-LTE atomic process in laser produced plasmas. Journal of Quantitative Spectroscopy and Radiative Transfer, 51(1-2), 379-395.
- Takami, K., & Takabe, H. (1990). Simple fitting formulas of equation of state for laser produced plasmas (Tech. Rep. No. 40). Osaka University.
- Tandy, J. D., Mihaly, J. M., Adams, M. A., & Rosakis, A. J. (2014). Examining the temporal evolution of hypervelocity impact phenomena via high-speed imaging and ultraviolet-visible emission spectroscopy. Journal of Applied Physics, 116(3).

- Tandy, J. D., Price, M. C., Wozniakiewicz, P. J., Cole, M. J., Alesbrook, L. S., & Avdellidou, C. (2020). Impact flash evolution of CO2 ice, water ice, and frozen Martian and lunar regolith simulant targets. Meteoritics & Planetary Science, 55(10), 2301-2319.
- Tarantino, P., Goel, A., Corso, A., Lee, N., & Close, S. (2018). An electrostatic method to model the expansion of hypervelocity impact plasma on positively biased surfaces. Physics of Plasmas, 25(9).
- Teolis, B. D., Perry, M. E., Magee, B. A., Westlake, J., & Waite, J. H. (2010). Detection and measurement of ice grains and gas distribution in the Enceladus plume by Cassini's Ion Neutral Mass Spectrometer. Journal of Geophysical Research: Space Physics, 115(A9).
- Teolis BD, Niemann HB, Waite JH, Gell DA, Perryman RS, Kasprzak WT, Mandt KE, Yelle RV, Lee AY, Pelletier FJ, Miller GP. (2015). A revised sensitivity model for Cassini INMS: Results at Titan. Space Science Reviews, 190(1), 47-84.
- Tillotson, J. H. (1962). Metallic equations of state for hypervelocity impact (No. GA3216).
- Timmermann, R., & Grün, E. (1991, January). Plasma emission from high velocity impacts of microparticles onto water ice. In International Astronomical Union Colloquium (Vol. 126, pp. 375-378). Cambridge University Press.
- Tong, D. (2012). Kinetic theory: University of Cambridge graduate course.
- Toyoda, M., Okumura, D., Ishihara, M., & Katakuse, I. (2003). Multi-turn time-of-flight mass spectrometers with electrostatic sectors. Journal of mass spectrometry, 38(11), 1125-1142.
- Tsunakawa, H., Takahashi, F., Shimizu, H., Shibuya, H., & Matsushima, M. (2015). Surface vector mapping of magnetic anomalies over the Moon using Kaguya and Lunar Prospector observations. Journal of Geophysical Research: Planets, 120(6), 1160-1185.

- Waite Jr, J. H., Lewis, W. S., Kasprzak, W. T., Anicich, V. G., Block, B. P., Cravens, T. E., ... & Yelle, R. V. (2004). The Cassini ion and neutral mass spectrometer (INMS) investigation. Space Science Reviews, 114(1), 113-231.
- Waite Jr JH, Combi MR, Ip WH, Cravens TE, McNutt Jr RL, Kasprzak W, Yelle R, Luhmann J, Niemann H, Gell D, Magee B. (2006). Cassini ion and neutral mass spectrometer: Enceladus plume composition and structure. science, 311(5766), 1419-1422.
- Waite JH, Glein CR, Perryman RS, Teolis BD, Magee BA, Miller G, Grimes J, Perry ME, Miller KE, Bouquet A, Lunine JI. (2017). Cassini finds molecular hydrogen in the Enceladus plume: evidence for hydrothermal processes. Science, 356(6334), 155-159.
- Waite Jr JH, Perryman RS, Perry ME, Miller KE, Bell J, Cravens TE, Glein CR, Grimes J, Hedman M, Cuzzi J, Brockwell T. (2018). Chemical interactions between Saturn's atmosphere and its rings. Science, 362(6410), eaat2382.
- Waite, J. H., Brockwell, T., Glein, C., & Perry, R. (2019, September). MASPEX-Europa aboard Clipper: A mass spectrometer for investigating the habitability of Europa. In Epsc-dps joint meeting.
- Waite Jr, J. H., Burch, J. L., Brockwell, T. G., Young, D. T., Miller, G. P., Persyn, S. C., ... & Siegmund, O. H. W. (2024). MASPEX-Europa: the Europa Clipper neutral gas mass spectrometer investigation. Space Science Reviews, 220(3), 30.
- Walsh, J. M., Shreffler, R. G., & Willig, F. J. (1953). Limiting conditions for jet formation in high velocity collisions. Journal of Applied Physics, 24(3), 349-359.
- Wen, K., & Chen, X. W. (2020). Analysis of the stress wave and rarefaction wave produced by hypervelocity impact of sphere onto thin plate. Defence Technology, 16(5), 969-979.
- Wolf, A. A., & Smith, J. C. (1995). Design of the Cassini tour trajectory in the Saturnian system. Control Engineering Practice, 3(11), 1611-1619.

- Yabuta H, Cody GD, Engrand C, Kebukawa Y, De Gregorio B, Bonal L, Remusat L, Stroud R, Quirico E, Nittler L, Hashiguchi M. (2023). Macromolecular organic matter in samples of the asteroid (162173) Ryugu. Science, 379(6634), eabn9057.
- Yada T, Abe M, Okada T, Nakato A, Yogata K, Miyazaki A, Hatakeda K, Kumagai K, Nishimura M, Hitomi Y, Soejima H. (2022). Preliminary analysis of the Hayabusa2 samples returned from C-type asteroid Ryugu. Nature Astronomy, 6(2), 214-220.
- Yafei H, Enling T, Liping H, Meng W, Kai G, Jin X, Jianjun M, Shuhua L, Ruizhi W, Zhenbo L. (2019). Evolutionary characteristics of thermal radiation induced by 2A12 aluminum plate under hypervelocity impact loading. International Journal of Impact Engineering, 125, 173-179.
- Yafei, H., Maoen, Y., Enling, T., Chuang, C., Mengzhou, C., Kai, G., & Liping, H. (2021). Experimental study on flash radiation and damage characteristics of C/SiC composites induced by hypervelocity impact. International Journal of Impact Engineering, 155, 103902.
- Yamaguchi, S., Kudoh, S., Okada, Y., Orii, T., & Takeuchi, K. (2002). Cluster size dependence of the H/D exchange reaction rate constant for protonated water clusters H+ (H2O) n (n= 2–11). Chemical Physics Letters, 359(5-6), 480-485.
- Yamaguchi, S., Kudoh, S., Kawai, Y., Okada, Y., Orii, T., & Takeuchi, K. (2003). Collisional reaction of water cluster cations (H2O) n+ (n= 2 and 3) with D2O. Chemical Physics Letters, 377(1-2), 37-42.
- Yano H, Kubota T, Miyamoto H, Okada T, Scheeres D, Takagi Y, Yoshida K, Abe M, Abe S, Barnouin-Jha O, Fujiwara A. (2006). Touchdown of the Hayabusa spacecraft at the Muses Sea on Itokawa. Science, 312(5778), 1350-1353.
- Yurimoto H, Abe KI, Abe M, Ebihara M, Fujimura A, Hashiguchi M, Hashizume K, Ireland TR, Itoh S, Katayama J, Kato C. (2011). Oxygen isotopic compositions of asteroidal materials returned from Itokawa by the Hayabusa mission. Science, 333(6046), 1116-1119.

- Zamith, S., Kassem, A., L'hermite, J. M., Joblin, C., & Cuny, J. (2023). Threshold collision induced dissociation of protonated water clusters. The Journal of Chemical Physics, 159(18).
- Zhang, K., Long, R., Zhang, Q., Xue, Y., & Ju, Y. (2016). Flash characteristics of plasma induced by hypervelocity impact. Physics of Plasmas, 23(8).
- Zhao, L., Wang, H., Fu, S., Zhao, C., & Wu, Y. (2025). A theoretical model for estimating hypervelocity impact generated plasma (HVIGP) considering phase transitions. International Journal of Impact Engineering, 203, 105341.
- Zhaoxia, M. A., Anhua, S. H. I., Junling, L. I., Hai, L. I. U., Pei, L. I. U., & Sen, L. I. U. (2020). Radiation mechanism analysis of hypervelocity impact Ejecta cloud. International Journal of Impact Engineering, 141, 103560.
- Zhou, Z., Xie, M., Wang, Z., & Qi, F. (2009). Determination of absolute photoionization cross-sections of aromatics and aromatic derivatives. Rapid Communications in Mass Spectrometry: An International Journal Devoted to the Rapid Dissemination of Up-to-the-Minute Research in Mass Spectrometry, 23(24), 3994-4002.